Rational Structure Design of Transition Metal Chalcogenide Multifunctional Sulfur Immobilizer for Fast and Durable Li-S Performance

by

Dan Luo

A thesis

presented to the University of Waterloo

in fulfillment of the

thesis requirement for the degree of

Doctor of Philosophy

in

Chemical Engineering

Waterloo, Ontario, Canada, 2020

Examining Committee Membership

The following served on the Examining Committee for this thesis. The decision of the Examining Committee is by majority vote.

External Examiner	Dr. Juchen Guo Associate Professor
Supervisor	Dr. Zhongwei Chen Professor
Internal Member	Dr. Eric Croiset Professor
Internal Member	Dr. Ali Elkamel Professor
Internal-external Member	Dr. Zhongchao Tan Professor

Author's Declaration

This thesis consists of materials that I authored or co-authored: see Statement of Contributions in the thesis. This is a true copy of the thesis, including any required final revisions, as accepted by my examiners.

I understand that my thesis may be made electronically available to the public.

Statement of Contributions

Some of the chapters in this thesis are based published works co-authored by myself. These include the following publications.

Chapter 3 of this thesis consists of some paragraphs from two research papers that I was co-authored with my supervisor, Ya-Ping Deng, Dr. Gaoran Li, Dr. Jing Fu, Dr. Xiaolei Wang, Ruilin Liang, Dr. Wen Lei, Dr. Yuanli Ding, Dr. Aiping Yu, Dr. Juan Wu, Dr. Liangshuai Liu. I am the first author of these papers. In these works, I performed most of the experiments, data analyses, and manuscript preparation.

"Tuning shell numbers of transition metal oxide hollow microspheres toward durable and superior lithium storage", ACS Nano, 2017, 11, 11521-11530.

Chapter 4 of this thesis consists of some paragraphs from two research papers that I was co-authored with my supervisor, Dr. Gaoran Li, Ya-Ping Deng, Zhen Zhang, Ruilin Liang, Dr. Jingde Li, Matthew Li, Dr. Yi Jiang, Dr. Aiping Yu, Weiwei Zhang, Dr. Liangshuai Liu, Dr. Wen Lei. I am the first author of these papers. In these works, I performed most of the experiments, data analyses, and manuscript preparation.

"Synergistic engineering of defects and architecture in binary metal chalcogenide toward fast and reliable lithium-sulfur batteries", Advanced Energy Materials, 2019, 1900228.

Chapter 5 of this thesis consists of some paragraphs from the research paper that I was co-authored with my supervisor, Dr. Guihua Liu, Dr. Rui Gao, Dr. Aiping Yu. I am the co-

first author of these papers. In these works, I performed most of the experiments, data analysis and involved in the writing of the manuscript.

"An combined ordered macro-mesoporous architecture design and surface engineering strategy for high-performance sulfur immobilizer in lithium-sulfur batteries", Small, 2020, 2001089.

Chapter 6 of this thesis consist of paragraphs from two research papers that I was co-authored with my supervisor, Zhen Zhang, Dr. Gaoran Li, Dr. Sahobo Cheng, Dr. Shuang Li, Dr. Jingde Li, Dr. Rui Gao, Matthew Li, Ya-Ping Deng, Dr. Yi Jiang, Serubbabel Sy, Dr. Yongfeng Hu, Haozhen Dou, Yanfei Zhu, Dr. Aiping Yu. In these works, I performed most of the experiments, data analysis and involved in the writing of the manuscript.

"Revealing the rapid electrocatalytic behavior of ultrafine amorphous defective Nb_2O_{5-x} nanocluster towards superior Li-S performance", ACS Nano, 2020, 14, 4849-4860.

"Ship in a bottle design of highly efficient bifunctional electrocatalysts for long-lasting rechargeable Zn-air batteries", ACS Nano 2019, 13, 7062-7072.

Abstract

Lithium-sulfur (Li-S) batteries are one of the most promising candidates for next-generation energy storage owing to their high energy density, environmental benignity and cost effectiveness. However, the practical application of Li-S batteries is still hindered by technical challenges, including the insulating nature of sulfur, the sluggish redox reaction kinetics and notorious polysulfide shuttle effect. Rational design of sulfur electrode is significant to improving Li-S performance, among which the morphology control, defect engineering and ultrafine structure implantation in the design of multifunctional sulfur immobilizer holds a great potential in altering the physical and electrochemical features toward fast and durable sulfur electrochemistry.

This thesis work is mainly focused on the advanced structure design of cobalt-based transition metal chalcogenides (TMCs) multifunctional sulfur immobilizer for enhanced sulfur confinement, expedited redox reaction and accelerated lithium polysulfides (LiPS) conversion kinetics. Chapter 3 introduces a universal and straightforward synthesis method developed to produce multishelled Co_3O_4 hollow microspheres with tunable composition and shell numbers. The sulfur confinement was investigated when employed this material as sulfur host. The evolution of multishelled structure was further revealed and the underlying formation mechanism was also elucidated. The as-synthesized Co_3O_4 quadruple-shelled hollow microsphere offers a large active surface area and a large void interior, which stockpiles sulfur and reserves electrolyte inside the shell, leading to alleviated volume expansion and blocked migration of LiPS. Thus, a higher discharge capacity and prolonged cycle life were perceived.

Defect engineering strategy was further identified to accelerate the electron conduction, LiPS adsorption and catalytic conversion on cobalt based transitional metal oxides for enhanced Li-S performance. Chapter 4 introduces the double shelled Co_3O_4 porous hollow microsphere with vast oxygen defects. The incorporated oxygen vacancies on the octahedral sites of spinel Co_3O_4 not only serves as active sites to immobilize sulfur species, but also strengthen the electron conduction for accelerated redox reaction. Owing to these structural advantages, this sulfur composite delivers a higher discharge capacity, an improved rate capability, and an enhanced cyclability, even under raised sulfur loading. Instead of oxygen defect, the positive effects brought by defect engineering can be further extended to other type of anion defects. Chapter 5 introduces the three-dimensional ordered mesoporous Co_9S_8 material with admirable sulfur defects was developed. The triply hierarchical design offers potent sulfur immobilization while the defect engineering also induces the formation of sulfur vacancies on the octahedral sites of Co_9S_8, which serve as active sites to strengthen LiPS adsorption and accelerate its conversion reaction. Therefore, a superb rate capability and an excellent cyclic stability can be realized under a high sulfur loading and a low electrolyte/sulfur (E/S) ratio in Li-S battery.

These findings indicate that the elaborate structure manipulation of TMCs is capable of altering its physical/chemical properties, thus improving the electrochemical performance in all aspects. Chapter 6 is dedicated to a unique porous carbon composite structure inlaid with ultrafine nanoparticles that was delicately created. Comparing with cobalt based TMCs, implanting niobium based TMCs inside porous carbon exhibits good nanoparticle dispersity with controllable content, offering more active surface area for redox reaction. The synchronous engineering encompassing nanoreactor design, defect implantation and

crystallinity engineering endow this composite material with superior LiPS adsorption and catalytic conversion. The as-developed ultrafine, amorphous and oxygen-deficient Nb_2O_5 nanocluster microporous carbon implantation, which serves as nanoreactor, demonstrates higher sulfur utilization, potent sulfur immobilization, and fast catalytic conversion of LiPS. Attributed to these structural superiorities, this material delivers a remarkable discharge capacity, a superior rate capability and an ultra-long cycle lifespan, even under high sulfur loading and lean E/S ratio. These material engineering strategies hold great promises to promote the development of sulfur cathode design toward high performance Li-S batteries.

Acknowledgements

I would like to express my sincere gratitude to my supervisor, Professor Zhongwei Chen, for his support, motivation, guidance and advice during my Ph.D studies. I would also like extend thanks to my Ph.D. exam committee members, including Professors Eric Croiset, Professor Zhongchao Tan and Professor Ali Elkamel from the University of Waterloo, and Professor Juchen Guo as the external examiner from the University of California, Riverside for their valuable time and insights.

I would also like to thank all the group members who were always there to help in my project. I also received help from my outstanding colleagues who include, but are not limited to, Dr. Gaoran Li, Zhen Zhang, Ya-Ping Deng, Dr. Gaopeng Jiang, Dr. Rui Gao, Dr. Kaiyuan Shi, Dr. Jingde Li, Dr. Guihua Liu, Ruilin Liang, Dr. Matthew Li, Dr. Wen Lei, Dr. Yanfei Zhu and Dr. Yi Jiang. I would also like to thank Dr. Dong Su and Dr. Liwei Chen for their invaluable advices for my research works. Thanks a lot for all your help and support in the past four years. Moreover, I would like to acknowledge my parents, family members and friends. I am grateful for their unconditional love, support and sacrifice.

Finally, I would like to mention my gratitude to the Natural Science and Engineering Research Council of Canada (NSERC), the Waterloo Institute for Nanotechnology, and the University of Waterloo for their financial support.

Table of contents

List of Figures

List of Tables

List of Abbreviations

3DOM	Three-dimensional ordered mesoporous
BE	Binding Energy
BET	Brunauer-Emmett-Teller
CE	Coulombic efficiency
CMF	Carbonaceous microspherical framework
CV	Cyclic voltammetry
DFT	Density functional theory
DME	Dimethoxymethane
DOL	1,3-dioxolane
DFT	Density functional theory
DSC	Differential scanning calorimetry
EDX	Energy dispersive X-ray spectroscopy
EELS	Electron energy loss spectroscopy
EIS	Electrochemical impedance spectroscopy
ELNES	Electron loss near edge spectroscopy
EPR	Electron paramagnetic spectroscopy
E/S ratio	Electrolyte/sulfur ratio
EV	Electric vehicles
EXAFS	Extended X-ray absorption fine structure
FFT	Fast Fourier transform
FTIR	Fourier transform Infrared spectroscopy
GCD	Galvanostatic charge-discharge

HRTEM	High-resolution TEM
HS	Hollow sphere
KB	Ketjen Black
LCF	Linear combination fitting
LIBs	Lithium-ion batteries
LiPS	Lithium polysulfides
Li-S	Lithium-sulfur
LiTFSI	Bis(trifluoromethanesulfonyl)imide lithium salt
MAPs	Metal acetate polysaccharides
MCS	Microporous carbon sphere
NCO-HS	Nickel cobalt oxide hollow sphere
NPs	Nanoparticles
OCV	Open-circuit voltage
PAW	Projected augmented wave
PBE	Perdew-Burke-Ernzerhof
PS	Polysulfides
PSD	Pore size distribution
PVDF	Polyvinylidene fluoride
R_{ct}	Charge transfer resistance
QS-HS	Quadruple shelled hollow sphere
SAD	Selected area diffraction
SEI	Solid electrolyte interface
SEM	Scanning electron microscopy

SSE	Solid state electrolyte
STEM	Scanning transmission electron microscopy
TEGDME	Tetraethylene glycol dimethyl ether
TEM	Transmission electron microscopy
THF	Tetrahydrofuran
TGA	Thermal gravimetric analysis
TMO	Transition metal oxide
TMC	Transition metal chalcogenide
UV-vis	Ultraviolet-visible spectroscopy
VASP	Vienna Ab initio Simulation Package
XANES	X-ray absorption near-edge structure
XPS	X-ray photoelectron spectroscopy
XRD	X-ray diffraction

Chapter 1 Introduction

1.1 Overview of LIBs

The rechargeable batteries stem from the reversible nature of the redox reactions that occur at each electrode of the cell. Amongst all the rechargeable battery systems that have serviced mankind for decades, lithium-ion batteries (LIBs) have dominated the commercial battery market, especially for the electric vehicle (EV) market, owing to their high cell voltage, low self-discharge rate, and stable cycling performance. In the history of LIBs, Whittinghan et al. reported the first rechargeable LIBs prototype with Titanium Sulfide as cathode while Li metal as anode in 1976. In 1981, Goodenough et al. first developed the use of lithium cobalt oxide ($LiCoO_2$) as a high-energy and high-voltage cathode material. In 1983, Goodenough also identified manganese spinel as low-cost cathode material. In 1987, Yohsino et al. field the patent and developed prototype LIBs using $LiCoO_2$ as cathode and carbon as anode, realizing the large-scale production of LIBs in 1990s. As a reward, John B. Goodenough, Stanley Whittingham and Akira Yoshino jointly won the Nobel Chemistry prize 2019, recognizing their pioneering work in LIBs (Figure 1.1).

The cell of LIBs usually consists of cathodes and anodes, which are separated by the Li-ion containing electrolyte and separators. A commercially available LIBs consists of lithium metal oxide such as $LiCoO_2$ or $LiFePO_4$ as cathode while carbon-based material, like graphite, as anode (Figure 1.1). Both electrodes operate under the principles of lithium intercalation. During discharge, Li^+ moves from high chemical potential anode to low chemical potentials cathode. Meanwhile, electrons transfer from the anode to the cathode, which converts chemical energy into electric work. Additionally, an electrically insulating separator was placed between the cathode and anode to avoid short-circuiting happen

inside cell. The separator wetted by electrolyte exhibits low viscosity and high Li^+ mobility at room temperature. Typical electrolyte comprises propylene carbonate (PC), ethylene carbonate (EC), diethyl carbonate (DEC) and dimethyl carbonate (DMC) as solvent and lithium hexafluorophosphate ($LiPF_6$) or Bis(trifluoromethane)sulfonimide lithium salt (LiTFSI) as dissolved salts. The electrolyte has mediate mobility of Li^+ to ensure the fast Li^+ transportation without experiencing huge overpotential of the battery. It also demonstrates wide electrochemical voltage window for normal operation without severe electrolyte decomposition.

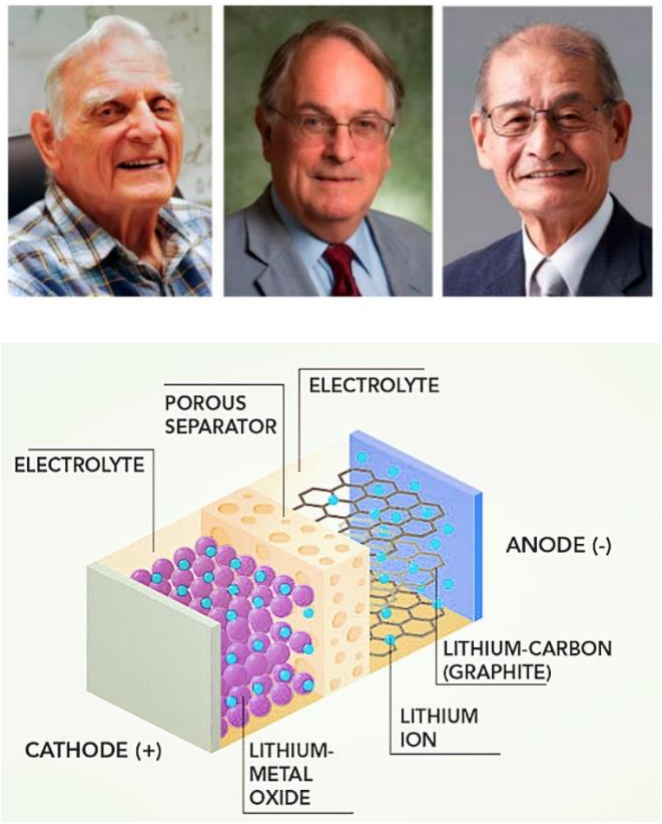

Figure 1.1 Top: 2019 Nobel Prize in chemistry was jointly awarded to John B. Goodenough, M. Stanley Whittingham, and Akira Yoshino (left to right)[1]; Bottom:

Schematic illustration of commercial LIBs with graphite as anode and lithium metal oxide as cathode.

The most important parameter that enabling the application of LIBs is its high energy density comparing with other type of rechargeable batteries including lead-acid battery and nickel-metal hydride battery. The total Gibbs free energy change caused by the electrochemical reaction on the two electrodes influences the energy density of LIBs. Given the entire electrochemical reaction and the transferred charge, the theoretical battery voltage can be determined from $\Delta E = -\Delta G/nF$. Gravimetric energy measures the energy that can be stored and released per unit mass battery. It can be acquired by multiplying the gravimetric capacity (mAh g^{-1}) by the working battery voltage (V). Gravimetric capacity measures the amount of charge reversibly stored per unit mass. It is closely related to the number of electrons released by the electrochemical reaction and the atomic weight of the host. The theoretical capacity of the active electrode material can be estimated based on the electrochemical reactions involved. For example, for an electrochemical reaction with a graphite anode that can be reversibly intercalated with Li to form LiC_6, the reaction is:

$$Li^+ + e^- + C_6 \rightleftharpoons LiC_6$$

For the cathodic reaction by using $LiCoO_2$ as anode, which usually discharge 50% of its capacity, the reaction can be written as follow:

$$LiCoO_2 \rightleftharpoons 0.5Li^+ + 0.5e^- + Li_{0.5}CoO_2$$

The practically viable LIBs employing this configuration deliver a high energy density of ~150 Wh kg^{-1}. Current state-of-art LIBs employed with high capacity cathode and anode

material show a high energy density up to 300 Wh kg^{-1} on the cell level. Unfortunately, minimal change in energy density can further be made if the same material cathode and anode are used. This limitation stems from the inherent ability of the metal oxide and graphite to uptake and accommodate Li^+ in its layered structure. The lithiation of $LiCoO_2$ cathode material theoretically has a specific capacity of 274 mAh g^{-1} and an actual capacity of~170 mAh g^{-1} to ensure a high electrochemical reversibility.[2] Although new cathode material, like $LiNi_{0.8}Co_{0.1}Mn_{0.1}O_2$, with much higher theoretical and practical has been developed, the severe structure deformation also exists in this material over the course of electrochemical process, leading to fast capacity fading and poor cycle life. Therefore, the realization of high energy density energy storage is one of the greatest scientific and engineering challenges in the twenty-first century.[3-5] New battery prototype is desperately demanded for future use to increase both the energy density and cycle life.

1.2 Introduction of Li-S battery

Sulfur is a promising candidate of cathode material, which located in the chalcogen group of the periodic table, possesses a redox potential of 2.15 V vs Li^+/Li.[6] Although this voltage is lower than commercial metal oxide cathode materials because of its relatively low oxidizing power comparing with oxygen, the capacity for lithium and sulfur is significantly superior to commercial metal oxides.[7] The high theoretical capacity (1672 mAh g^{-1}) of sulfur and high theoretical energy density on both volume (2.8 kWh L^{-1}) and weight (2.5 kWh kg^{-1}) basis of lithium-sulfur (Li-S) configuration attracts much attention from battery research community.[8, 9] The Li-S energy is generated through the electrochemical redox reaction between S and lithium sulfide (Li_2S) accompanied by a series of intermediate lithium polysulfides (LiPS) in ether-based electrolyte such as 1,3 dioxolane (DOL) and

dimethoxyethane (DME).[10] The operation of a Li-S battery relies on the conversion reaction of S, which involves two reduction steps. In the first reduction process, solid sulfur dissolved into the electrolyte, which generates high-order LiPS (Li_2S_x, $4 \le x \le 8$).[11] As the element sulfur is cumulatively reduced, the soluble long chain LiPS turns into short chain LiPS and transform to insoluble Li_2S_2/Li_2S. Actually, the reduction mechanism of sulfur is much more complex in nature compared to that of metal oxides and remains elusive and debated among the research community. The following equations illustrate a proposed reduction pathway:

$$S_8 + 2e^- = S_8^{2-}$$

$$3S_8^{2-} + 2e^- = 4S_6^{2-}$$

$$2S_6^{2-} + 2e^- = 3S_4^{2-}$$

$$S_4^{2-} + 6e^- = 4S^{2-}$$

Overall, the discharge reaction of sulfur is listed as follows:[11]

$$S_8 + 16Li^+ + 16e^- = 8Li_2S$$

During oxidation process, the insoluble Li_2S_2 and Li_2S are gradually oxidized to LiPS and finally become sulfur. A detailed illustration of sulfur chemistry for solid-liquid sulfur conversion and corresponding galvanostatic charge-discharge (GCD) profiles is shown in Figure 1.2.

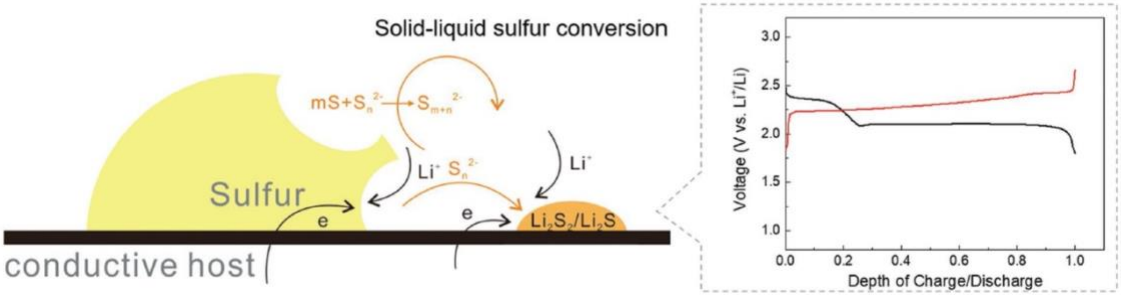

Figure 1.2 Illustration of the sulfur electrochemistry and the corresponding voltage profiles based on solid-liquid sulfur conversion.[12]

1.3 Challenges of Li-S battery

Current Li-S technology is still not able to meet the requirements of commercial applications owing to its low practical energy density and limited cycle lifespan. The main problems are mainly come from the cathode side, which are associated with four aspects: (1) poor ion and electron transport dynamics due to the uncontrolled dissolution of complex sulfur species and the insulating nature of S (σ = 5 × 10^{-30} S cm^{-1}) [13] and Li_2S (σ = 10^{-13} S cm^{-1});[14] (2) the huge volume variation of the active materials result in fragile electrode integrity during cycling; (3) dissolution of active materials into electrolytes stemming from the shuttling of soluble LiPS intermediates; (4) the sluggish redox reaction kinetics of S/Li_2S leads to low sulfur utilization and huge potential hysteresis, especially in fast charge-discharge process. Among them, the notorious LiPS shuttle effect is a significant obstacle that hampers the development of Li-S batteries. In discharge process, the solved polysulfide (PS), which shuttle back and forth between electrodes, considerable increases the electrolyte viscosity and reduces the ionic conductivity, leading to capacity decay and low coulombic efficiency during cycling. The concentration gradient determines that sulfur species cannot be fully reformed on the cathode, rendering irreversible sulfur loss and capacity fading. Moreover, the chemical disproportionation of PS produces insulate Li_2S_2/Li_2S precipitates in both the cathode and separator, leading to porosity loss and less electrolyte infiltration. The high solubility of LiPS intermediates in commonly used electrolytes can also diffuse from cathode to anode and reduce on the lithium surface,

generating insoluble Li_2S_2/Li_2S deposition, rendering impeded charge transfer kinetics and capacity loss. These behaviors result in severely hindered Li-S performance and making the practical Li-S battery unachievable in the foreseeable future.

However, this behavior is a double-edged sword because certain amount of soluble LiPS in electrolyte could favors the thermodynamically sluggish reactions of Li_2S and S.[15] The participation of Li_2S on the lithium surface also favors the stable solid electrolyte interface (SEI) formation, which physically block the contact between lithium and electrolyte and further suppress their spontaneously side reactions.[16] An inhibited Li dendrite formation can be realized when employing $LiNO_3$ in electrolyte, which reduces the short-circuiting safety concerns.[17, 18] During discharge process, the PS dissolution drags the insulating sulfur into electrolyte via chemical comproportionation, leading to improved sulfur utilization. The reduction of generated PS on the host surface uniformly redistributes sulfur on the electrode surface during charge process. Therefore, the delicate manipulation on PS behavior to amplify its positive effects has great significance in Li-S battery performance.

Another bottleneck of Li-S battery is its sluggish LiPS conversion kinetics. The fast reduction of sulfur to higher-order and highly soluble LiPS and sluggish transformation from LiPS to lower order and insoluble LiPS results in a high LiPS concentration in liquid electrolytes, leading to stagnant ion transportation. Besides, the slow redox reaction induces non-uniform Li_2S_2/Li_2S deposition and agglomeration under fast discharge rate, part of which cannot be fully oxidized to sulfur, leading to low sulfur utilization and low Coulombic efficiency (CE). Enhancing conversion kinetics of soluble LiPS to alleviate the shuttle effect has attracted more attentions.[19] On the other hand, promoting the conversion of dissolved LiPS to solid Li_2S not only reduces the bulk concentration of active species,

which shortens the retention time of LiPS in electrolytes, but also facilitates the complete reaction of sulfur.[20] Therefore, realizing rapid redox kinetics of LiPS plays a pivotal role for achieving expedite Li-S performance.

To overcome those problems, various approaches for the confinement of these sulfur species and LiPS shuttle inhabitation and accelerated Li-S kinetics were developed which mainly focus on three ways: (1) sulfur host construction, (2) lithium metal protection (3) electrolyte modification and (4) interlayer and separator design.

1.4 Sulfur cathode design

Sulfur cathode host have been intensively studied in order to overcome the problem caused by soluble LiPS.[21] To enhance the electronic conductivity of sulfur cathode, a host material has been introduced to facilitate electron transportation and homogenize sulfur distribution. The host material also exhibits satisfactory physical and/or chemical sulfur confinement to immobilize PS species within cathodes for inhibited shuttle effect. Normally, the sulfur host can be divided into three categories: carbon host, polar host and composite host. Each of them has its own merits to meet the performance requirement in different scenarios.

1.4.1 Physical sulfur confinement of porous carbon host

Carbon based material is a promising candidate as sulfur host due to its excellent conductivity, high porosity and light weight. Much effort has been devoted to immobilize sulfur using carbonaceous materials in the past decade. Multiple carbon materials with various morphologies and structures have been widely investigated, serving as conductive agents as well as physical absorber to PS (Figure 1.3). It is reported the mesoporous carbon is a promising candidate as sulfur host, which can offer strong sulfur immobilization owing to the spatial confinement of aligned mesopores.[22] Apart from that, the employed of

mesoporous carbon also results a uniform distribution of nano-sized sulfur. Size refinement effect of uniformly distributed active sulfur favors sulfur chemistry and significantly reduces the stress/strain during the lithiation/delithiation process. These carbonaceous materials provide additional electron conduction and pathways for electrolyte and Li^+ ion diffusion and offers physical confinement to stockpile sulfur.

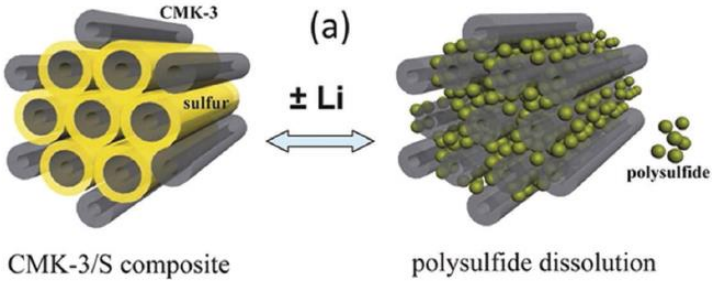

Figure 1.3 Scheme of carbon/sulfur composite for improving the cathode performance.[23]

1.4.2 Strong chemical affinity of polar host

Although carbonaceous material exhibits high electronic conductivity and homogenized sulfur distribution, its LiPS confinement is still low due to the poor chemical interaction between non-polar carbon and polar LiPS. Thus, polar materials with strong chemical affinity have been developed as promising multifunctional hosts for admirable sulfur electrochemistry. Polar hosts such as metal oxides,[24] metal sulfides,[25, 26] and polymers[27-29] have been widely studied to constrain active cathode materials by the high binding energy (BE) between sulfur species and materials. The favorable physi- and chemi-interactions strengthen LiPS adsorption within the cathode,[30, 31] while nanostructured polar material can further promote the reaction kinetics by offering decent electronic and ionic conductivity. On the other hand, too strong chemical bondage between nonconductive materials and

Li_2S_x could indeed impair the proper function of Li-S batteries because trapping Li_2S_x too tight on insulating substrates would hinder the electron transfer and deactivate S materials. Therefore, intermediate binding between nonconductive materials and the S species is favorable.[32] It is also suggested that conducting substrate could facilitate the electron transfer along the cathode host and favor the sluggish redox reactions of the insulating sulfur species. Many literatures have reported that non-conductive metal oxides on a carbon substrate have remarkable ability of trapping LiPS and promote the electrochemical properties.[33] The oxidative properties of metal oxide not only physically trap LiPS on its surface, but also oxidize PS to thiosulfate or sulfate, which in turn facilitates the Li-S chemistry.[34] Wang et al.[35] demonstrated an innovative strategy to efficiently entrap LiPS through the synergistic effect of structural restriction and chemical encapsulation using metal oxide-decorated hollow spheres. This nanocomposites with a unique hollow structure favor highly stable sulfur electrochemistry benefited from its admirable physical and chemical sulfur immobilization (Figure 1.4).

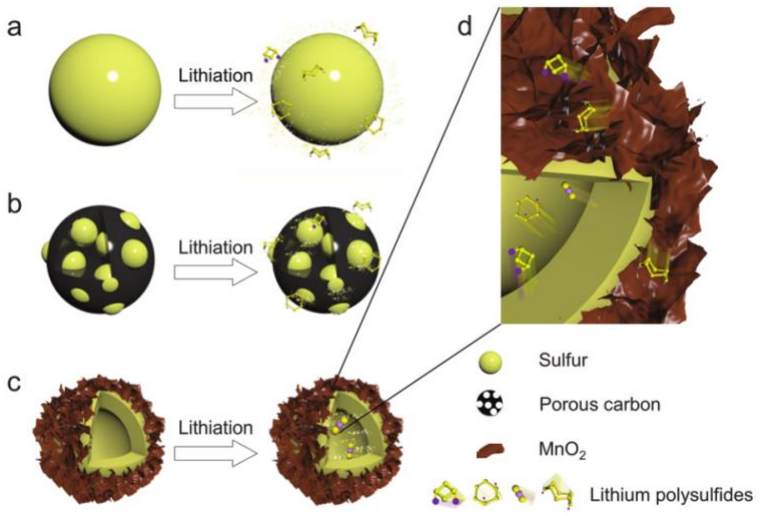

Figure 1.4 Schematic of the lithiation process in various S-based materials. (a) Bare S particles suffer from severe PS dissolution. (b) Porous carbon materials provide structural restriction of S and limited LiPS dissolution and diffusion suppression. (c) The MnO_2-decorated hollow S spheres provide both structural and chemical encapsulation of LiPS. (d) The soluble LiPS preferably diffuses within the hollow structure, or strongly anchors on MnO_2 nanosheets.[36-38]

1.4.3 Enhanced conduction and PS adsorption of composite sulfur host

To further intensify the Li-S performance, the sulfur immobilizer should deliver expedite electron conduction and strengthened PS adsorption. Therefore, design hybrid composite sulfur cathode is a common method to effectively boost charge transfer and sequester LiPS by incorporating carbon matrix with affinity additives.

Recently, a series of polar carbon sulfur hosts have been developed. For instance, heteroatom doping[34] and surfaces functionalization[39, 40] of carbon materials lead to significant improvement of chemical adsorption of LiPSs. Taking advantage of the Lewis acid–base interactions with PS, metal organic frameworks[41, 42], MXene nanosheets[43] and metal oxides[44] have been employed as sulfur hosts and perceived decent cycling stability. Polar metal oxides/sulfides, such as SiO_2[45], TiO_2[46], Co_9S_8[47], $NiCo_2O_4$[27] can also strongly adsorb PS and provide significantly improved cycling properties. By employing carbonaceous material as matrix and polar materials additives, an improved electron conduction and PS adsorption capability were realized. Li et al.[48] presented a new strategy by introducing anthraquinone (AQ), a small molecule organic compound, as additives in graphene (Gr) as composite sulfur immobilizer (Figure 1.5). The keto groups of AQ play

a critical role in forming strong Lewis acid-based chemical bonding. The AQ exhibits strong π–π stacking with Gr and chemical affinity with LiPS, rendering enhanced electron conduction and suppressed LiPS dissolution to promote long-cycling Li-S batteries. Comparing with the PS adsorption on Gr, the BE values of AQ is in the mid-range of chemical bonds intensities, implying that the redox reaction between PS species and the AQ molecules are highly reversible.

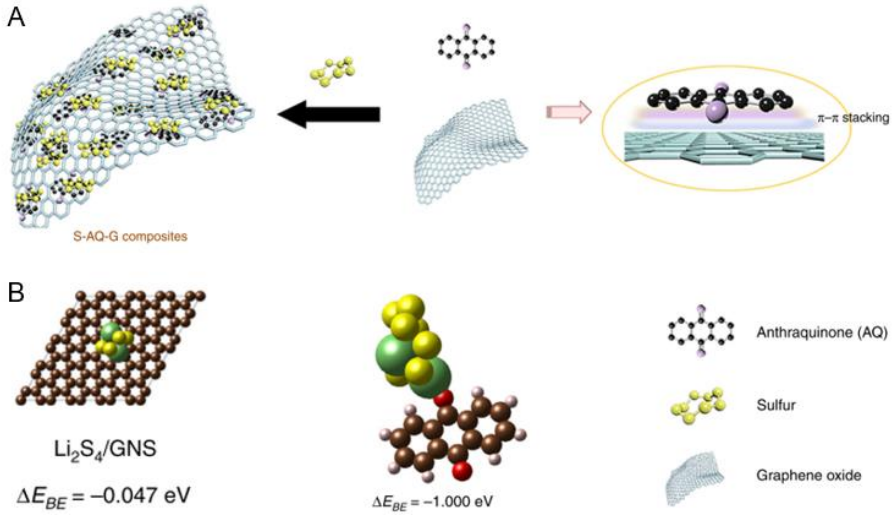

Figure 1.5 (A) Schematic illustration of the preparation of AQ-Gr sulfur composites and (B) the BE comparison of Li_2S_4 on Gr and AG.[30]

1.4.4 Emergence of nanostructure design strategies

It would never be realized the practical application of Li-S battery without rational structural/component design of appropriate electrode materials. The combination of materials with rationally designed structures is expected to show advantages over the strategy of simply mixing several components. Meanwhile, a synergistic effect is expected to be realized by constructing a micro/nanosized architecture, which is capable of enhancing sulfur utilization, suppressing LiPS shuttle effect and accelerating redox kinetics,

thus ameliorating the remaining challenges. The emergence of nanostructure design in sulfur cathode engineering significantly improve its structural stability and performance, promoting the revolution of sulfur cathode towards its practicability.

1.4.5 Morphology control

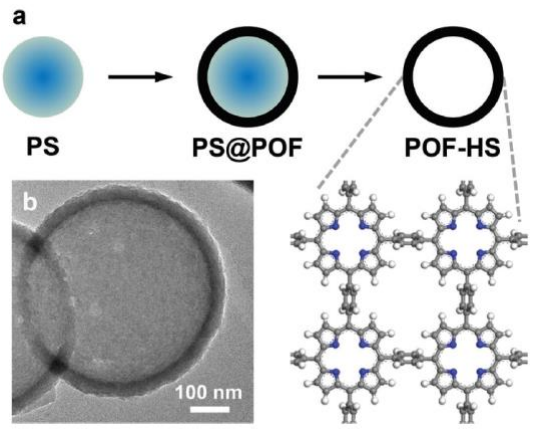

Figure 1.6 The concept of hollow spherical organic frameworks. (A) Schematic for the synthesis of POF-HSs. The amplified image is the periodic structure of single-layer POF. (B) TEM image of POF-HS with the typical hollow spherical morphology.[30]

Numerous researches have paid attention to design sulfur immobilizer with porous and/or hollow structure with large surface-to-volume ratio.[49] The porous structure with large hollow voids offers empty space a not only alleviate the volume expansion of S on lithiation but also structurally restrict soluble LiPS within the structure. The small dimensions of the hollow nanocomposites facilitate both ion and electron transport, leading to a better utilization of sulfur. Li et al.[50, 51] reported a new synchronously tactic to deliver porphyrin organic framework hollow spheres (POF-HS) with controllable morphology, which can be regulated in terms of void size and shell thickness (Figure 1.6). Benefited from the polar chemical structure and the hollow spherical morphology, POF-HS sufficiently migrates the

PS shuttle effect benefited from the strong physical and chemical sulfur confinement. Besides, the size and shell thickness can be easily tuned by controlling the size and content of template (Figure 1.7). By regulating its void size and shell thickness of POF, a structure-performance relationship was determined, which further guide the material design towards desirable performance.

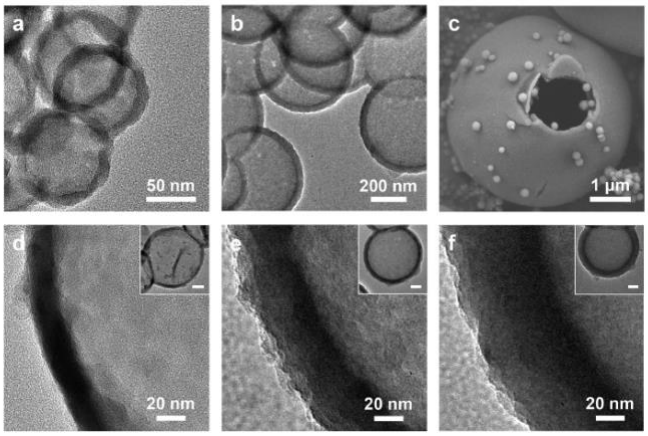

Figure 1.7 Morphology characterization of POF-HSs varying in void size and shell thickness. TEM images of (a) s-POF-HS and (b) POF-HS. (c) Scanning electron microscope (SEM) image of l-POF-HS. TEM images of (d) f-POF-HS, (e) POF-HS, and (f) t-POF-HS, respectively. Scale bars in the inserted TEM images are 100 nm.[49]

1.4.6 Defect architecture engineering

Defect engineering has been long considered as a facile surface engineering strategy to introduce more active sites for increased intrinsic activity of electrocatalyst.[49] Defect structures in metal compounds include intrinsic defects, extrinsic defects and non-stoichiometric defects.[52] The intrinsic defects consist of lattice vacancies without changing the composition or stoichiometry of metal compounds but affect the atoms around the vacancies and thus altering their physiochemical properties.[53, 54] The extrinsic defects that

introducing foreign atoms or ions into crystal lattices can break the original atomic arrangement and induce partial lattice distortion, which result in charge redistribution and electronic structures modulation.[55, 56] The non-stoichiometric defects can alter both the chemical composition and crystalline structure and exist mainly in compounds containing volatile elements which are greatly affected by temperature and ambient atmosphere.[28, 57] The synchronous implantation of miscellaneous defects formed on the surface can alter inherent properties such as energy band structure, surface adsorption and activity, which plays important roles in promoting electrocatalytic behavior.[58, 59]

Among these defects, anion vacancies are prevalent because of their low formation energy and capability to perturb the surface structure and provide more active centers by reduce atom coordination numbers, as evidenced by many experimental studies and theoretical calculations.[60] Several facile and controllable strategies have been developed to engineer the formation of anion vacancies within metal compounds, which contains three aspects that well-recognized by scientific community: chemical reduction, thermal treatment and force induction.[61] The chemical reduction, which contains reduction gas (NH_3, H_2) treatment[62], reduction liquid ($NH_3 \cdot H_2O$, $NaBH_4$ solution) treatment[63], and reduction solid (carbon, lithium, sodium) treatment[64] are generally used in material engineering to employ vacancies on the surface of materials. Li et al.[61, 64] utilized a simple ammonia treatment strategy to introduce oxygen vacancies into three-dimensional ordered mesoporous (3DOM) TiO_xN_y material to alter its electron conduction close to metallic feature. Meanwhile, the massive anion vacancies on its surface further act as adsorption sites to confine Co atoms, which facilitates ultrafine Co nanocluster nucleation, rendering efficient and durable electrocatalytic behavior (Figure 1.8).

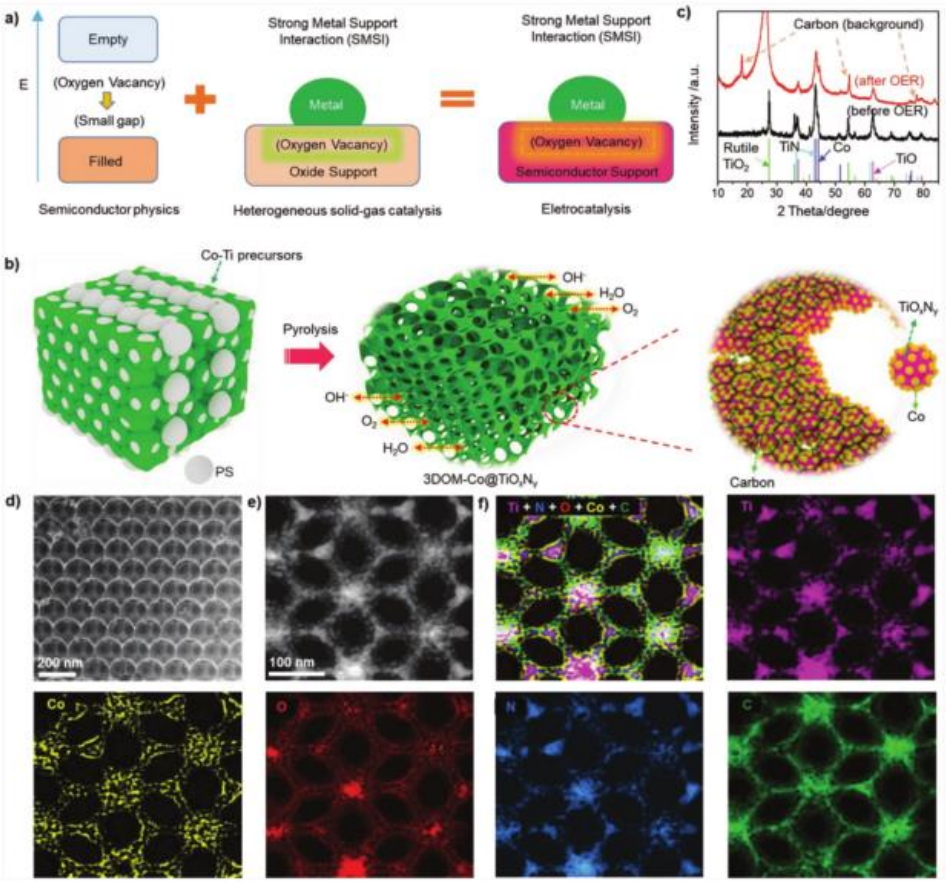

Figure 1.8 (A) The designing strategy for semiconductor-supported metal as electrocatalysts; (B) schematic of preparation procedure for 3DOM-Co@TiO_xN_y catalyst, and the Co interface-confinement effect; (C) XRD patterns of 3DOM-Co@TiO_xN_y before and after OER reaction; d) SEM; e) STEM image; and f) EELS elemental mapping (Ti, Co, O, N, and C) of 3DOM-Co@TiO_xN_y.[65]

Thermal treatment is also a common strategy to create vacancies, which involves thermal annealing or burning of material in oxygen deficient environment.[58] For example, Zheng et al.[66] activated and optimized 2H-MoS_2 basal planes through sulfur defect and strain engineering by Ar treatment to deliver a new hydrogen evolution reaction (HER) catalyst. The hydrogen adsorption free energy can be further manipulated by straining the surface

with S-vacancies, which fine-tunes its catalytic activity. Proper combinations and optimization of vacancies and strain result in an optimal adsorption energy of 0 eV, which exhibits the highest intrinsic HER activity among molybdenum-sulphide-based catalysts. Another frequency tactic used is force-induced strategies, which comprises plasma-assisted methods, ultrasonic treatment and microwave-assisted strategy.[58] Taking advantage of the etching and reducing functions of Ar plasma, Zhang et al.[67-69] prepared S-deficient Co_3S_4 ultrathin porous nanosheets as HER electrocatalyst. Impressively, the authors also extended this plasma-assisted dry exfoliation method to engineer Se vacancies in ultrathin $CoSe_2$ and $NiSe_2$ nanosheets, rendering a highly distorted structure and high electrical conductivity. The successful implantation of defect engineering in electrocatalyst design inspired the Li-S battery researchers to investigate the electrocatalytic behavior of sulfur immobilizer and the kinetic enhancement driven by defect introduction. Zhao et al.[70] developed an *in-situ* etching strategy to activate the inert sulfur immobilizer to realize its multifunctionality. By etching the iron atom *via* surface reaction with PS, the perceived $Ni_3Fe_{1-\delta}N$ exhibits enhanced LiPS conversion kinetics, leading to a high rate capability (Figure 1.9). This work opens up the exploration of defective materials and unveil their underlying mechanisms in kinetic regulation for high rate performance.

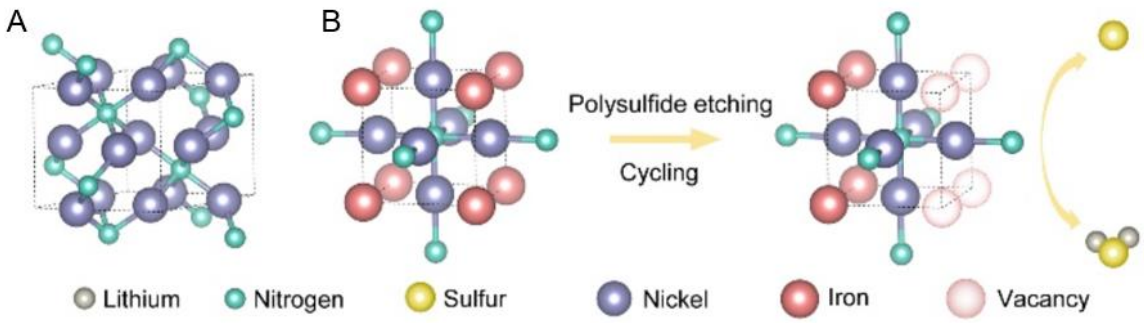

Figure 1.9 (A) Atomic structure model of hexagonal Ni_3N, (B) Atomic structure model of cubic Ni_3FeN and schematic illustration of PS etching process toward active $Ni_3Fe_{1-\delta}N$ phase.[71]

1.4.7 Ultrafine structure design

Although defect engineering endows the sulfur host with admirable Li-S kinetics improvements, the rate capability is still limited, especially under high C-rate, attributed to the low active surface given by microsized particles. The insufficient active interfaces result the incomplete conversion reaction of S/Li_2S. Therefore, it is crucial to design catalyst with refined particle size in atomic level. Recently, many sub-nanosized and atomically dispersed materials haven been developed as multifunctional sulfur immobilizer to accelerate the conversion kinetics. An atomically dispersed cobalt single atom catalyst has been introduced, which is able to trigger the surface-mediated reaction of LiPS (Figure 1.10).[72] Its structural information was revealed by XAS results, which indicates that Co atoms are embedded in the N-doped graphene lattice and are coordinated to N atoms to form Co−N−C coordination centers. The optimized structures of the intermediates and their Gibbs free energy profiles reveal the spontaneous exothermic conversion from S_8 to Li_2S, which indicates that the reduction of S is thermodynamically more favorable on Co−N/G than on N/G substrate. Thus, the ultrafine nanostructure is expected to confer an expedite redox reaction kinetics to promote the complete LiPS transformation and catalytic conversion.

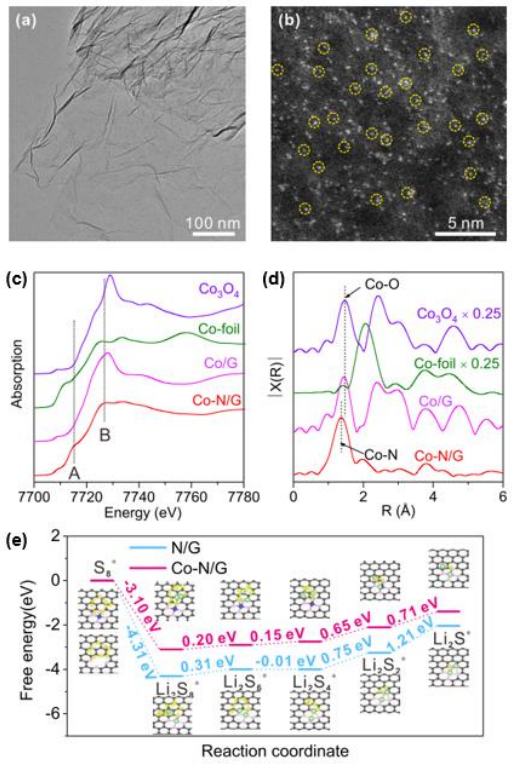

Figure 1.10 Structure of the Co−N/G composite. (A) TEM and (B) HAADF-STEM images of Co−N/G. (C) XANES and (D) FT-EXAFS in R space for Co−N/G and reference samples including Co/G, Co-foil, and Co_3O_4. (E) Energy profiles for the reduction of LiPSs on N/G and Co−N/G substrates. (inset figure) The optimized adsorption conformations of intermediate species on N/G and Co−N/G substrate.[71]

1.5 Lithium anode protection

On the anode side, severely electrode pulverization and dendrite formation will occurred during cycling, leading to battery failure.[72] The main reason is the insulating SEI film that spontaneously forms on the surface of the strongly reductive lithium surface. SEI are lithium ion conductive but electrically insulating.[73] The uneven Li electrodeposition process could continuously break SEI and reform, leading to thick SEI formation. Large

amount of electrolyte will be consumed when contact with the fresh exposed Li, causing low coulombic efficiency and fast capacity fading. Higher current densities associated with a raised sulfur loading results in higher depth of discharge and huge volume fluctuation of lithium metal anode (LMA), rendering electron disconnection and Li dendrite growth.[74] The sharp dendritic Li sprout out could pierce the separator, leading to severe safety concerns. An illustration of failure of LMA is shown in Figure 1.11.

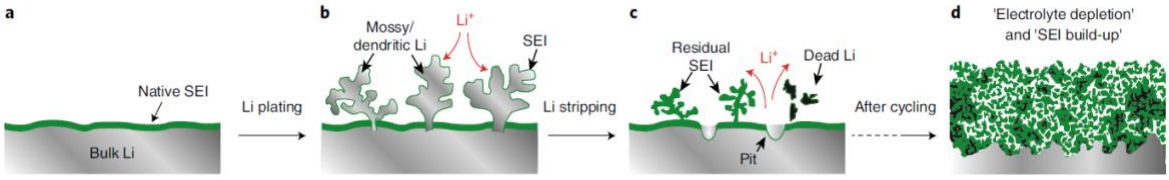

Figure 1.11 Schematic showing the Li stripping/plating and dendrite growth process.[75] Step a: Li plating induces the SEI film cracking. Step b: further plating causes Li dendrites to shoot out through the cracks. Step c: Li stripping produces isolated Li, leading to 'dead' Li accumulation. Step d: Continuous cycling causes steps 1-3 to occur repeatedly, confer to accumulated dead Li, thick SEI and porous Li electrode.

To gain insight for the dendrite growth mechanism, two type of models, tip dendrite growth mode and mossy dendrite growth were introduced. The mossy dendrite mode occurs when the mass transfer during lithium deposition is limited by SEI due to its low Li^+ conductivity and non-uniformity. The impact of this type of dendrite will slowly consume the finite amount of electrolyte solvent and eventually "dry out" the cell. The tip growth mode takes place at a sufficiently high current density when the Li^+ concentration that closed to interface drop to zero and will maintain a zero-lithium concentration, leading to preferential tip growth during Li deposition. The non-uniform deposition of lithium is

further promoted and amplified by subsequent topographical changes in the anode's surface in a fractal-pattern type manner. The impact of this type of dendrite is even worse compared to those of the mossy growth mode cause the tip dendrite growth is non-reversible and intensified during cycling, which finally penetrate separator and reach to cathode, causing short circuit and severe safety issues.

Numerous efforts, such as employing electrolyte additives, designing artificial SEI layer, developing host structure, introducing high concentration electrolyte and optimizing electrolyte component, have been attempted to construct a stable SEI towards improved LMB performance.[76] For instance, deep eutectic solvent (DES) based self-healing polymer electrolyte (DSP) to enable a dendrite-free LMA, which simultaneously possesses non-flammability, high ionic conductivity and decent electrochemical stability (Figure 1.12).[77-79] A more homogeneously distributed Li^+ flux can be achieved on the interface of DSP/LMA based on their COMSOL simulation conclusion. This uniformed Li^+ flux efficiently stabilizes the Li electrodeposition owing to its mesh size much smaller than the nucleation points, leading to a dendrite-free Li deposition. These key findings provide a deep insight to inspire progresses in the development of highly safe and durable Li-S batteries.

1.6 Electrolyte modification

The dissolution and dissociation of generated LiPS intermediates in electrolyte during discharge/charge process drastically increases the electrolyte viscosity and decreases the electrolyte wettability as well as conductivity, which deteriorates Li-S kinetics. Therefore, electrolyte modification toward inhabited dissolution of sulfur species is at stake. Besides, the low boiling point and flammable ether-based electrolyte in Li-S battery is able to be

ignited when thermal runaway occurs, which usually end up with battery fire, or even worse, explosion.

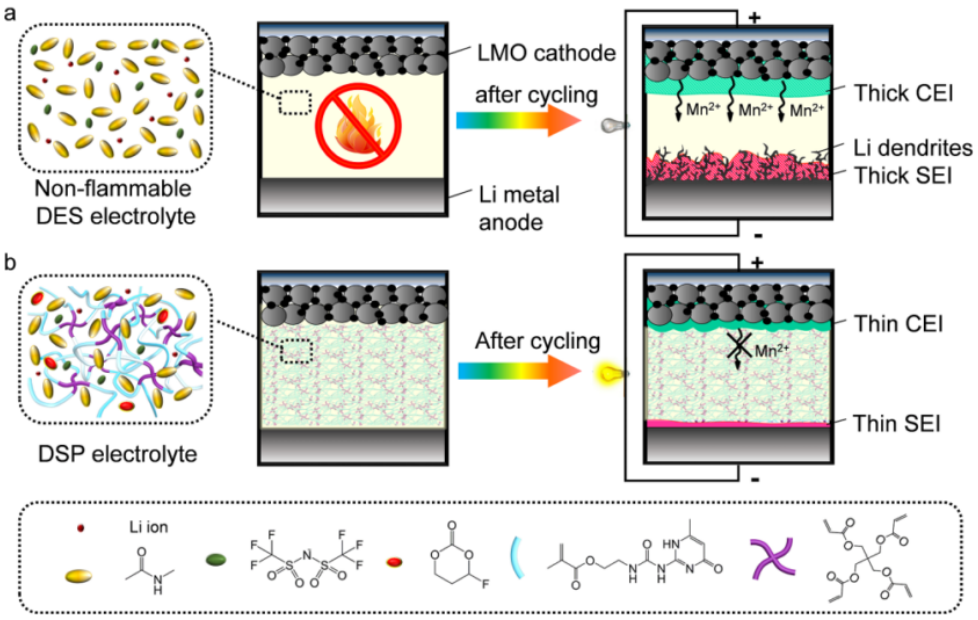

Figure 1.12 Schematic illustration of (A) the DES and (B) DSP electrolytes in Li||LMO cells.[80]

To alleviate these problems, solid-state electrolytes (SSE) have been widely recognized as the ultimate solution for future battery technologies due to their excellent safety performance, including high chemical, electrochemical, thermal, and mechanical stabilities as well as its capability of suppress Li dendrite formation when substituted SSE over liquid electrolyte. However, due to the intrinsically low conductivity of S/Li_2S and the poor solid-solid interfacial contact between sulfur and SSE, the all-solid-state Li-S batteries suffer from low conductivity, sluggish kinetics, and poor rate capability. Besides, many problems such as compatibility, air/moisture sensitivity and manufacturing difficulties of SSE still need to be solved to fully realize its large-scale production.

1.7 Interlayer and separator design

Functional interlayer/separator also impacts Li-S performance, which is capable of building up ion selective shield to block PS diffusion from cathode to anode and simultaneously provide satisfactory Li^+ conductivity, contributing to a significant inhibition of PS shuttling. The illustration of typical interlayer/separator towards PS shuttle inhabitation is shown in Figure 1.13.

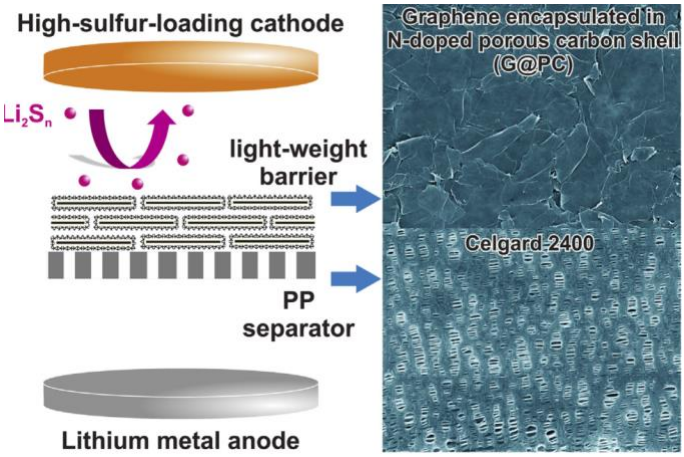

Figure 1.13 Schematic Illustration of the functional separator for suppressed PS shuttle effect.[85]

Recently, Zhou et al.[80] developed a metal-organic framework based separator to manipulate the PS diffusion. Similar shuttle effect suppression is realized by anion-repelling of surface functionalized separator.[81] Apart from that, interlayer design can also provide effective PS confinement and enhanced electrochemical reaction kinetics by capturing and reutilizing PS anions. Many functional materials, such as carbonaceous materials,[82] metal compound[83] and functional polymers[84] are widely used as absorber and promoter in interlayer. Obviously, interlayer/separator designs have experienced an extraordinary rise in achieving high-efficiency Li-S batteries.

1.8 Practical application requirement

Albeit many admirable electrochemical performances have been reported in literatures, their performance was always evaluated under low sulfur loading and flush electrolyte content in the cell. Under this circumstance, the material usually manifests superior mass/charge transportation and limited electrode volume expansion, leading to extraordinary Li-S electrochemistry. However, the practical utilization requires the sulfur cathode with high sulfur loading and low E/S ratio to deliver high discharge capacity and energy density in the cell level. A huge gap still remains between the state-of-the-art Li-S performance and the strict commercial standards. Therefore, extensive explorations should be devoted to study the shuttle and electrocatalytic behavior of PS under practical relevant conditions. Instead reporting the capacity based on the mass of active materials, the performance evaluation of sulfur electrode is suggested to take into account all the battery shells, electrodes, electrolytes, etc. Therefore, significant progress is needed to boost the practical battery performance.

To achieve decent gravimetric and volumetric energy density for practically viable Li-S batteries, the electrode should contain a high S loadings and lean electrolyte/sulfur (E/S) ratio based on the simulation result.[86] Also, the cycle life of Li-S batteries under high S loadings and low E/S ratio is still far from that of commercial Li-ion batteries.[87] The huge sulfur volume expansion and sluggish redox reaction kinetics issues on the cathode and the electrolyte consumption and exacerbated Li dendrite growth problems on the anode significantly hamper the cycling stability of Li-S batteries.

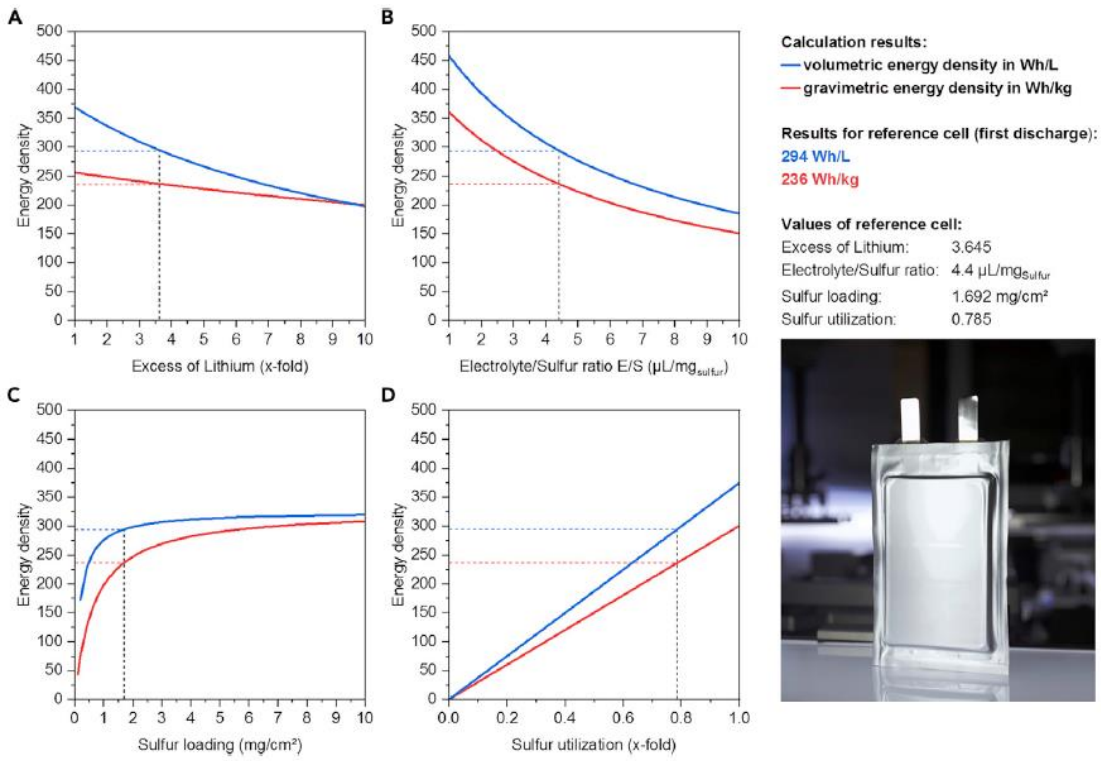

Figure 1.14 Modeled volumetric (A) and gravimetric (B) energy densities of a hypothetic Li-S cell. Projected Energy Density (Gravimetric and Volumetric) of the Reference Cell The amount of Li-excess (A), electrolyte/sulfur E/S ratio (B), sulfur-loading (C), and sulfur utilization (D).[88]

Dorfler et al.[88] reported the sensitivity analysis of the energy density of Li-S pouch cell, which indicates that the sulfur loading has low impact on energy density enhancement above 3 mAh cm^{-2} (Figure 1.14C). However, reducing the E/S ratio is essential to achieve both high gravimetric and volumetric energy density (Figure 1.14B). Owing to the low mass density of Li metal, the anode excess limits the volumetric energy density much more than the specific energy (Figure 1.14A). Also, enhancing the sulfur utilization to realize a high discharge capacity above 1300 mAh g^{-1} is also critical for high energy density Li-S batteries. This simulation result means that design highly active sulfur immobilizer with

enhanced LiPS conversion kinetics to promote the completely Li_2S transformation has significant meaning for Li-S batteries. In view of these design strategies, the obstacles, the developing tactics and the future applications also differs on their ways to high energy storage and commercialization. Therefore, rationally designed electrode configurations toward sparing electrolyte usage and raised sulfur loading is another critical aspect that need more research efforts for Li-S batteries.

The main objectives for this thesis are: (1) design novel transitional metal compounds architecture and evaluate its capability and suitability when employed in Li-S systems; (2) understand how rational structure design influence the properties of sulfur host and its Li-S performance; (3) contribute to an innovative material synthesis strategy to design multifunctional sulfur immobilizer for advanced Li-S battery technologies.

1.9 Structure of thesis

Figure 1.15 depicts a breakdown of work conducted throughout this thesis. This thesis is organized in seven chapters. **Chapter 1** introduces the background, challenges, contemporary research progress of Li-S batteries, and structure of the thesis work. **Chapter 2** describes the main characterization techniques used throughout this thesis. **Chapter 3** introduces a facile strategy to synthesis multishelled cobalt based transitional metal oxide hollow sphere material with tunable composition and shell numbers as sulfur host to enhance its sulfur confinement and evaluate the multishelled structure-performance relationship. **Chapter 4** presents a universal strategy to synthesis double-shelled cobalt based transitional metal oxide porous hollow sphere material. The defect engineering of cation substitution by replacing Co^{3+} with Ni^{2+} is capable of introducing immense oxygen

defects in the octahedral sites. The superior Li-S performance was realized when employing it as sulfur stockpile and the strong chemical interaction between oxygen defects and LiPS is fully illuminated. **Chapter 5** depicts a three-dimensional ordered mesoporous cobalt sulfide material as sulfur immobilizer and the anion defect engineering, which tunes part of CoS_4 tetrahedron intro CoS_6 octahedron by replacing N with S, creates numerous sulfur defects in its octahedral sites. The fundamental mechanism of LiPS adsorption and catalytic conversion on sulfur defects is unveiled. **Chapter 6** describes the attempt and evaluation of implanting highly dispersed cobalt sulfide in porous carbon as host material for Li-S batteries. It also highlights the development of 3-pronged Nb_2O_5 ultrafine nanoarchitecture porous carbon implantation, of which the defective state, crystallinity and inlaid particle size can be delicately manipulated by controlling the pore diameter of carbon and annealing atmosphere, for expedite Li-S performance. The homochronous combination of defect engineering, crystallization tactic and nanoreactor design endows the sulfur immobilizer with multifunctionality, which incorporating high sulfur utilization, strong PS adsorption and fast LiPS catalytic conversion, rendering superior rate capability and cyclic stability when employed it as sulfur cathode. **Chapter 7** summarizes the important results and offers some discussions on the future direction that the work may take.

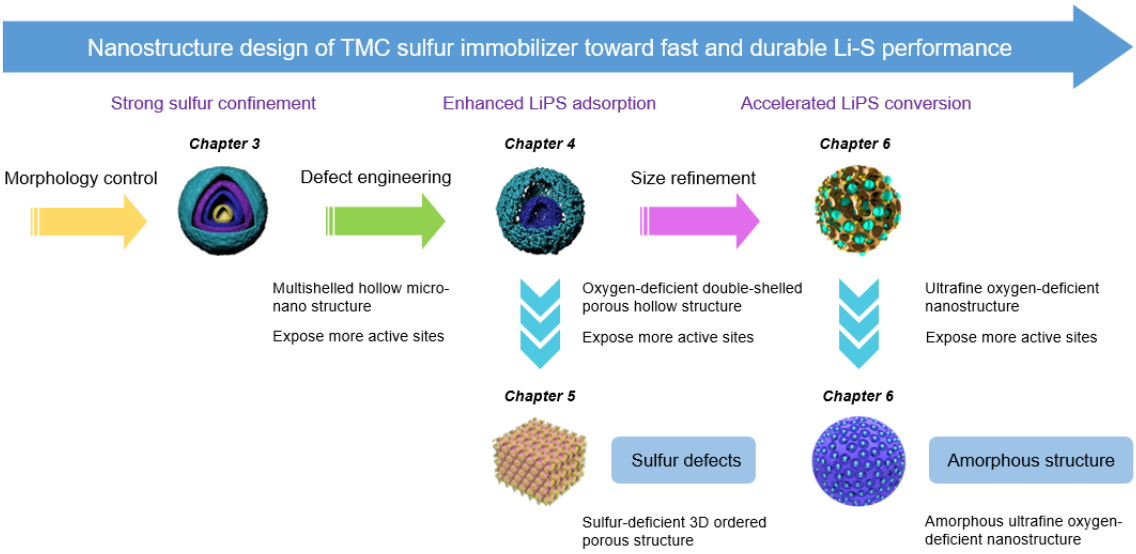

Figure 1.15 Schematic illustration of the research topics throughout this thesis.

Chapter 2 Experimental Methods and Characterization Techniques

2.1 Electrodes and electrolytes preparation

The cathode material of Li-S batteries can be made from the charged species (elemental sulfur) or the discharged species (Li_2S). The sulfur cathodes in this thesis were all prepared based on elemental sulfur that is thermally infiltrated into the host materials by melt-impregnation method. Typically, sulfur was grinded in mortar with the host material by a desired mass ratio. Then the mixture was transferred into a small vial and heated at 155 ^oC for 12 hours. The final active material was acquired after hand grinding into powder.

The electrodes were prepared by mixing the sulfur composites, conductive agent and binder with a desired ratio (wt%, 8:1:1 or 7: 2: 1), hand grounding in the NMP solvent for 30 mins. Then the slurry was cast on Al foil (MTI, 15 μm thickness) by doctor blading or carbon paper (SGL Group, 190 μm thickness) by drop casting, respectively. The electrodes were then dried at 70 °C overnight.

The electrolyte used for electrochemical characterizations is 1 M LiTFSI and 2 wt.% of $LiNO_3$ in a mixed solvent of DOL and DME with a volume ratio of 1:1. All the electrolyte preparation was conducted inside the Ar filled glovebox (Mbraun) with a water and oxygen level below 0.5 ppm. The 2032 coin cells were used for battery assembling. Li metal plate (450 μm) was used as the anode and specified amount of electrolyte was used. Celgard 2325 was used as the separator.

2.2 Physical characterization

2.2.1 X-ray diffraction (XRD)

XRD is a versatile characterization technique which allows the determination of crystal structure and atomic spacing. X-rays are employed to generate the diffraction patterns at

the angles corresponding to specific crystal. The X-rays interact with the sample to produce diffraction patterns at the angles corresponding to specific crystal planes and then are collected, processed and counted by the detector, as shown in Figure 2.1. The angle of diffraction is related to the specific crystal orientation of the sample by Bragg's law as shown by Equation 2-1 below:

$$n\lambda = 2d\sin\theta \qquad (2\text{-}1)$$

where n represents the order of the spectrum, λ is the wavelength of the incident X-rays, d is the lattice spacing, and θ represents the incident angle. The diffraction pattern at specific angles obtained by XRD can be used to calculate the crystalline planes to identify its structure.

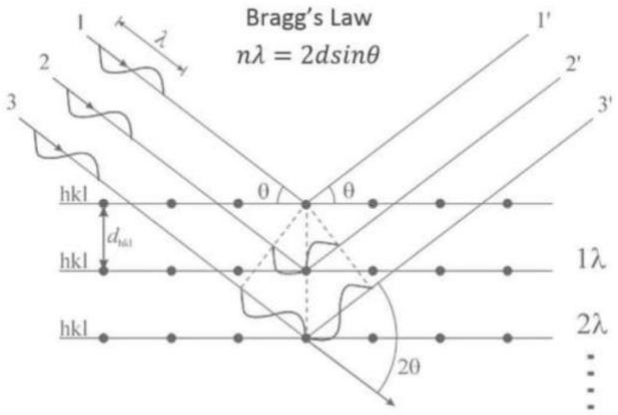

Figure 2.1 Schematic illustration of X-ray diffraction.

2.2.2 Scanning electron microscopy (SEM)

SEM is an important imaging tool to reveal the morphology and topological features of materials which is much sensitive to the surface information. The principle of image-forming is illustrated in Figure 2.2. It involves illuminating the sample with an electron beam, and projecting images based on collected secondary or backscattered electrons. After

collecting signals by detectors, it creates a real-time image on computer to display the morphology of the sample. In this project, SEM will be used to investigate the surface morphology of the materials.

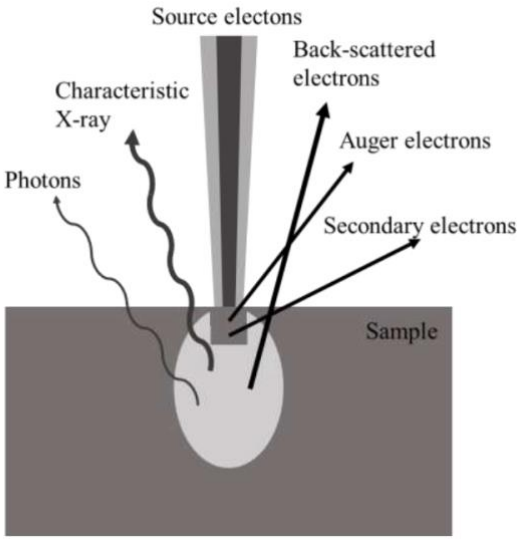

Figure 2.2 The principle of SEM.

2.2.3 Transmission electron microscopy (TEM)

TEM is widely used for analyzing the structure information of materials. In this characterization, a beam of electrons, which is ejected from the electron gun, will transmit through an ultra-thin specimen and collected by detector. TEM allows direct visualization of samples' morphology on the nanometer scale. High resolution TEM imaging even manifests atomic level morphology. Based on electron diffraction theory, the signals from the collected diffracted electrons can be processed to produce a high resolution image of the sample. The lattice distance and crystal structure can be further revealed by selected area electron diffraction.

2.2.4 Brunauer-Emmett-Teller (BET) method

BET theory is used to explore the physical adsorption of gas molecules on a solid surface, which is an important analysis technique for the measurement of the specific surface area of porous materials. BET theory builds upon the foundational Langmuir monolayer molecular adsorption theory and extends this theory to multilayer adsorption, assuming gas molecules can adsorb on a solid surface in an infinite number of layers and individual adsorption layers do not interact with other layers and Langmuir theory can be applied to each individual adsorption layer.

Therefore, the BET equation can be derived as shown in Equation 2-2:

$$\frac{1}{[\nu\left(\frac{p_0}{p}\right)-1]} = \frac{c-1}{\nu_m c}\left(\frac{p}{p_0}\right) + \frac{1}{\nu_m c} \qquad (2\text{-}2)$$

2.2.5 Energy dispersive X-ray spectroscopy (EDX)

EDX is commonly incorporated into SEM and TEM to identify and quantify the chemical compositions of samples. EDX is based on the emitted characteristic X-ray from the process of the ejected electrons on the outer shell jumping into the partially empty inner shell. It involves bombardment of the electron beam onto the sample surface which results in the emission of X-ray collected by a detector. The binding energy of the emitted X-ray and their corresponding intensity are specific to certain elements, allowing their appropriate identification and quantification in the sample being investigated. EDX is widely used for the elemental analysis because of the unique set of X-ray emission peaks of each element. Elemental mapping can also be created, which is helpful in analyzing the localized elements over a selected area of the sample. Variations in the emitted X-ray intensities indicated variations in the specific atomic contents at those locations and can be

used to map the concentration of different elements over the entirety of the sample being investigated.

2.2.6 X-ray photoelectron spectroscopy (XPS)

XPS is a surface characterization technique that allows investigation of the elemental composition, chemical state and electronic states. In principle, the sample is exposed to X-rays with a specific energy. These X-ray photons, upon interaction with the sample, will cause the emission of electrons. As a result, the number of electrons that escape from the material's surface (up to 5 nm) are detected and analyzed based on the electron binding energy (BE). In this project, XPS is mainly utilized to identify the elements in the developed sulfur host and indicates the chemical interactions with LiPS.

2.2.7 Thermogravimetric analysis (TGA)

TGA is a technique where the weight change of a sample is measured as a function of temperature. Samples can also be exposed to different atmospheres as they are being heated during TGA. A typical TGA measures the sample weight with a precision balance while purging the heated region with the desired type of gas. The heating is done in a small furnace and the temperature is precisely measured with a temperature resistance probe in close vicinity to the sample holder. A platinum sample holder is used in this research study.

2.2.8 Raman spectroscopy

Raman spectroscopy reflects the interaction of photons with the vibrational, rotational or other low-frequency modes of a molecule. The Raman effect of photons describes the condition when photons interact with the polarizable electron density, the chemical bonds of the molecule and the environment it finds itself. Specifically, a photon excites the molecule that is in either the ground rotational/vibrational state or an excited state, resulting

in the molecule being in a virtual energy state for a short period of time. At the same time, the photon is then inelastically scattered, which can be of either lower (Stokes) or higher (anti-Stokes) energy than the incoming photon. The difference in energy between the original state and the resulting state leads to a shift in the wavelength of the scattered photon from the excitation wavelength.

2.2.9 X-ray absorption spectroscopy (XAS)

XAS is a synchrotron radiation technique that can be used to explore the atomic/electronic structure and geometric/bonding information of materials. The spectrum is obtained by collecting the absorption coefficient as a function of photon energy in a desired energy region, which consisting three regions: the pre-edge, X-ray absorption near-edge structure (XANES) and extended X-ray absorption fine structure (EXAFS). The first two regions are related to the excitation of core electrons to free orbitals to reveal the electronic states. The last region comes from the scattering of the ejected photoelectrons with the neighboring atoms and thus reflects bonding information.

2.2.10 PS absorptivity

PS absorptivity was evaluated by UV-vis spectra, which determines the amount of residual LiPS in solution after contact with the respective host materials. Internal standard method was employed to prepare calibration baseline. Sample solutions were prepared by stirring a known mass of materials in a known concentration of Li_2S_6 in THF solution. The mixture was static settlement overnight and the supernatant was collected. This solution was further transferred to UV-vis equipment and its adsorption spectroscopy was collected. The absorptivity was then calculated by subtracting the starting amount with adsorption amount. All procedures were performed in an Ar-filled glovebox.

2.3 Electrochemistry methods

2.3.1 Galvanostatic charge discharge technique (GCD)

GCD profile refers to the electrochemical cycling method where a constant current is applied to a cell until a certain amount of charge has been passed or a voltage cut-off has been reached. In the field of battery research, usually a negative current force discharge and a positive current force charge of a cell.

GCD profile is one of the most important and widely used electrochemical characterization technique for research in Li-S battery and even all types of batteries. On one hand, it mimics the battery operating conditions in practice, where a constant power is desired (assuming voltage is constant in this region). On the other hand, it presents a way to understand the maximum number of Li^+ charges that can be stored in the electrode or depleted from the electrode. Also, the potential of Li^+ storing/depleting processes can be illuminated. Through this we can learn the specific charge and discharge capacity of an electrode and get the thermodynamics/kinetics information about these processes. A curve that plots the voltage response as a function of specific capacity is usually used to present the basic electrochemistry, as shown in Figure 2.3. For Li-S battery, the discharge curve of GCD profile shows two voltage plateaus.

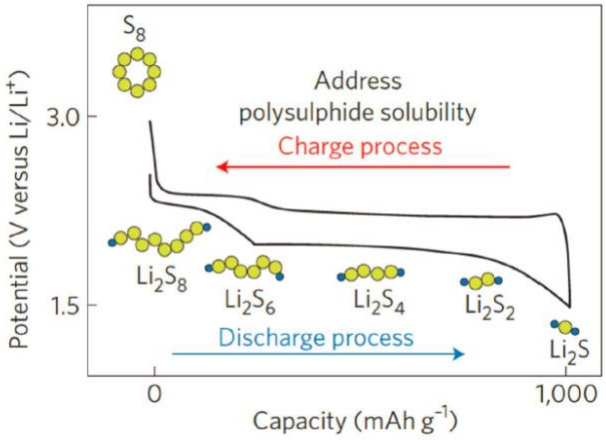

Figure 2.3 A typical GCD profile of Li-S batteries that base on conventional ether electrolytes. The lower curve represents discharge process while the upper curve represents the charge process. Structural evolution of the sulfur species upon discharge is represented, from element sulfur to PS to Li_2S.[87]

2.3.2 Cyclic voltammetry (CV)

CV is a potentiodynamic electrochemical measurement technique used to analyze the electrochemical reactions. During testing, the working electrode potential is cycled linearly at a certain potential scan rate (i.e., at 0.1 mV/s) within a desired voltage window. In this research, CV is used to confirm the potentials at discharge and charge process as well as to identify electrochemical reactions of PS.

2.3.3 Electrochemical impedance spectroscopy (EIS)

EIS is a widely used tool to diagnose the impedance of batteries by recording the current response to an applied sinusoidal potential at varying frequencies. Among various ways to present the spectrum, the so-called Nyquist plot is commonly used in the battery field by plotting the negative of the imaginary part of impedance versus the real part for different frequencies. The Nyquist plot usually consists of one or more semicircles at high frequencies (which are charge transfer processes) and a linear tail at low frequencies (which is diffusion process). EIS data are commonly analyzed by fitting the curve with an equivalent circuit model to understand the contribution from each component.

Chapter 3 Tuning shell number of Multishelled Cobalt Oxide Microsphere Sulfur Host for durable Li-S performance

3.1 Introduction

Lithium-sulfur (Li-S) batteries are regarded as one of the most promising candidates for next-generation energy storage benefiting from the natural abundance, environmental benignity and high specific capacity of sulfur.[89] While the significant advantages are convincing, the wide-scale commercialization of Li-S batteries is so far limited because of some intractable technical challenges, which involve the ionically and electrically insulating nature of sulfur, the dissolution and shuttling behaviors of the intermediate lithium polysulfides (LiPS), and the large volume expansion during cycling.[90]

Addressing the PS adsorption is an important avenue to commercialize Li-S batteries. As mentioned in Chapter 1, initially nanostructured carbons with sophisticated pore structures were used to provide electron conductivity and physical entrapment of the LiPS. However, carbon-based material shows low chemical interaction with LiPS, rendering limited PS shuttling inhibition. Under these circumstances, polar materials such as transitional metal oxides (TMOs) have been developed as promising sulfur host for improved sulfur electrochemistry.[12, 91] Among TMOs, Co_3O_4 has drawn particular research interests due to its high electrochemical stability and adsorbability to LiPS, serving as a promising sulfur host.[92-94] However, the nanosized Co_3O_4 material is easy to agglomerate, which results in non-uniform sulfur distribution and insufficient active sites for redox reaction.[95, 96] The relatively poor electron conduction properties and low surface area of Co_3O_4 are greatly impeding its widespread implementation.[97] These instinct structural weakness results in a low sulfur utilization and sluggish kinetics of sulfur cathode. Therefore, structural design

offers a promising route to alleviate this problem.[98, 99] The construction of porous hollow structure is capable of facilitating ion access to the electrode matrix by offering sufficient ion transport pathways.[100] Comparing to single-shelled hollow sphere, multi-shelled hollow structure offers additional benefits such as high volumetric energy density, shell permeability and reduced aggregation of nanosized subunits.[16-18] The multi-shelled hollow structure also offers large interior void spaces to homogenize sulfur distribution and accommodate volume expansion during sulfur lithiation. The high porosity and large surface area of multi-shelled microsphere facilitates electrolyte infiltration and reduces Li-ion diffusion distance, rendering improved sulfur utilization and fast electrochemical kinetics.[101] Moreover, multi-shelled hollow sphere with more shells offers freedom to manipulate the properties of materials through the design and construction of multi-components with complex architectures to achieve enhanced properties.[102, 103] Precisely design the void interior to accommodate the sulfur volume expansion for enhanced structural integrity without sacrificing gravimetric and volumetric performance offers a new strategy to design huge volume effect material for required energy storage behavior. Therefore, a synergistic combination of well-designed composition and structure is promising to realize greatly improved Li-S performance. Some literatures have reported the synthesis of TMOs multi-shelled hollow sphere by vesicles, gas-bubble, or hard templating methods.[104-107] However, those strategies usually involve time-consuming processes and struggles to control the structures and components of the products. The development of versatile methodologies to synthesize porous hollow structures with multi-components and tunable number of shell and composition are still a great challenge.[108, 109]

In this chapter, we present a straightforward strategy for the synthesis of Co_3O_4 hollow microspheres with tunable shell number and composition as sulfur host. This economic and facile synthetic method delivers great universality and strong controllability on the morphology of the obtained hollow spheres by varying metal ion concentration, which makes it possible to systematically investigate the structure-electrochemical performance relationships. As for demonstration, Co_3O_4 quadruple-shelled hollow microsphere (Co_3O_4 QS-HS) was developed as sulfur immobilizer, which uniformizes sulfur distribution and offers abundant electrode/electrolyte interfaces to minimize electron transport and lithium ion diffusion. Furthermore, the creatively designed quadruple-shelled structure with empty interiors is flexible toward volume changes, which also provides potent sulfur confinement to inhibit the dissolution and outward migration of LiPS. Benefiting from the structural integrity and morphological/compositional advantages, Co_3O_4 QS-HS sulfur composite demonstrated the best discharge capacity and cyclic stability, holding great promises to be utilized as sulfur immobilizer in Li-S systems.

3.2 Experimental section

3.2.1 Synthesis of Co_3O_4 QS-HS

In this work, hydrothermal method was used to prepare the precursor. In a typical preparation process, 0.056 mol glucose ($C_6H_{12}O_6$) and 0.066 mol cobalt acetate $Co(CH_3COO)_2 \cdot 6H_2O$ were dissolved into 100 ml distilled water under magnetic stirring. Subsequently, the obtained solution was transferred into a 200 ml Teflon container, sealed in autoclave and hydrothermal reacted at 180°C for 400 min with a ramping rate of 5°C min^{-1}. The black precipitation was collected, washed and centrifuged with distilled water and ethanol for 3 times, the obtained powder was dried at 70 °C for 12 h and collected as

metal acetate polysaccharides (MAP) precursor. The final product was obtained by annealing MAP at 500 degree for 1 h in air, with a ramping rate of 1°C min^{-1}. The synthesis procedures of (Ni, Co, Mn)$_3O_4$ QS-HS is similar to that of Co_3O_4 QS-HS except for using nickel acetate, cobalt acetate and manganese acetate as reactants for (Ni, Co, Mn)$_3O_4$ QS-HS, respectively. The Co_3O_4 with different shell numbers were synthesized by adjusting the glucoses and metal ions in precursor.

3.2.2 Materials characterizations

TGA (TA instrument Q500) was conducted under air atmosphere with a heating rate of 1°C min^{-1}. Nitrogen sorption (ASAP 2020 micromeritics) was used to retrieve data which was analyzed using Brunauer–Emmett–Teller theory to calculate and in return, characterize the surface area. The SEM images was collected with a FEI Quanta FEG 250 SEM. The TEM images were collected using Phillips CM 12 and JEOL 2010F TEM. X-ray diffraction (MiniFlex 600 Rigaku) experiments were performed to determine the crystal structure. XPS was performed using a K-Alpha XPS spectrometer.

3.2.3 Electrochemical analyzation

Sulfur composites were prepared by immersing 0.3g Co_3O_4 QS-HS powder inside carbon disulfide (CS_2) solution, containing 0.7g sulfur, followed by a thermal treatment under 155°C for 6 h. The sulfur composites, conductive agent (Super P) and binding agent (poly(vinylidene fluoride, (PVDF)) were grinded and homogenized in *N*-Methyl-2-pyrrolidone (NMP) in a 7:2:1 ratio by ultrasonication and vigorous stirring overnight. Al foil (MTI Corporation) were used as the current collector and coated with the homogenous slurries, dried at 70°C and cut into small pieces with certain dimensions as electrodes. The electrochemical performance test was carried out in CR2032 type coin cell and the cells

were assembled with the prepared sulfur composite cathodes, anodes, electrolyte and separators in an argon filled glove box. The used electrolyte was 1 M LiTFSI dissolved in a mixed solvent of DOL and DME (1:1, v/v), containing 2 wt% $LiNO_3$. The average areal sulfur loading was ~1 mg cm_2. The cells were tested using a Land CT2001A battery tester. The EIS were measured in the frequency range from 100 kHz to 0.1 Hz with an amplitude of 10 mV.

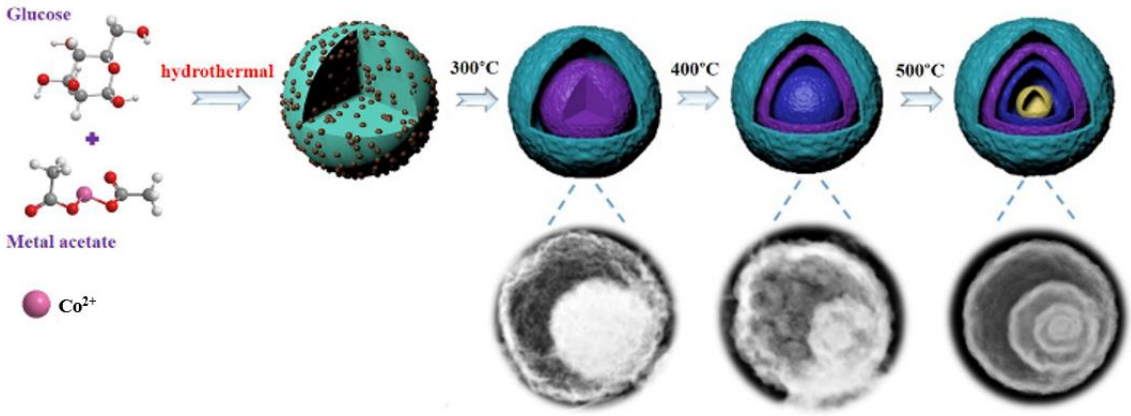

Figure 3.1. Formation process of Co_3O_4 QS-HS.

3.3 Formation and characterization of multi-shelled hollow microsphere

The conventional syntheses of TMOs are complicated and time consuming which usually require process such as template synthesis, ion-adsorption and template removal.[110] In comparison, we presented a novel and convenient route to prepare Co_3O_4 QS-HS by using MAPs as self-template. The synthesis method is well illustrated in Figure 3.1. Co_3O_4 QS-HS with uniform gap between adjacent thin shells are synthesized by hydrothermal method followed with thermal treatment. Firstly, a homogeneously mixed solution of metal acetates and glucose is prepared for hydrothermal reaction. During the glucose

polymerization process, metal cations are adsorbed onto the polysaccharides to form MAPs via an *in-situ* coordinating process, which involves intermolecular dehydration of glucose and simultaneous coordination of transition metal ions.[111-114] The adsorbed metal ions on the MAPs frameworks will further promote the growth of microspheres by acting as cross-linking agent and forming coordination bonds with free flowing glucose, resulting in carbonaceous spheres (CS) with uniformly distributed metal ions and expanded volume.[115]

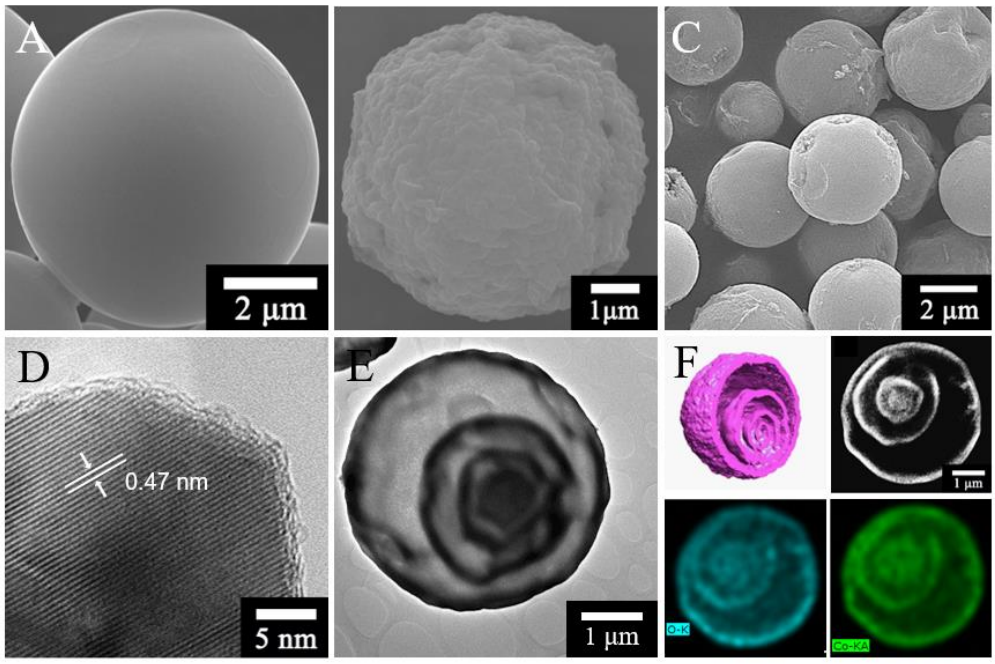

Figure 3.2. SEM images of (A) MAPs and (B, C) Co_3O_4 QS-HS. (D) HRTEM image of Co_3O_4 QS-HS. (E) TEM image of Co_3O_4 QS-HS. (F) 3D reconstructed image, STEM image and EDX element mappings of Co_3O_4 QS-HS.

Figure 3.2A-C shows SEM images of MAPs and Co_3O_4 QS-HS with micro-spherical features. The Co_3O_4 QS-HS was obtained with uniform primary particle size. The Co_3O_4 subunits on the shell are shown in HRTEM (Figure 3.2D) with an interplanar spacing of 0.47 nm. TEM image and reconstructed STEM images visualized by slicing sphere in

Figure 3.2E and F reveal its elaborated interior structure. Meanwhile, EDX element mapping images of Co and O elements (Figure 3.2F) confirms the uniform element distribution in each shell.

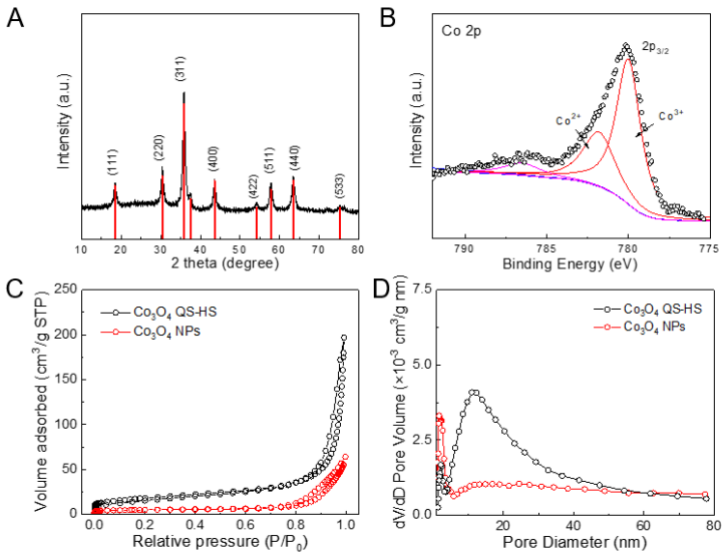

Figure 3.3. Physical characterization of Co_3O_4 QS-HS: (C) XRD pattern, (D, E) N_2 adsorption-desorption isotherms and corresponding pore size distribution (PSD) profiles, (F) High resolution Co 2p XPS spectrum.

The XRD peaks of Co_3O_4 QS-HS in Figure 3.3A can be ascribed to the cubic spinel phase which has the $Fd\bar{3}m$ space group in consistent with previous reports.[116, 117] The Co 2p XPS spectrum of Co_3O_4 QS-HS in Figure 3.3B exhibits two peaks at 780 eV and 795.6 eV, which can be associated with Co $2p_{3/2}$ and Co $2p_{1/2}$.[118] The satellite peaks confirmed the existence of Co^{2+} and Co^{3+} species at the surface.[119] Besides, the perceived Co_3O_4 QS-HS possess a high BET surface area of 69.5 $m^2 g^{-1}$ and moderate porosity (Figure 3.3C and D). The high surface area and abundant mesopores built into the microstructures are beneficial to sufficient electrochemical redox and fast ion diffusion. To demonstrate the generality of

our strategy, we successfully prepared other quadruple-shelled TMOs with tunable composition. Figure 3.4 shows the morphology and interior architecture of $(Ni, Co, Mn)_3O_4$ QS-HS. SEM and TEM images confirm that these types of QS-HS possess similar quadruple-shelled structure morphology and size uniformity. EDX element mapping images of Ni, Co, Mn, O and mixed elements indicates the uniform element distribution in each shell.

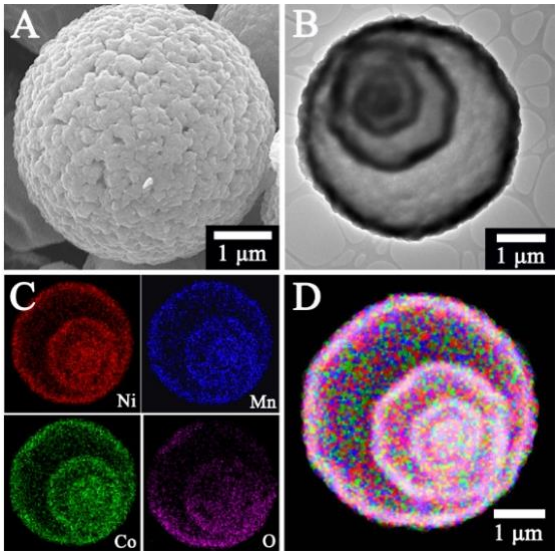

Figure 3.4. (A) SEM image and (B) TEM image of single $(Ni, Co, Mn)_3O_4$ QS-HS. (C) EDX element mappings and (D) mixed element distribution of Ni, Co, Mn and O.

3.4 Structure evolution of multishelled hollow microsphere

To reveal the multishelled structure evolution, the shell formation process of QS-HS was investigated. The FTIR spectra of MAPs precursor in Figure 3.5A shows characteristic adsorption peaks at 1695 cm^{-1} and 1576 cm^{-1}, contributed by COO^- and C=C group. During the annealing process, the microspheres began to shrink near 300°C and their surface were transformed into a metal oxide shell which was induced by the large temperature gradient along the radical direction.[120, 121] In this progress, two forces, contraction force and

adhesion force, are acting simultaneously on the shell interfaces in opposing directions. The contraction force, which causes the inward shrinkage of inner sphere, is induced by the considerable weight loss during the oxidative degradation.[122] On the contrary, the adhesion force hinders the inward contraction of the core from the relatively rigid shell.[100, 123] SEM and STEM images (Figure 3.6A and B) show the separation of the microspheres and the formation of the porous surface. The X-ray diffraction (XRD) peak in Figure 3.6C indicated its crystallization. Furthermore, the inner carbon sphere decomposes with increasing temperature, which is accelerated by TMOs catalytic combustion process,[122] and result in a drastic weight loss above 320°C, as verified by TGA analysis. At around 400°C, the morphology of the outer shell did not change while inner shell has formed, as confirmed by SEM and STEM image (Figure 3.6D and E).

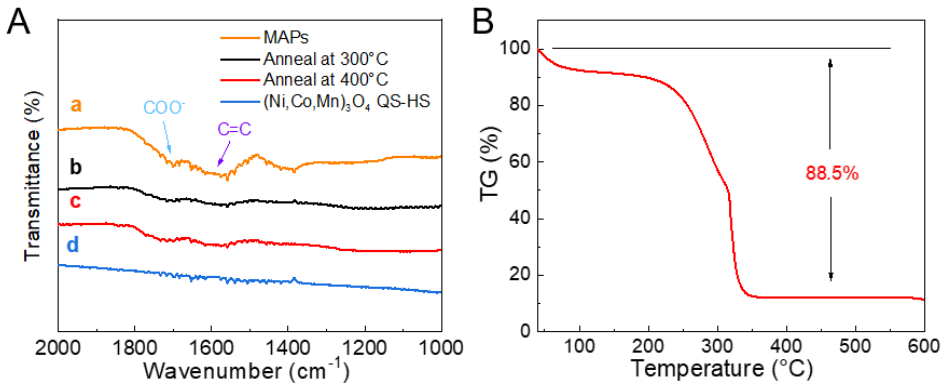

Figure 3.5. Physical characterization of MAPs: (A) FTIR spectra, (B) TGA analysis.

The increase of XRD diffraction peak intensity revealed the continuing crystallization during the annealing progress (Figure 3.6F). At ~500°C, a unique QS-HS was formed with prolonged annealing. No vibration peaks of C=C and COO- are observed from FTIR spectra, indicating no carbonaceous material remaining after heat treatment.[124]

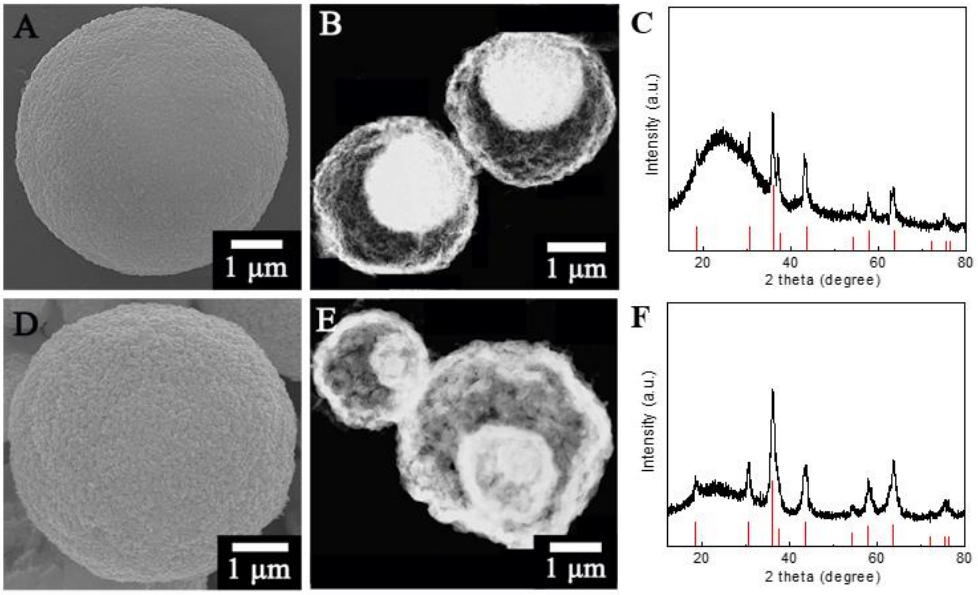

Figure 3.6. SEM images, STEM images and XRD patterns of MAPs annealed at (A, B, C) 300°C for 5 min and (D, E, F) at 400°C for 5 min. (Reference PDF file: 01-080-1534)

Moreover, this tactic is also capable of producing Co_3O_4 multishelled hollow microspheres with tunable shell number by only varying the concentration of metal acetate and glucose source, which is a feasible strategy to control the microsphere with desirable hollow interior. The TEM images in Figure 3.7 demonstrate the successful synthesis of Co_3O_4 double-shelled, triple-shelled and quintuple-shelled hollow microspheres and rigid sphere (named as Co_3O_4 DS-HS, Co_3O_4 TS-HS, Co_3O_4 FS-HS and Co_3O_4 RS, respectively). These evidences indicate that this facile method can also be used to creatively control component and number of shells to design multi-shelled TMOs hollow microspheres to realize enhanced electrochemical performance.

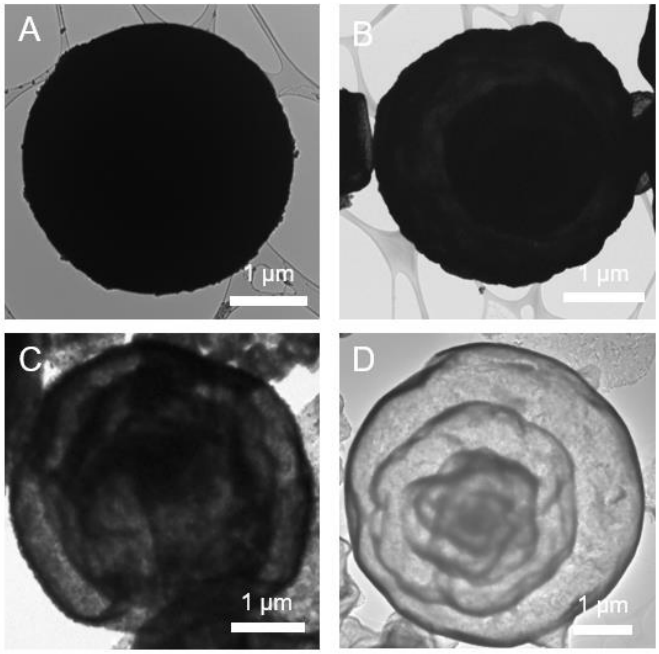

Figure 3.7. TEM images of (A) Co_3O_4 RS, (B) Co_3O_4 DS-HS, (C) Co_3O_4 TS-HS and (D) Co_3O_4 FS-HS.

To further examine the significance of multi-shelled structure design for enhanced sulfur confinement, Co_3O_4 NPs, Co_3O_4 DS-HS, Co_3O_4 TS-HS, Co_3O_4 QS-HS and Co_3O_4 FS-HS sulfur composites were prepared. The mass ratio of sulfur and material are 7:3. Co_3O_4 NPs was synthesized by hydrothemral reaction under 180°C for 6 hrs by using $Co(NO_3)_2$ as precursor, with a ramping rate of 5°C min^{-1}. The SEM image of Co_3O_4 NPs is shown in Figure 3.8, indicating its nanosized feature and severe agglomeration. The sulfur loading content of Co_3O_4 NPs and Co_3O_4 QS-HS were evaluated by TGA analysis (Figure 3.9). Co_3O_4 NPs demonstrates a steep slope at ~225°C, corresponding to sulfur loss from the composites. However, Co_3O_4 QS-HS shows another mass decreasing stage at ~270°C, which is pertained to the sublimation of confined sulfur inside the shell, indicating the sulfur infiltration inside the hollow void. Co_3O_4 QS-HS shows a relatively higher sulfur

content of 69.5% in the composites than that of Co_3O_4 NPs, indicating its stronger sulfur immobilization. The large surface area of Co_3O_4 QS-HS uniforms sulfur distribution on the shell while the multishelled hollow structure offers immense active interfaces to adsorb LiPS and empty inner space to stockpile sulfur species, fulfilling the requirement to be utilized as sulfur immobilizer.

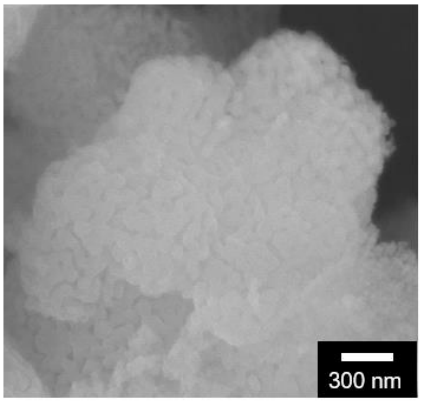

Figure 3.8. SEM image of Co_3O_4 NPs.

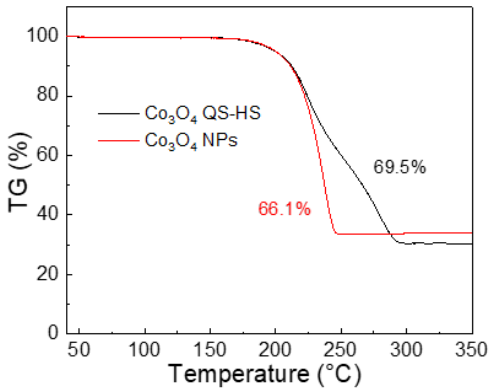

Figure 3.9. TGA analysis of Co_3O_4 QS-HS and Co_3O_4 NPs sulfur composites.

3.5 Electrochemical performance

The Li-S performance was evaluated by GCD cycling with a voltage window of 1.8-2.6 V vs Li/Li^+ to determine the specific capacity values and capacity retentions. Figure 3.10A shows the GCD profiles of Co_3O_4 NPs, Co_3O_4 DS-HS, Co_3O_4 TS-HS, Co_3O_4 QS-HS and Co_3O_4 FS-HS sulfur composites electrode. Clearly, Co_3O_4 QS-HS delivers the highest initial discharge capacity of 1038.8 mAh g^{-1} at 0.2 C (1C = 1670 mA g^{-1}), which outperforms the capacity of Co_3O_4 NPs (812.5 mAh g^{-1}), Co_3O_4 DS-HS (893.7 mAh g^{-1}), Co_3O_4 TS-HS (941.5 mAh g^{-1}) and Co_3O_4 FS-HS (989.8 mAh g^{-1}) indicating the best sulfur utilization of Co_3O_4 QS-HS. With the shell number increasing, the GCD profiles exhibit a gradually reduced potential hysteresis and increased discharge capacity, indicating the improved sulfur kinetics. Figure 3.10B presents the typical cyclic voltammetry (CV) curves of these sulfur composites, which shows good consistency with its voltage profile. For the initial cathodic scan, two sharp peaks can be observed at 2.3 V and 2.05 V, which correspond to the reduction of elemental sulfur into long chain LiPS (Li_2S_x, $4 \leq x \leq 8$) and its further reduction to Li_2S_2 and Li_2S. Two broad anodic peaks can be observed at 2.3 V and 2.45 V, corresponding to the oxidation process from Li_2S to S. EIS spectra and rate performance are further used to estimate the Li-S kinetics of different sulfur electrodes. Figure 3.10C shows representative Nyquist plot, which contain a depressed semicircle in the high to medium frenquency region and a linear Warburg tail in low frequency region. The intercept of the plot with the real axis at high frequency corresponds to the bulk resistance of the electrolyte, while the semi-circle reflects the resistance of the charge transfer process (R_{ct}). The Warburg tail usually represents the ion-diffusion resistance in the electrode materials and structure.[125, 126] Co_3O_4 QS-HS shows the smallest R_{ct}, implying

its best charge transfer kinetics. The rate preformance is also revealed in Figure 3.10D. Co_3O_4 NPs delivers a capacity of 226.7 mAh g^{-1} at 3 C, which only corresponds to ~28% of its initial capacity at 0.2 C, indicating its sluggish sulfur kinetics and poor rate capability. Moreover, the Co_3O_4 DS-HS and Co_3O_4 TS-HS manifest much better rate performance with high electrochemical reversibility, indicating their favored kinetics. The Co_3O_4 QS-HS demonstrates the best rate capability with an admirable discharge capacity of 585.1 mAh g^{-1} at 3 C, confirming its best sulfur electrochemistry. The superior rate performance is mainly originated from the pores on surface of the thin multi-shell, which not only facilitates the electron and ion transfer process but also blocks the migration of LiPS outward the shell. However, a significantly decreased rate performance of sulfur composite can be observed with the shell number further increased. The unsatisfied reaction kinetics is related to the limited void space of Co_3O_4 FS-HS to tolerate the volume effect of sulfur and impeded electron transportation from inner shell to current collector attributed to the elongated transfer pathway. The cycling stability of Co_3O_4 microspheres with different number of shells can also be observed in Figure 3.10E. The Co_3O_4 QS-HS delivers the best cycling performance with the highest capacity of 798.2 mAh g^{-1} and satisfactory capacity retention of 86.3% after 100 cycles, indicating its best cyclic stability attributed to its strengthened LiPS shuttling inhibition. The strong LiPS capability was further examined by evaluating the long-term cycling performance of Co_3O_4 QS-HS. Even under raised current density of 1 C (Figure 3.10F), Co_3O_4 QS-HS still shows much better capacity retention over 300 cycles and higher Coulombic efficiency over 99%, indicating its augment LiPS adsorption capabilities. Therefore, the QS-HS structure design exposes considerable active sites and appropriate void interior, rendering strong adsorption to trap

LiPS. Besides, the multishelled structure further act as barrier to physically block the migration of LiPS, which efficiently confine the LiPS inside shell, leading to much suppressed shuttle effect. Also, this unique hollow structure offers decent structure integrity and large voids between each shell, which are beneficial for the alleviation of the mechanical strain and accommodate volume effect during the lithiation/delithiation process.[127] Overall, owing to these favorable structural features, Co_3O_4 QS-HS electrode achieves improved rate capability and cycle stability for enhanced Li-S performance.

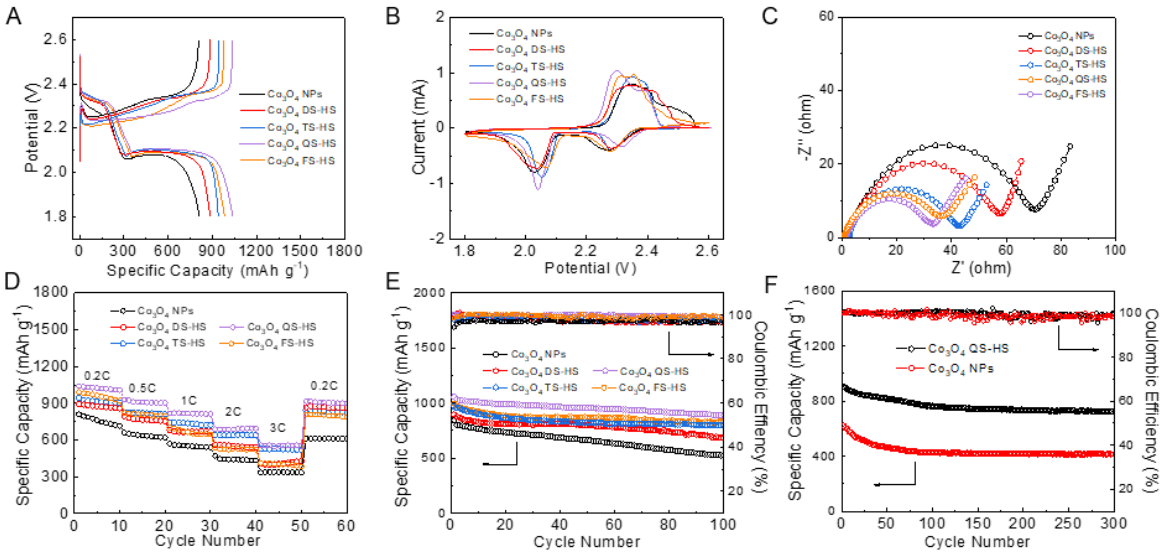

Figure 3.10. Electrochemical performance of Co_3O_4 NPs, Co_3O_4 DS-HS, Co_3O_4 TS-HS, Co_3O_4 QS-HS and Co_3O_4 FS-HS sulfur composites: (A) GCD profiles, (B) CV curves, (C) EIS spectra, (D) rate performance, (E) cycling performance under the current density of 0.2 C. (F) Long term cyclic stability of Co_3O_4 NPs and Co_3O_4 QS-HS under the raised current density of 1 C.

3.6 Conclusion

In summary, we developed a universal and facile strategy to design Co_3O_4 hollow microspheres with tunable shell number and chemical composition as sulfur immbilizer and reveal the advancement of multishelled structure on the electrochemical performance. The as-developed Co_3O_4 QS-HS exhibits high porosity, large surface area and uniform void separation between each shell, which favors electrolyte infiltration, Li^+ transportation and accommodates volume expansion of sulfur during lithiation. The multi-shelled architecture not only offers plenty of active surfaces for uniformed sulfur distribution and favored redox reaction, but also enhances sulfur confinement by strengthening LiPS chemisorption and blocking its diffusion outward the microsphere. A structure-performance relationship was determined by analyzing the Li-S performance of Co_3O_4 with different number of shells. Benefied from the structural superiorities of Co_3O_4 QS-HS, an admirable rate capability and cyclability can be realized.

Chapter 4 Oxygen Defect Engineering of Cobalt Oxide Sulfur Immobilizer for Rapid and Reliable Li-S Performance

4.1 Introduction

In the previous chapter, we have identified that the Co_3O_4 multishelled hollow structure design is capable of offering uniform sulfur distribution and strong chemical interaction of LiPS, thus enhancing sulfur confinement. However, this designed strategy may not meet the requirements for the practical application of Li-S battery, especially under high sulfur loading.[128] The LiPS trapping interaction and electronic conduction provided by supported TMOs NPs are not sufficient. Therefore, it is critical to improve Co_3O_4 sulfur host material to realize decent conductivity, commendable structural stability and fast LiPS conversion kinetics, which plays an essential role in the development of high-performance Li-S batteries.

Cation and anion defects engineering in TMOs have been reported capable of manipulating the electronic structure toward favorable physical and electrochemical properties, so affecting the energetics for electron and ion transport as well as adorability.[129] Among defect engineering, oxygen vacancies (OVs) have been widespread studied in the field of catalysis. First, OVs with abundant localized electrons can act as active centers for the adsorption and activation of adsorbent molecules. Second, the recombination of charge carriers is effectively suppressed due to the strong electron and/or hole trapping ability of surface OVs. As a result, the energy barrier for interfacial charge transfer is significantly reduced. Moreover, OVs can remarkably narrow the bandgap of metal oxides by introducing gap states or altering the valence band and promoting charge transfer from substrates to adsorbates. However, despite its successful applications in other

chemistries, oxygen defect engineering has been rarely investigated for improving the kinetics and sulfur hosting capability of cobalt based TMOs in Li-S battery. Understanding the defect implantation and its substantial effect on the LiPS interactions and electronic/ionic conductivity improvement can guide the sulfur host design to strengthen the sulfur confinement and promote the reaction kinetics.

Herein, we present a universal and straightforward *in-situ* coordinating strategy to synthesize highly defective TMOs double-shelled hollow microspheres (TMOs-HS) which involves the one-pot synthesis of a solid spherical composite precursor and the subsequent thermal treatment to yield the final defect-rich product. The employed defect engineering in this strategy are capable of optimizing the structural and adsorptive properties of TMOs to meet the specific demands of Li-S systems. Herein, disordered spinel $NiCo_2O_{4-x}$ hollow microspheres (NCO-HS) was developed with abundant oxygen vacancies on octahedral sites. The defect engineering endows the as-developed NCO-HS with significantly enhanced electronic conductivity and meanwhile alters the chemical interactions with LiPS towards excellent sulfur immobilization. Moreover, the highly porous and hollow construction shortens the ion transfer distance, homogenizes the sulfur distribution, offers abundant active interfaces, and buffers the volume variation. When employed as sulfur host, these advantageous features enable high sulfur utilization, fast reaction kinetics, and strong sulfur confinement, leading to outstanding battery cyclability with an ultra-low capacity fading rate of 0.045% per cycle over 800 cycles at 0.2 C (1C = 1675 mA g^{-1}) and remarkable rate capability up to 5 C, as well as a high areal capacity of 6.3 mAh cm^{-2} under raised sulfur loading. This strategy offers a synergistic combination of defects engineering and structural design that renders fast and durable sulfur electrochemistry as well as

significantly improved battery performance, holding a great promise in promoting the practical application of Li-S batteries.

4.2 Experimental section

4.2.1 Material Synthesis

To synthesize NCO-HS, 4.93 g $Ni(NO_3)_2 \cdot 6H_2O$, 19.14 g $Co(NO_3)_2 \cdot 6H_2O$ and 10 g glucose were dissolved into 100 mL deionized water under violent stirring. The obtained solution was then sealed into an autoclave for hydrothermal reaction at 180°C for 400 mins with a ramping rate of 5°C min^{-1}. The black precipitate was collected and filtration washed for 3 times each by distilled water and ethanol. The obtained powder precursor was then dried at 70 °C for 12 h. Finally, the NCO-HS was collected by annealing the precursor at 500°C for 1 h under air atmosphere, with a ramping rate of 1°C min^{-1}. The synthesis procedures of Co_3O_4-HS is similar to that of NCO-HS with the exception that only $Co(NO_3)_2 \cdot 6H_2O$ was used as the metal ion source.

4.2.2 Materials Characterizations

Nitrogen adsorption-desorption isotherm analysis (ASAP 2020 micromeritics) was performed to study the pore structures and the surface area was calculated using BET theory. A FEI Quanta FEG 250 SEM and JEOL 2010F TEM were used to collect SEM and TEM images. SHIM was performed using a Zeiss ORION Plus He^+ microscope, operating at an accelerating voltage of 30 kV. TGA was conducted on a TA instrument Q500. UV-vis spectra were collected by Thermal Scientific GENESYS 10S spectrophotometer. The XRD patterns were collected by MiniFlex 600 Rigaku diffractometer. Electron paramagnetic resonance (EPR) spectra was conducted on a Bruker EMX spectrometer at 77 K with a microwave frequency of 9.4 GHz and microwave power of 2 mW. The ELNES

spectra is fitted with least square regression method. The unknown valence state (S) can be got by a linear fitting of two normalized experimental reference spectra with known valence states, using the equation $S(\text{unknown}) = a \cdot S(1) + b \cdot S(2)$. The valence state (V) of unknown species can be determined by $V(\text{unknown}) = \frac{a}{a+b} \cdot V(1) + \frac{b}{a+b} \cdot V(2)$.

4.2.3 Electrode Fabrication

NCO-HS and Co_3O_4-HS sulfur composites were prepared by mixing material and sulfur in a mass ratio of 30:70, followed by a thermal treatment under 155°C for 6 h. The composite powder, Super P and PVDF were mixed in a weight ratio of 7:2:1 and dispersed in NMP. The obtained slurry was coated on Al foil and then dried at 70°C for 12 h. The electrochemical performance test was carried out in CR2032 type coin cell and the cells were assembled with the prepared sulfur composite cathodes, lithium plate anodes, electrolyte and separators in an argon filled glove box. The used electrolyte was 1 M LiTFSI dissolved in a mixed solvent of DOL and DME (1:1, v/v), containing 2 wt% $LiNO_3$. The average areal sulfur loading was ~1 mg cm_2. For symmetric cell, 30 μL above-mentioned electrolyte containing 0.5 mol L^{-1} of Li_2S_6 was used.

4.3 Formation and characterization of NCO-HS

Figure 4.1 illustrates the synthetic process of NCO-HS and the according morphological evolution. NCO-HS with uniform size and morphology was synthesized through hydrothermal method followed by annealing treatment. In this method, glucose and metal nitrates are mixed together for hydrothermal reactions, in which the metal ions (Ni^{2+} and Co^{2+}) are adsorbed *via* an *in-situ* coordinating process during the preliminary carbonization of glucose to form carbonaceous microspherical frameworks (CMF).[69, 71]

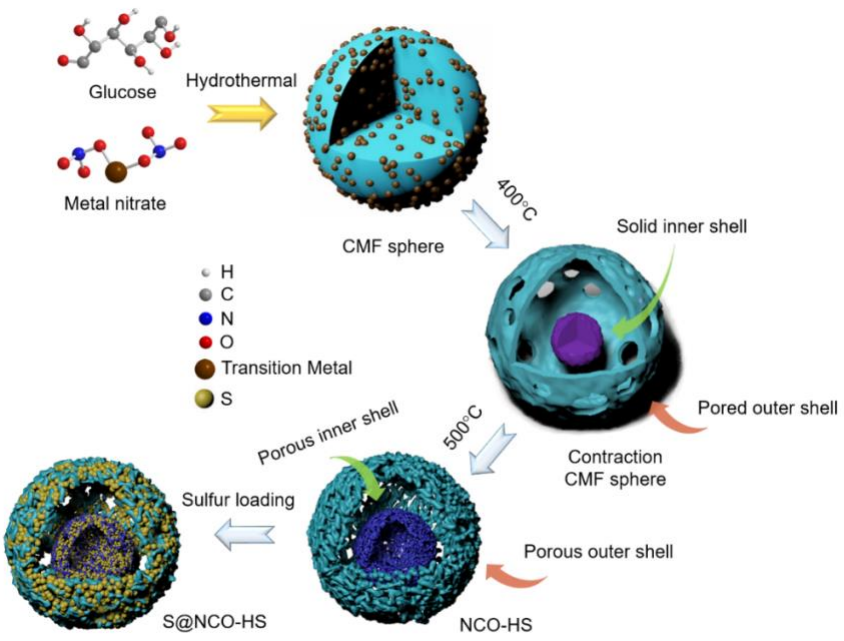

Figure 4.1. Schematic illustration of the morphological evolution of NCO-HS.

Figure 4.2A shows the morphology of CMF with spherical shape and smooth surface. Subsequently, in the calcination process in air, the CMF microspheres began to shrink near 300°C induced by the temperature gradient,[130] which is confirmed by SEM, TEM and XRD (Figure 4.3A-C). When the temperature continues increasing to 400°C, the layer separation occurs inside the solid CMF sphere to form a double-shelled structure, which is attributed to the combined actions of contraction force and adhesion force in opposite directions on the shell.[122] (Figure 4.3D-F**)** Meanwhile, the XRD pattern reveals the crystallization during this annealing stage while the drastic weakening of the carbon peak indicates the decomposition of the carbonaceous components. At a higher temperature of 500°C, the NCO-HS was collected through prolonged annealing (Figure 4.2B, C).[123]

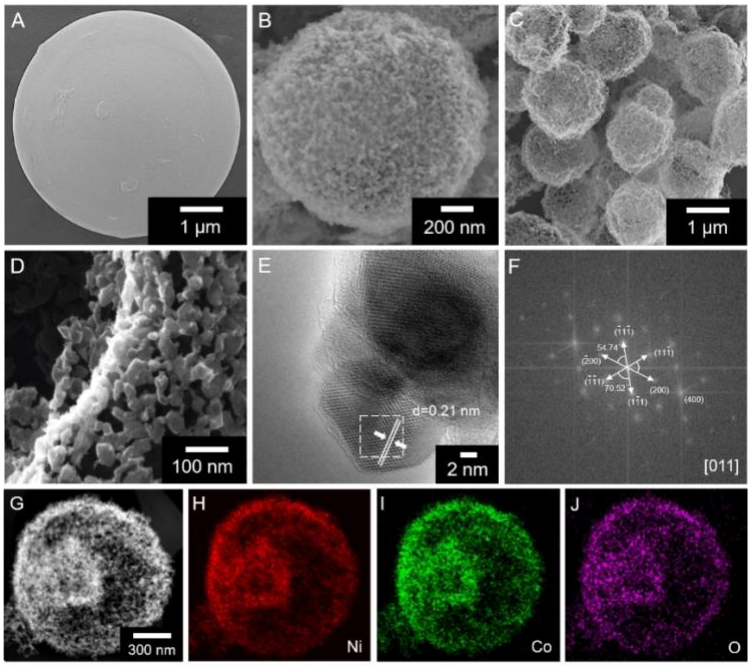

Figure 4.2 SEM images of (A) CMF and (B, C) NCO-HS; (D) SHIM image, (E) HRTEM image and (F) FFT image of NCO-HS; (G) STEM image and (H-J) element distribution mapping of Ni, Co and O for NCO-HS.

The obtained microspheres exhibit good size uniformity and plentiful meso-pores on the shell surface, which is confirmed by scanning helium ion microscopy (SHIM), indicating its appealing electron and ion transportation.[131] Clearly, the highly porous NCO-HS acquires admirable structure integrity without damage when bombarded by He ions (Figure 4.2D). The highly porous NCO-HS provides vast active sites for sulfur reaction and vast channels for ion transfer, while the large inner voids in the hollow structure facilitates sufficient sulfur loading. The STEM images of NCO-HS and EDX element mapping clearly reveal its interior structure and uniform element distribution (Figure 4.2H-J). For comparison, Co_3O_4 double-shelled hollow microspheres (Co_3O_4-HS) was also synthesized, of which the consistent porous and double-shelled hollow structures (Figure 4.4**)**.

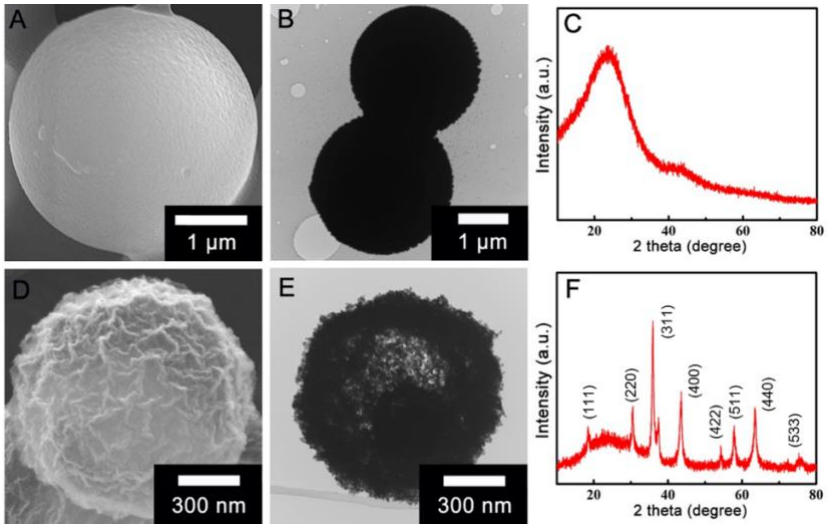

Figure 4.3 SEM image, TEM image and XRD pattern of CMFs (A, B, C) annealed at 300°C for 5 min and (D, E, F) at 400°C for 5 min.

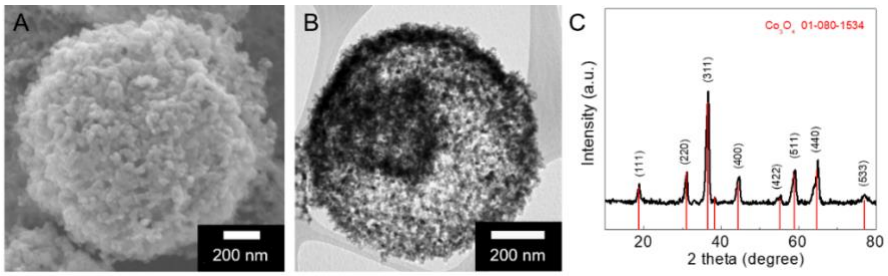

Figure 4.4 (A) SEM image, (B) TEM image and (C) XRD pattern of Co_3O_4-HS.

The in-depth crystalline feature of the obtained NCO-HS was further characterized by HRTEM, which exhibits an interplanar spacing of 0.21 nm corresponding to the (400) crystallographic plane (Figure 4.2E). Meanwhile, the FFT image with periodic arrangement of the lattice fringe selected area (Figure 4.2F) reveals a cubic structure with a crystal axis of [011]. Figure 4.5A shows the XRD result of NCO-HS, confirming its cubic spinel phase with the $Fd\bar{3}m$ space group.[132, 133] The XRD pattern and FFT image in Figure

4.6 of Co_3O_4-HS implies its similar crystal structures with NCO-HS. However, the significantly negatively shifted XRD peaks can be observed for NCO-HS, suggesting an disordered lattice volume resulted from defect engineering.[134]

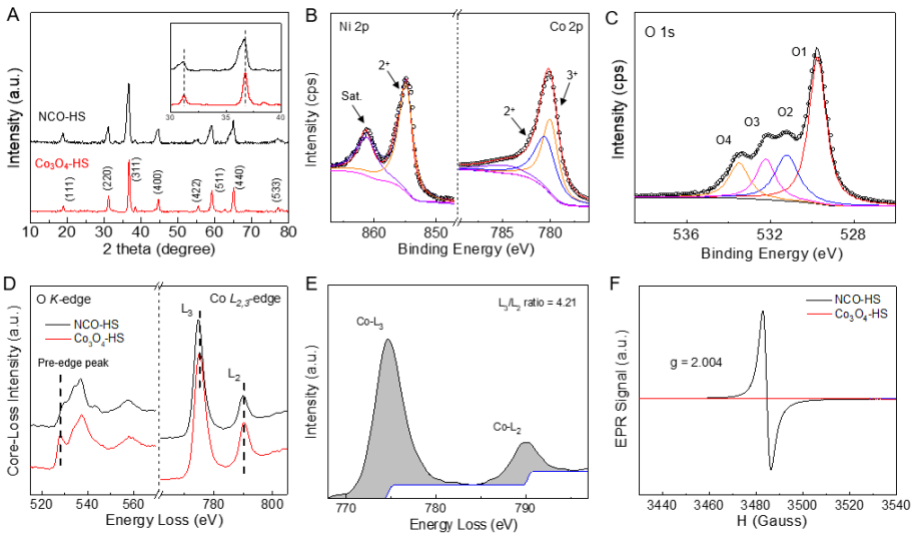

Figure 4.5 (A) XRD patterns of NCO-HS and Co_3O_4-HS (inset: local magnification of the (220) and (311) peaks); the high resolution (B) Ni 2p and Co 2p and (C) O 1s XPS spectra of NCO-HS; (D) ELNES spectra of the O K-edge and Co $L_{2,3}$-edges and (E) L_3/L_2 ratio of Co, (F) EPR pattern of NCO-HS and CO_3O_4-HS.

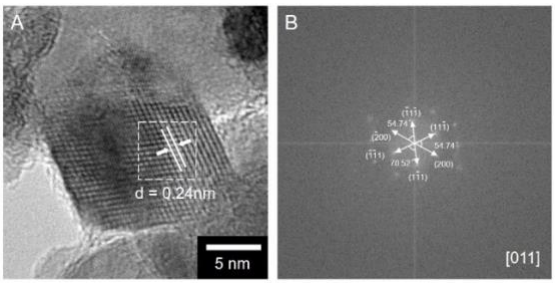

Figure 4.6 (A) HRTEM image and (B) Fast Fourier Transform image of Co_3O_4-HS.

The as-developed NCO-HS was studied by N_2 adsorption-desorption measurement (Figure 4.7). The NCO-HS exhibits a higher BET surface area of 127.6 m_2 g^{-1} and

hierarchical PSD than Co_3O_4-NPs (Figure 3.3). The high surface area built into the microstructure are beneficial for uniform sulfur distribution, efficient LiPS confinement and fast ion/electron transfer. Beyond that, the doping strategy by substituting Ni into the spinel Co_3O_4 lattice is expected to introduce defects, which is promising to increase the electrical conductivity and intensify the LiPS chemical interactions.[135]

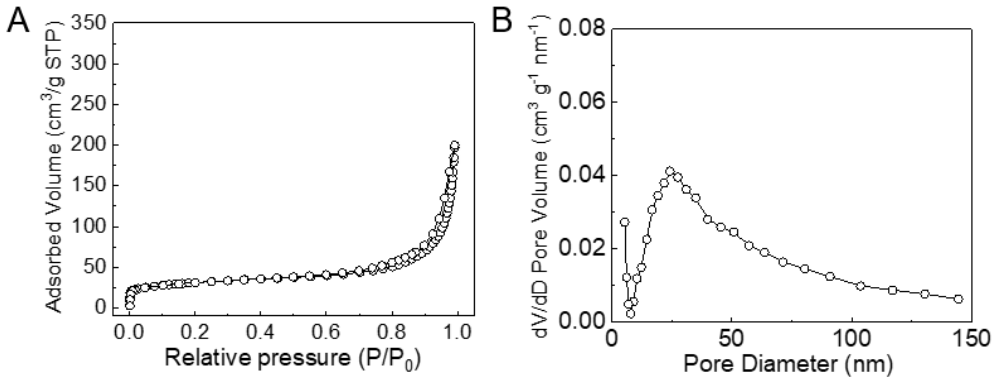

Figure 4.7 (A) N_2 adsorption-desorption isotherms and (B) PSD of NCO-HS.

The surface chemistry of NCO-HS was investigated by XPS analysis. The peaks located at 854.7 eV in Ni $2p_{3/2}$ spectrum (Figure 4.5B) confirms the existence of Ni^{2+} species in NCO-HS.[55, 136] The two sub peaks in Co $2p_{3/2}$ spectrum located at 780 eV and 780.7 eV can be assigned to Co^{2+} and Co^{3+}, which implies the non-integral valence of cobalt in NCO-HS.[137] Figure 4.5C displays the O 1s spectrum of NCO-HS, which can be fitted into four sub peaks (O1, O2, O3, and O4). The strongest O1 peak is located at 529.8 eV, corresponding to metal-oxygen bonds.[138] A shoulder O2 peak can be observed at 531.2 eV, indicating the hydroxylated surface of NCO-HS, which is favorable to attracting LiPS.[139] The O3 peak at 532.2 eV can be considered to be defects with a low oxygen coordination.[140] The O4 peak located at 533.5 eV is contributed by adsorbed moisture on the surface of NCO-HS.[141, 142] The defective structure of NCO-HS was further probed by electron energy

loss near-edge structure spectroscopy (ELNES) and electron paramagnetic response spectroscopy (EPR). Figure 4.5D shows the core-loss O K-edge and Co $L_{2,3}$-edges near-edge spectra. The pre-edge peak located at 528 eV in O K-edge spectra is attributed to the hybridization of the unoccupied O 2p orbital with Co 3d orbitals.[143] The less prominent pre-edge peak of NCO-HS confirming the existence of oxygen vacancies.[144] In Co $L_{2,3}$-edges spectra, the intense L_3 edge can be assigned to Co $2p_{3/2}$ and the L_2 edge is attributed to Co $2p_{1/2}$ orbital. A 0.5 eV shift is observed from the Co L_3 peak of NCO-HS while the Co L_2 peak remains unchanged, indicating the valence state reduction of octahedral Co^{3+} species.[145] This shift is in agreement with the trend observed from Co $2p_{3/2}$ XPS spectra (Figure 4.8A, B), which exhibits a negative shift of 0.5 eV binding energy (BE) of Co^{3+} peak (780.6 eV) in NCO-HS.

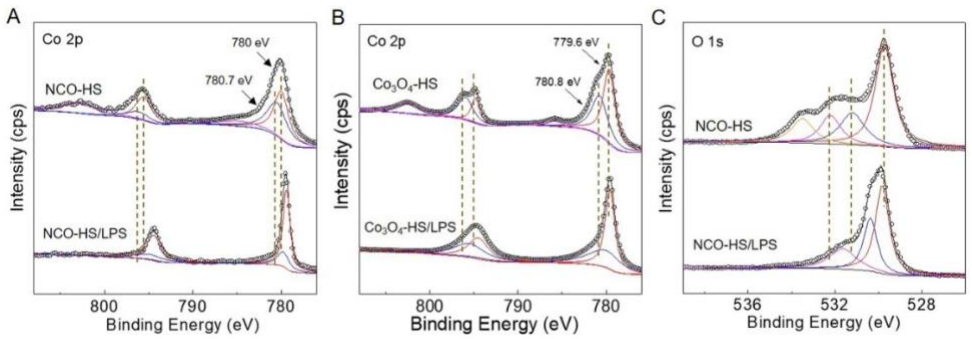

Figure 4.8 Co 2p XPS spectra of (A) NCO-HS and NCO-HS/LiPS, (B) Co_3O_4-HS and Co_3O_4-HS/LiPS, and (C) O 1s XPS spectra of NCO-HS and NCO-HS/LiPS.

The processed ELNES spectrum reveals a L_3/L_2 intensity ratio of 4.21, implying the valence state around $Co^{2.2+}$ (Figure 4.5E) .[146] Moreover, the normalized Co $L_{2,3}$ ELNES spectrum regression fitting suggests a composition of 20.5% of Co_3O_4 (with $Co^{2.67+}$) and 79.5% of CoO (with Co^{2+}), indicating the cobalt valence state in NCO is $Co^{2.13+}$. This fitting

result also indicates the formation of disordered octahedral coordination around Co sites in NCO-HS. The EPR pattern present a distinctive EPR signal with a g value of 2.004, suggesting a higher concentration of oxygen vacancies in NCO-HS in drastic contrast to Co_3O_4-HS (Figure 4.5F**)**.[147] All these results consistently verify the highly defective nature of the as-developed NCO-HS. The defect engineering is expected to create new defect states such as dangling bonds and oxygen vacancies located in the band gap of Co_3O_4 so as to lower the formation energy of electron holes in Co_3O_4 and give rise to a substantially enhanced electrical conductivity.[148] To examine the boosted electrical conductivity through defect-engineering in the proposed strategy, the conductivity of the prepared NCO-HS and Co_3O_4-HS were measured. The as-developed NCO-HS exhibits a significantly higher conductivity of 0.52 S cm^{-1} and such electrical conductivity enhancement of NCO-HS is expected to offer an improved electron transfer for fast sulfur electrochemistry.

4.4 Enhanced LiPS adsorption by oxygen defect engineering

In view of its highly defective and polar nature, NCO-HS could also facilitate the adsorption of LiPS for improved sulfur confinement in Li-S batteries.[149, 150] To testify the LiPS adsorption abilities, NCO-HS, Co_3O_4-HS and Co_3O_4-NPs were immersed into Li_2S_6 solution (Figure 4.9A). The pristine Li_2S_6 solution shows an orange color. After adsorption, the Li_2S_6 solution adsorbed by NCO-HS manifests a much lighter color than the others, which intuitively illustrates its strongest adsorption to LiPS. UV-vis measurements were performed to further investigate the Li_2S_6 adsorption capabilities. The UV-vis spectrum of the pristine Li_2S_6 shows peaks at 265 nm and 415 nm, which are assigned to S_6^{2-} and S_4^{2-}, respectively.[151] The most reducing peaks intensity of NCO-HS indicates its strongest PS adsorption, which is consistent with the optical observation (Figure 4.9B). XPS analysis

was performed to verify these chemical interactions. Both the Co $2p_{1/2}$ and Co $2p_{3/2}$ peaks of NCO-HS/LiPS shift significantly to lower BE ranges (Figure 4.8A). Especially, the octahedral coordinated Co peak undergoes a much large shift than that for Co_3O_4-HS/LiPS (Figure 4.8B). These results indicate that the introduction of defect engineering in NCO-HS improves the chemical interaction between Co and LiPS.[11] Besides, the major peak of the M-O bond in NCO-HS/LiPS shifts to a higher BE range, corresponding to a reduction of electron cloud density in O, suggesting the formation of "lithium bond"-like interactions (Figure 4.8C).[113] The other peaks in the NCO-HS/LiPS shift towards lower BE, which implies the coordination between the oxygen defects and the sulfur in LiPS, corresponding to the PS adsorption on oxygen vacancies.[25, 152]

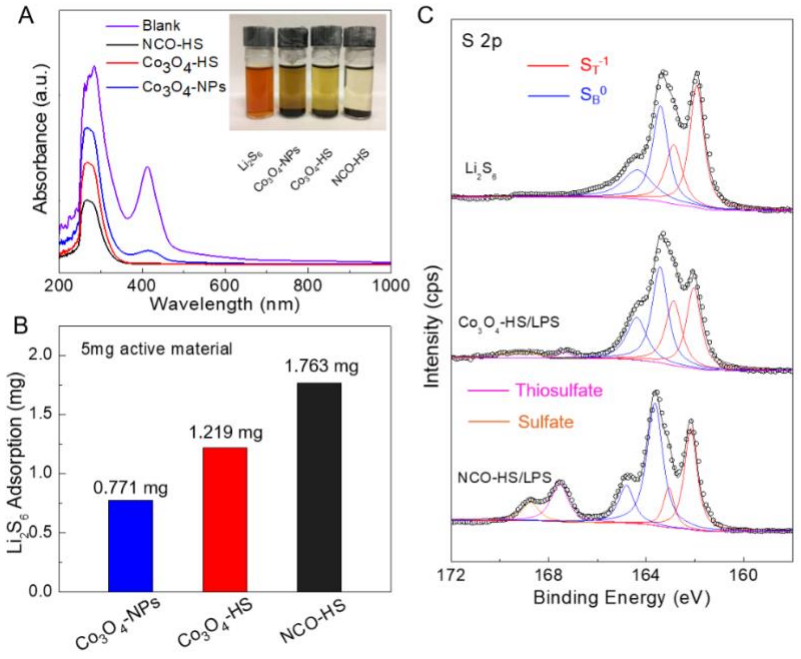

Figure 4.9 (A) UV-vis spectra and optical images of LiPS solutions adsorbed by Co_3O_4-NPs, Co_3O_4-HS and NCO-HS; (B) PS adsorption capacities of different adsorbers. (C) XPS spectra of S 2p for pristine Li_2S_6, Co_3O_4-HS/LiPS and NCO-HS/LiPS.

Further verification on the chemical interactions can be gained through the S 2p XPS spectra (Figure 4.9C). The large shift of S_{T-1} and S_{B0} peaks in the NCO-HS/LiPS spectra can be observed after adsorbed Li_2S_6, indicating the reduction of electron cloud density in sulfur atoms and further confirming the strong chemical interactions between NCO-HS and LiPS.[4] This is attributed to the stronger binding ability and the increased adsorption sites induced by the massive oxygen vacancies in NCO-HS.[153] A pair of new peaks emerges in NCO-HS/LiPS spectra, which refers to the formation of polythionate complex and further manifests the chemical bondage between defective sites of NCO-HS and LiPS.[154, 155] All these variations in XPS spectra evidentially support the strong chemical interactions between NCO-HS and sulfur species.

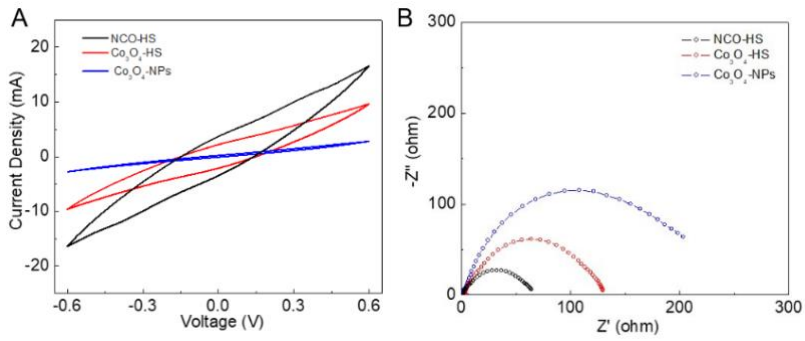

Figure 4.10 (A) Polarization curves and (B) EIS spectra of Li_2S_6-Li_2S_6 symmetrical cells of NCO-HS, Co_3O_4-HS and Co_3O_4-NPs.

Symmetrical cells were further employed to investigate the interfacial interaction of PS (Figure 4.10).[156] The CV and EIS results of NCO-HS exhibit the highest redox current density and smallest electrochemical resistance among the different electrodes. These results further confirm the significantly improved kinetics of PS redox reactions on NCO-HS matrix, which is attributed to its superior conductivity and stronger LiPS adsorption.[157]

Electrochemical evaluations were further conducted to verify the Li-S performance. TMOs-sulfur composites were prepared through the melt-impregnation method with a sulfur content of 70 wt.% in the composites,[158] which is confirmed by TGA analysis in Figure 4.11. The SEM and TEM image in Figure 4.12 indicate a uniform distribution of sulfur. After sulfur loading, the NCO-HS sphere well maintains its double-shelled hollow structure without collapses.

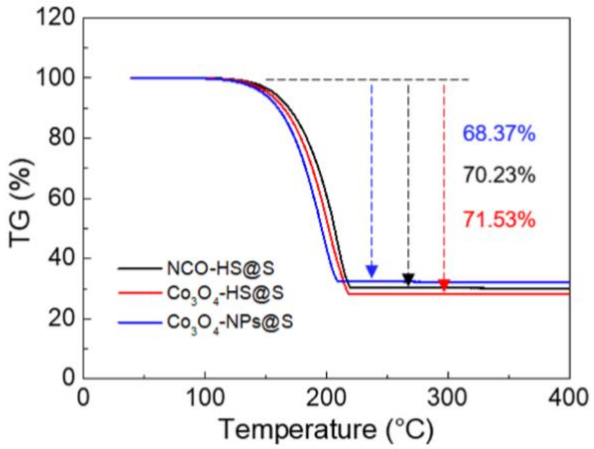

Figure 4.11 TGA analyzation of S@NCO-HS, S@Co_3O_4-HS and S@Co_3O_4-NPs.

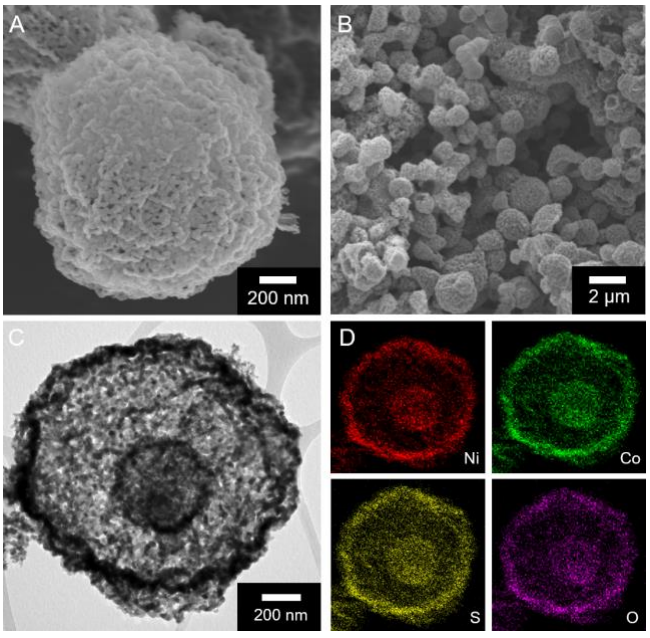

Figure 4.12 (A-C) SEM and TEM images of NCO-HS and (D) EDX element distribution.

4.5 Electrochemical performance improvement by defect engineering

Electrochemical evaluations were performed to verify the advantageous effects of NCO-HS serving as sulfur immobilizer for Li-S batteries. Figure 4.13A shows the GCD profiles with two distinguished plateaus curves for NCO-HS and Co_3O_4-HS sulfur composites electrodes. The high-potential discharge plateau at around 2.3 V (vs. Li^+/Li) is attributed to the electro-reduction of elemental sulfur into soluble long-chain LiPS (Li_2S_8 and Li_2S_6), while the long discharge plateau at around 2.1 V corresponds to the further reduction of the LiPS to form insoluble Li_2S_2 and Li_2S. The CV results in Figure 4.13B are in good agreement with the charge-discharge profiles by showing two major reduction peaks at 2.3 V and 2.05 V, and two major oxidation peaks at 2.35 V and 2.4 V. Notably, NCO-HS displays much smaller potential hysteresis in both voltage profile and CV curve compared to the other electrodes, indicating its smaller electrochemical polarization and improved reaction kinetics. The rate performances in Figure 4.13C shows that the NCO-HS exhibits the best rate capability with a high discharge capacity of 855 mAh g^{-1} at 5 C as well as a highly reversible capacity of 1103.5 mAh g^{-1} when the current is returned to 0.2 C. These results manifest that the defect engineering on NCO-HS can provide favorable conduction properties for the sulfur electrode to achieve fast reaction kinetics. Figure 4.13D shows the cycling performances of different electrodes at 0.2 C. The NCO-HS exhibits the best cycling performance with a high capacity retention of 1143.8 mAh g^{-1} after 100 cycles. The superior cyclability of NCO-HS is attributed to the combination of strong physical and chemical adsorptions of LiPS benefited from the structural superiorities of NCO-HS. The

uniform coating of sulfur species on the NCO-HS surface after 100 cycles indicates the strong sulfur immobilization and inhibited shuttle effect. Attributed to the uniform sulfur

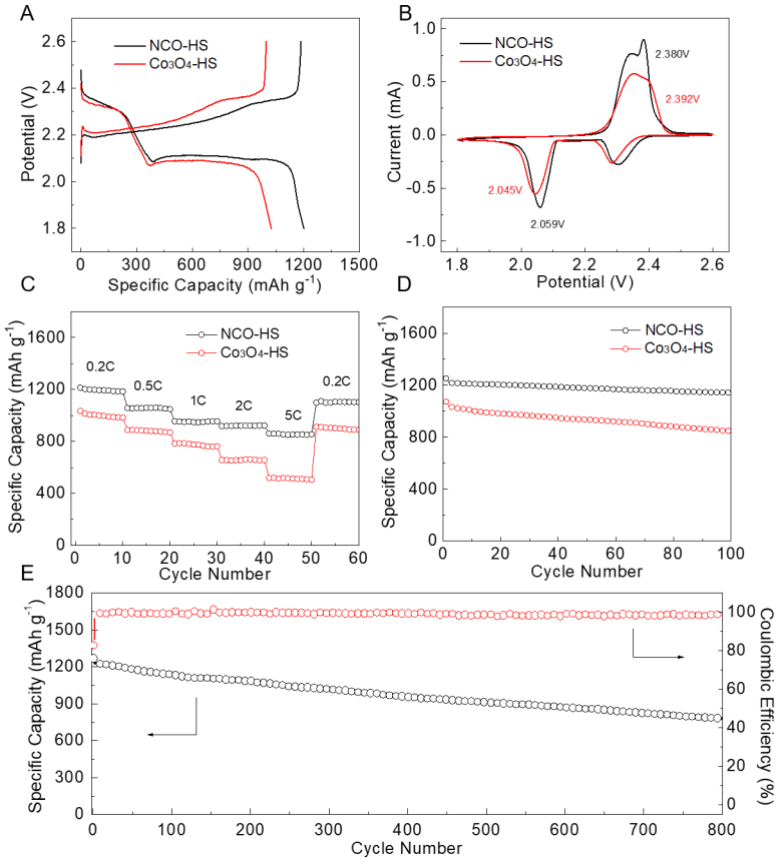

Figure 4.13 (A) GCD profiles at 0.2 C, (B) CV curves at scan rate of 0.1 mV s^{-1}, (C) rate performances, and (D) cycling performances at 0.2 C of NCO-HS and Co_3O_4-HS sulfur composites; (E) cycling performance of NCO-HS sulfur composites.

distribution, fast reaction kinetics, and excellent sulfur immobilization, NCO-HS achieves an outstanding cyclability with a low capacity fading rate of 0.045% per cycle and a highly reversible capacity of 781.8 mAh g^{-1} after 800 cycles at 0.2C (Figure 4.13E). Conductivity measurements and EIS tests were also performed to verify the improved sulfur electro-

redox. Notably, NCO-HS still possess the highest conductivity of 0.29 S cm^{-1} after sulfur loading, indicating the best electron transfer within the bulk composite (Figure 4.14). Moreover, it holds the smallest interfacial charge-transfer resistance and Warburg resistance, which further illustrates its best charge and mass transfer properties among these composites. These results evidence the great promotion of conduction properties and the reaction kinetics contributed by the unique structural features of NCO-HS.

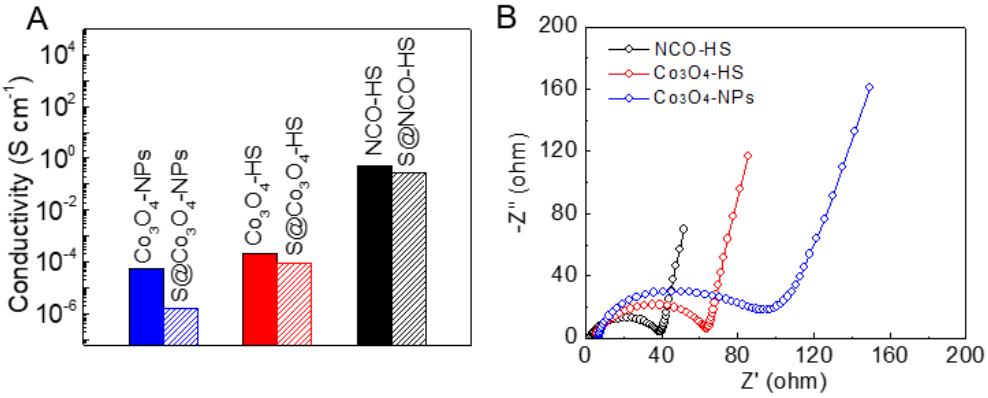

Figure 4.14 (A) electrical conductivities of NCO-HS, Co_3O_4-HS, Co_3O_4-NPs, and their sulfur composites; (B) EIS spectra of NCO-HS, Co_3O_4-HS and Co_3O_4-NPs electrodes.

The practical application of Li-S batteries requires a raised sulfur loading on electrode to gain higher energy density. Figure 4.15A shows GCD curves of NCO-HS electrode at different current densities. Clearly, the distinguished two-plateau charge-discharge curves can still be obtained at a relatively high rate of 2 C, indicating its low polarization and appealing reaction kinetics even under high sulfur loading. Nevertheless, Figure 4.15B manifests the admirable rate capability of the high-loading NCO-HS electrode by showing a highly reversible areal capacity of 3.8 mAh cm^{-2} at 2 C and a decent capacity of 5.4 mAh cm^{-2} after switching the current back to 0.2 C. Furthermore, the stable long-term operation

also indicates the remarkable cyclability of the NCO-HS under high sulfur loading (Figure 4.15C) with a constantly high areal capacity over 5 mAh cm^{-2}, which is competitive with commercial Li-ion batteries.[159] The uniform sulfur distribution and the excellent conduction properties in the highly porous and defective NCO-HS ensures high sulfur utilization and fast reaction kinetics, while the strong physical and chemical sulfur immobilizations further suppress the dissolution and shuttle behaviors of LiPS, leading to significantly prolonged cycling lifespan.

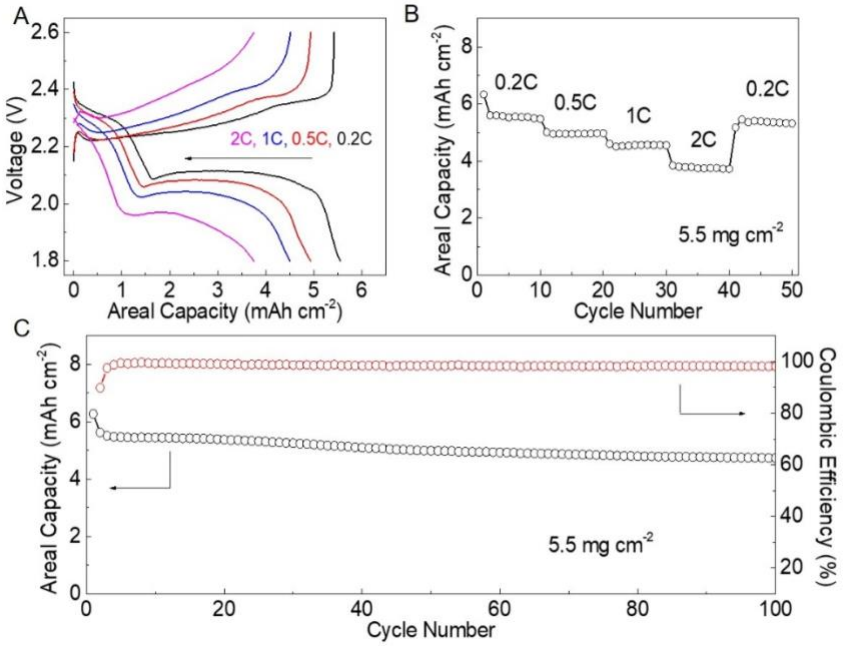

Figure 4.15 (A) GCD profiles at different current densities, (B) rate performance of NCO-HS with a sulfur loading of 5.5 mg cm^{-2}, (C) cycling performance of NCO-HS at 0.2 C.

4.6 Conclusion

In summary, we have developed a facile and universal *in-situ* coordinating method to synthesize TMO double-shelled hollow microspheres with cation and anion defects. The obtained NCO-HS displays a unique double-shelled hollow structure and hierarchical

porosity, which favors uniform sulfur distribution, fast ion transfer, and potent physical sulfur confinement. Meanwhile, the defective spinel NCO-HS consisting abundant Ni^{2+} substitution within Co_3O_4-HS matrix and oxygen vacancies on octahedral sites, was endowed with significantly enhanced electrical conductivity and strong chemical interactions with sulfur species, contributing to fast sulfur electro-redox and excellent sulfur immobilization. Benefited from these advantages, NCO-HS served as a multifunctional sulfur host to achieve fast and durable sulfur electrochemistry with a minimal capacity fading rate of 0.045% per cycle over 800 cycles at 0.2 C, superior rate capability up to 5 C, and high areal capacity of 6.3 mAh cm^{-2} under raised sulfur loading. This implementation of defect engineering to design a highly conductive and adsorptive sulfur host offers an instructive attempt for material engineering towards superior Li-S performance, which is also promising to be extended to other energy fields such as lithium-ion batteries, supercapacitors, and electro-catalysis.

Chapter 5 Sulfur Defect engineering of Cobalt Sulfide Sulfur Immobilizer for Rapid and Durable Li-S Performance

5.1 Introduction

In previous chapter, Co based transitional metal oxides (TMOs) were developed as sulfur immobilizers in Li-S batteries. Due to the strong chemical interaction and promoted LiPS adsorption on polar oxides surface, the introduction of TMOs can migrate the shuttle effect of LiPS.[160] Recently, Co based transitional metal chalcogenides (TMCs), especially transition metal sulfides also attract much attention owing to its much improved LiPS conversion kinetics. Meanwhile, the thermal stability and electronic conductivity of cobalt sulfides are superior to most other metal sulfides.[43, 161] Therefore, a selection of TMCs based sulfur host material with decent ion/electron conduction, proper porosity design with enhanced structural stability and abundant LiPS trapping/catalytic active sites is essential to improve Li-S performance.

Anion defect engineering in TMCs is highly sought after in electrocatalysis area. Recently, introducing sulfur vacancies (SV) in MoS_2 and other related materials are widely investigated. For example, Zhang et al. reported the rational design of 1T/2H MoS_2 can create positive sulfur vacancies on its interface, which significantly improved the LiPS adsorption.[113] Understanding the role of SV in Li-S battery and investigating the LiPS adsorption and conversion process on the defective sites is able to guide the sulfur immobilizer design toward fast Li-S electrochemistry. Considering the similar crystalline structure between Co_3O_4 and Co_9S_8 phases, it is reasonable to anticipate that cobalt sulfides could have similar vacancies formation sites comparing with cobalt oxides and produce vast sulfur vacancies in their structure, which play key roles in tuning the structure

distortion to realize enhanced Li-S kinetics.[148] However, such S-vacancies are unstable and the activities are very sensitive to the vacancy concentration. A strategy to stabilize these abundant active sites is thus highly desirable.

Herein, we developed a synergistic strategy combining the design of three-dimensional ordered mesoporous (3DOM) structure with facile surface engineering technique to afford sulfur immobilizer with superior Li-S electrochemistry. This strategy is demonstrated by the successful fabrication of 3DOM N-Co_9S_{8-x} composite through a hard template method. Compared with NCO-HS, the 3DOM N-Co_9S_{8-x} exhibits similar surface area as well as approximate size of particle and its subunit, making it possible to compare the performance enhancement of cobalt based TMCs with different type of anion defects. The 3DOM structure offers abundant surface area and large porosity to host active sulfur species, reserve electrolyte and accommodate volume expansion during sulfur lithiation. Meanwhile, the surface chemical property that contributed to the enhanced LiPS adsorption and rapid conversion kinetics was thoroughly investigated by the X-ray absorption spectroscopy (XAS) technique and DFT theoretical calculations. It was found that the defect engineering, through a facile ammonia treatment, introduces N substitution on the surface of Co_9S_8, tuning part of CoS_4 tetrahedron into CoS_6 octahedron, leading to the formation of S vacancies on the octahedral Co sites. These S vacancies, which further act as active sites, strengthen LiPS adsorptive and catalytic properties, rendering expedite redox reactions. Benefited from these advantages, the 3DOM N-Co_9S_{8-x} sulfur cathode delivers superior cyclability with a low capacity fading rate of 0.04% per cycle over 500 cycles at 1 C, an excellent rate capability up to 5 C and high areal capacity over 5.9 mAh

cm^{-2} under raised sulfur loading and decreased electrolyte/sulfur (E/S) ratio, offering great promises to be used for practically viable Li-S batteries.

5.2 Experimental Section

5.2.1 Material synthesis

The 3DOM Co_9S_8 composites were prepared using polystyrene (PS) spheres as template. The PS spheres have an average diameter of ~200 nm and were synthesized through emulsion polymerization using styrene, polyvinylpyrrolidone (PVP), potassium persulfate, and deionized water. Details on the preparation of PS spheres can be found in the literature.[162] For the development of 3DOM N-Co_9S_{8-x}, 1.50 g cobalt sulfate [$Co(SO_4)_2 \cdot 4 H_2O$] was dissolved in 10 mL methanol and then add 0.5 mL hydrochloric acid (HCl) aqueous solution. The as-obtained precursor solution was added drop-wisely to the PS template (1mL precursor: 0.2 g PS) under vacuum filtration. The infiltrated PS template was dried overnight at room temperature and transferred to furnace and calcination under NH_3 atmosphere at 500°C for 5 min.

5.2.2 Physical characterization

The morphology of the 3DOM samples were characterized by SEM (LEO FESEM 1530) and TEM (FEI Titan 80-300 LB). The crystal structures were investigated by XRD (Bruker AXS D8). The surface chemical composition of the samples was studied by XPS. The surface area and porosity were examined by BET analysis according to the nitrogen adsorption-desorption isotherms. The XANES measurements were performed at Canadian Light Source Inc, Canada, using the SXRMB beamline. All XANES data were processed using Athena program. TGA was conducted on a Q500 TGA instrument. EPR spectra were

obtained on a Bruker EMX spectrometer at 77 K with a microwave frequency of 9.4 GHz and microwave power of 2 mW.

5.2.3 Electrochemical measurements

The 3DOM N-Co_9S_{8-x}/S cathode composite was prepared *via* melting-diffusion method. First, the 3DOM N-Co_9S_{8-x} and S were mixed with a mass ratio of 30:70. Then, the as-obtained black powder was sealed in a glass vial and heat at 155°C for 6 hours. The sulfur composite, Super P and PVDF was well mixed with a mass ratio of 7:2:1 in NMP to form the slurry. The composite electrodes were fabricated by coating the slurry on Al foil with a mass loading of ~1 mg cm^{-2}. Li foil was used as counter and reference electrode and 2032 type coin cell were used for battery assembling. The electrolyte was prepared by well dissolved 1.0 M LiTFSI with 2 wt% $LiNO_3$ in the mixed DOL/DME solvent. CV and EIS were recorded on electrochemical workstation (Princeton, Versa STAT 4).

5.2.4 Symmetric cell assembling

The symmetric cell electrode was fabricated by mixing active material, super P and PVDF with a mass ratio of 8:1:1 and well dispersed in NMP solvent. The slurry was coated on carbon paper with a mass loading of ~1 mg cm^{-2}. Then the electrodes were punched with a diameter of 12 mm. Two identical electrodes were used as the working and the counter electrodes and Li_2S_6 electrolyte (30 μL containing 2.5 mol L^{-1} [S] and 1 mol L^{-1} LiTFSI in DOL/DME solution) was used as cell electrolyte. The CV measurement of the symmetric cell was conducted at a scan rate of 10 mV s^{-1} with a voltage window between -0.8 and 0.8V. The EIS was performed in a frequency range from 0.1 to 10^5 Hz.

5.2.5 Li_2S Nucleation characterizations

The Li_2S Nucleation test cell was assembled by using the identical electrode as working electrode and Li foil as counter electrode. 20 uL Li_2S_8 electrolyte (Li_2S_8 solution containing 2.0 mol L^{-1} [S] and 1 mol L^{-1} LiTFSI in tetraglyme was used as catholyte and 20 μL control electrolyte without Li_2S_8 was used as anolyte). The assembled cells were first discharged galvanostatically at 0.112 mA to 2.06 V and then discharged potentiostatically at 2.05 V for Li_2S nucleation and growth. The potentiostatic discharge was terminated when the current was below 0.1 mA.

5.2.6 Density functional theory calculations

The Perdew-Burke-Ernzerhof (PBE) function was used for the exchange and correlation energy terms. The U value of Co was set to 2 eV and a plane-wave cutoff of 400 eV was used. Li_2S_2, Li_2S_4 and Li_2S_6 were selected as typical LiPS and studied their absorption on Co_9S_8 (311) and N-Co_9S_{8-x} (311). The N-Co_9S_{8-x} model was constructed according to chemical composition determined by XPS analysis. Under the specific composition, local stable slab configurations were given by optimizing extensive slabs with different N and S distributions. All the slabs have a vacuum height of 15 Å. The cell parameter of (2×2) super cell was constructed. The bottom two atomic layers were fixed whereas the remaining layers and the LiPS adsorbates were allowed to relax. The k-space was sampled using a 2×2×1 Monkhorst-Pack grid. The BE was calculated as $BE = E_{total} - E_{LiPS} - E_{surf}$, where E_{total} is the total energy of the absorbed system, E_{LiPS} is the energy of the optimized LiPS species in vacuum and E_{surf} is the energy of the optimized bare surface.

5.3 Morphological analyzation of 3DOM N-Co_9S_{8-x}

Figure 5.1a shows the synthetic process of 3DOM N-Co_9S_{8-x}, which illustrated the synergy of architecture design and defect engineering to construct a multifunctional substrate for enhanced Li-S electrochemistry. The 3DOM structure was constructed by using PS spheres as template obtained by the self-assembly method.[163] During the pyrolysis process under Ar atmosphere, the soaked metal sulfate precursor in the void of PS spheres was converted into Co_9S_8, whereas the PS template will decompose, forming large interconnected pore structure. The formation of Co_9S_8 might result from the chemical reaction listed below:

$$9\ CoSO_4 + 17\ C = Co_9S_8 + SO_2 + 17\ CO_2$$

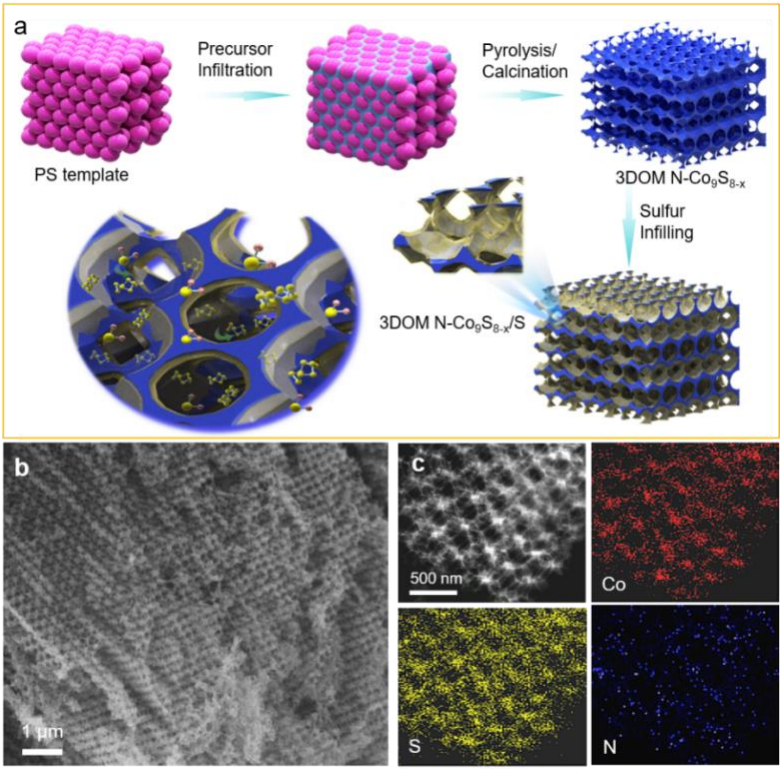

Figure 5.1 (a) Scheme illustration for the development of 3DOM N-Co_9S_{8-x} and its sulfur composites. SEM images of (b) 3DOM N-Co_9S_{8-x}; (c) The STEM and corresponding EDX element mapping image of 3DOM N-Co_9S_{8-x}.

Subsequently, the NH_3 etching introduces stupendous defects including N substitution and S vacancies into 3DOM Co_9S_8 (noted as 3DOM N-Co_9S_{8-x}). Noted that, a mild surface oxidation of 3DOM N-Co_9S_{8-x} is also observed in XPS spectrum, which might result from residual $CoSO_4$ or its exposure in air. The morphology of 3DOM N-Co_9S_{8-x} is revealed in Figure 5.1b. Clearly, the material still keeps its intact structure and porosity without damage, indicating the good controllability of defect engineering strategy. The STEM image and corresponding EDX element mapping in Figure 5.1c implies a homogeneous element distribution of Co, S and N. The hierarchical porous 3DOM N-Co_9S_{8-x} skeleton can offer abundant space for the filling of sulfur and electrolyte, large hollow interior to alleviate volume expansion, and facilitate ion/electron transportation within the electrode.

5.4 Structure elucidation of 3DOM N-Co_9S_{8-x}

To evaluate the advantages of structure design and defect engineering employed in this study, Co_9S_8 nanoparticle (Co_9S_8 NPs) and vacancy-free 3DOM Co_9S_8, were also synthesized. The XRD pattern shows that all these materials have typical diffraction pattern of Co_9S_8 (Figure 5.2a). As compared with 3DOM Co_9S_8 and Co_9S_8 NPs, the positive shift of XRD peaks in 3DOM N-Co_9S_{8-x} suggests the shrinkage of Co_9S_8 crystal owing to the defect engineering. Figure 5.2b shows the surface area and PSD of 3DOM N-Co_9S_{8-x}, which reveals its high BET surface area of 149.4 m_2 g_{-1} and hierarchical porosity. SEM images of 3DOM Co_9S_8 and Co_9S_{8-x} exhibit similar pore size and good structural integrity (Figure 5.2c, d). The HRTEM and corresponding FFT images of 3DOM Co_9S_{8-x} confirm the crystalline feature of Co_9S_8 (Figure 5.2e, f). Therefore, the large surface area and abundant hierarchical porosity homogenizes sulfur distribution and shorts electrolyte diffusion pathway inside electrode, favoring enhanced Li-S kinetics.

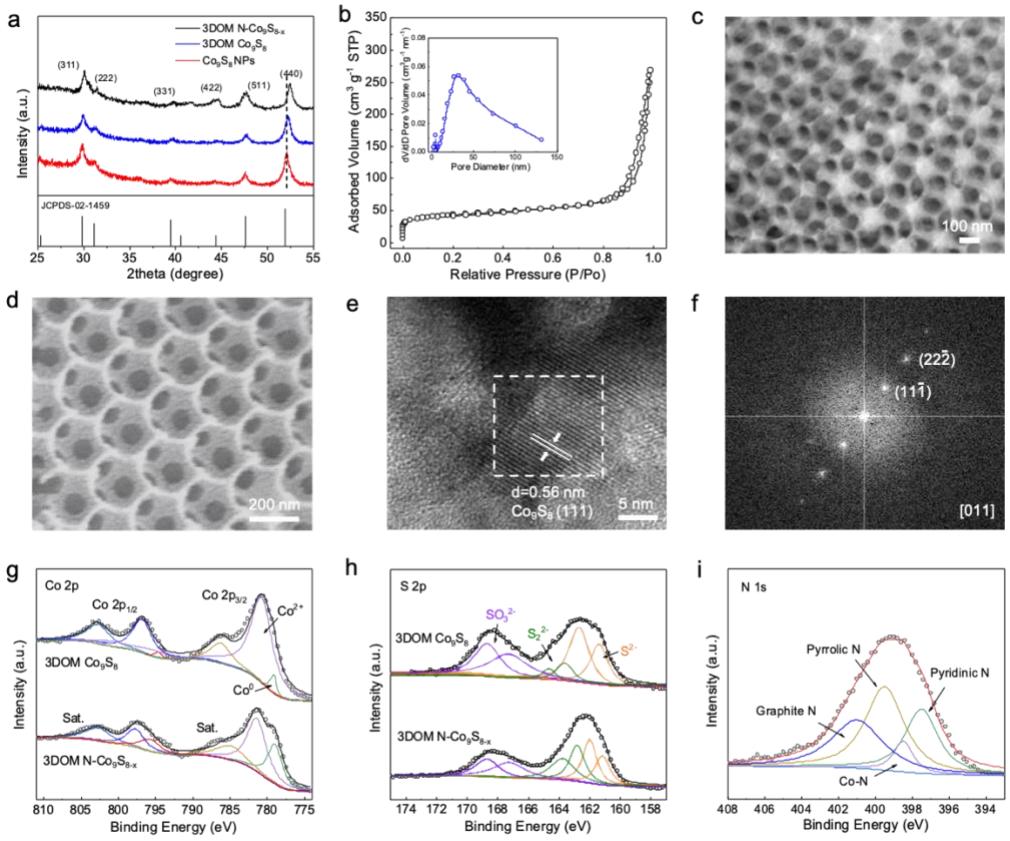

Figure 5.2 (a) XRD pattern of Co_9S_8 NPs, 3DOM Co_9S_8 and 3DOM N-Co_9S_{8-x}. (b) N_2 adsorption-desorption isotherms curves and the corresponding PSD of 3DOM N-Co_9S_{8-x}; (c) SEM image of 3DOM Co_9S_8 and (d) 3DOM N-Co_9S_{8-x}; (e) HRTEM image and corresponding FFT image (f) of 3DOM N-Co_9S_{8-x}; (g) Co 2p and (h) S 2p XPS spectra of 3DOM Co_9S_8 and 3DOM N-Co_9S_{8-x}; (i) N 1s XPS spectrum of 3DOM N-Co_9S_{8-x}.

To investigate the benefit of defect engineering, the surface chemistry of Co_9S_8 materials are analyzed by XPS. The Co 2p spectrum of 3DOM N-Co_9S_{8-x} shows a more legible metallic Co^0 state ($2p_{3/2}$ peak at 778.2 eV) than those of 3DOM Co_9S_8, suggesting its reduced surface state of Co by S vacancy (Figure 5.2g, h).[163] The S 2p spectra show three sets of peaks located between 160 eV and 168 eV, which can be ascribed to S_2^-, S_2^{2-} and

SO_x^{2-}.[164] Clearly, 3DOM N-Co_9S_{8-x} demonstrates the lowest SO_x^{2-} species intensity and an intensified S_2^{2-}/S^{2-} ratio among the three samples, indicating its reduced nature.[165] The N 1s spectrum of 3DOM N-Co_9S_{8-x} shows the existence of N-insertion in the bulk Co_9S_8 crystal (398.5 eV) (Figure 5.2i).[166] Moreover, the atomic composition of XPS analysis reveals that the S/Co atomic ratio of Co_9S_8 NPs and 3DOM Co_9S_8 is closes to the theoretical value of 0.89. However, this ratio in 3DOM N-Co_9S_{8-x} is decreased to 0.79, indicating the formation of S-deficient surface.[167] The defect and crystal structure distortion of 3DOM N-Co_9S_{8-x} was further investigated by X-ray absorption near-edge structure (XANES), extended X-ray absorption fine structure (EXAFS), electron energy-loss near-edge spectroscopy (ELNES) and electron paramagnetic resonance spectroscopy (EPR). The crystal structure of Co_9S_8 is shown in Figure 5.3a, which is constituted by CoS_6 octahedra and CoS_4 tetrahedra with a ratio of 1:8. To further analyze the content variation of CoS_6 octahedra in Co_9S_8 crystal after ammonia treatment, the XAS spectra of 3DOM N-Co_9S_{8-x}, 3DOM N-Co_9S_8 and CoS_2 were collected and compared. Since the CoS_2 only contains CoS_6 octahedra in its crystal structure, the CoS_2 Co *K*-edge XANES spectrum was used to represents the XAS spectra of CoS_6. Figure 5.3b shows the XANES spectra of 3DOM Co_9S_8 and 3DOM N-Co_9S_{8-x} in fluorescence yield (FLY) mode, which reveals the similar peak shape and adsorption edge (E_0), indicating the same valence state of Co in the bulk type of these samples. To identify the CoS_6 octahedra augment affected by defect engineering and the defective state on the surface and bulk of material, the principal component analysis and linear combination fitting (PCA-LCF) of Co *K*-edge XANES for 3DOM Co_9S_8 and 3DOM N-Co_9S_{8-x} was applied for both the surface sensitive total electron yield (TEY) spectra and FLY spectra (Figure 5.3c, d). The perfectly matched XANES

results and fitting curve for both TEY and FLY indicate a higher CoS_6 content of 17.6 % in 3DOM N-Co_9S_{8-x} in the TEY than FLY, suggesting that more CoS_6 octahedron is formed on the surface of 3DOM N-Co_9S_{8-x}. The 2 % CoS_6 content increasement is further revealed by LCF fitting results of S *K*-edge XANES spectrum under FLY mode (Figure 5.3e), which is similar with LCF fitting results of Co *K*-edge XANES spectrum. Figure 5.3f and g demonstrates Co *K*-edge EXAFS Fourier transform of 3DOM Co_9S_8 and 3DOM N-Co_9S_{8-x} in both TEY and FLY modes, in which the first shell located at 1.87 Å can be assigned to Co-S coordination. The EXAFS results display reduced peak intensity, indicating the decrease of coordination number and existence of S vacancies for 3DOM N-Co_9S_{8-x}. The above results indicate that the defect engineering strategy tunes some of the CoS_4 tetrahedron into CoS_6 octahedron and creates S vacancies on the octahedron sites for 3DOM N-Co_9S_{8-x}. To verify this point, ELNES analyzation were also provided (Figure 3h) to identify its structural distortion on the surface. ELNES can reflect the L-edge feature of Co, which is sensitive to the changes of valence state and high spatial resolution. The Co $L_{2,3}$-edge ELNES spectrum of 3DOM Co_9S_8 reveals a L_3/L_2 intensity ratio of 3.47, corresponding to an average Co valence of $Co^{2.5+}$.[78] Comparing with 3DOM Co_9S_8, the Co L_3 peak in 3DOM N-Co_9S_{8-x} undergoes negative shifts and the L_3/L_2 intensity ratio increased to 4.39, suggesting that the Co valence was reduced to $Co^{2.1+}$ on the surface, which is consistent with XPS analysis.[147] The EPR pattern in Figure 3i shows a signal with a g value of 1.99, suggesting the existence of S vacancies inside 3DOM N-Co_9S_{8-x}.[168] All these observations show that the ammonia treatment introduces N substitution inside Co_9S_8, which partially alters CoS_4 tetrahedron into CoS_6 octahedron, leading to the formation of S vacancies on octahedral sites. The defective surface offers multiple active sites to amplify

LiPS adsorption and conversion process toward superior kinetics, showing great promises to realize superior Li-S performance.

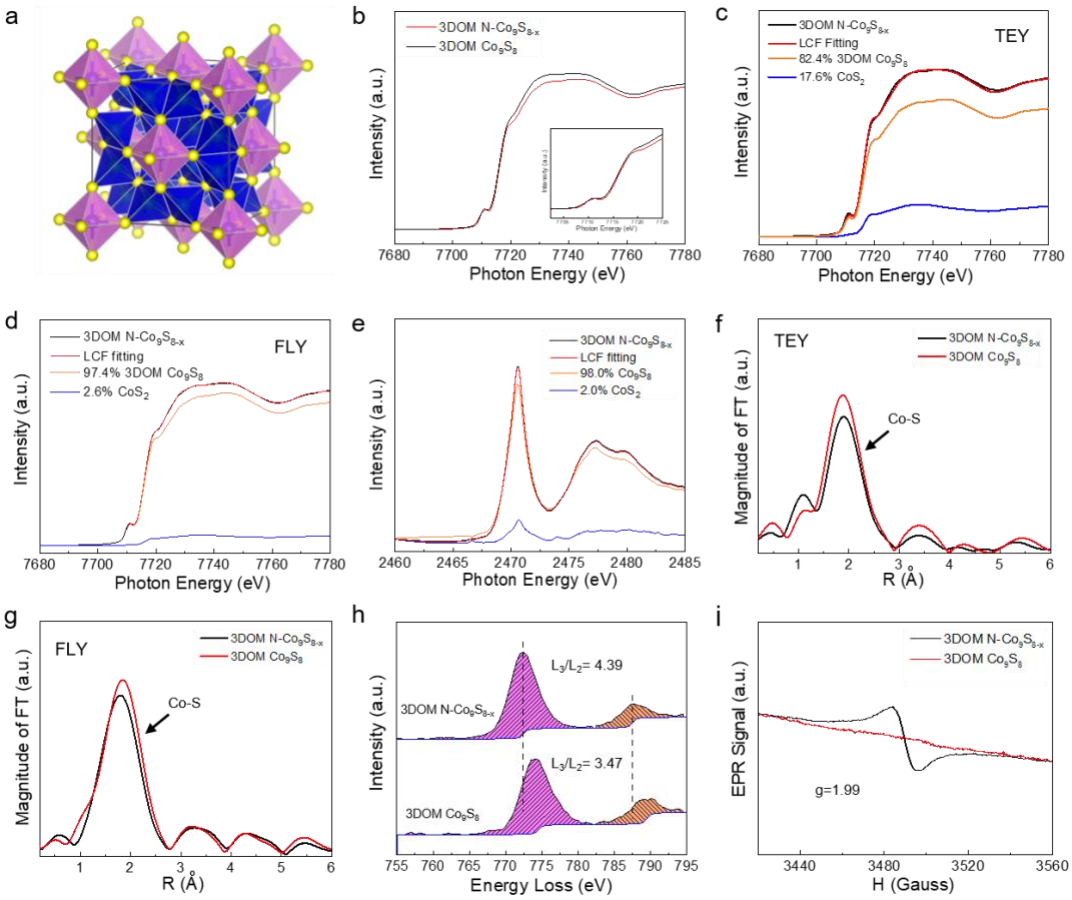

Figure 5.3 (a) Crystal structure of Co_9S_8, (b) The Co *K*-edge XANES spectra of 3DOM Co_9S_8 and 3DOM N-Co_9S_{8-x}; Co *K*-edge PCA-LCF fitting spectra from (c) TEY mode and (d) FLY mode; (e) S *K*-edge PCA-LCF fitting spectra of 3DOM N-Co_9S_{8-x}; (f) TEY and (g) FLY FT k_3-weighted Co *K*-edge EXAFS spectra of 3DOM Co_9S_8 and 3DOM N-Co_9S_{8-x}; (h) Co $L_{2,3}$-edge ELNES spectra of 3DOM Co_9S_8 and 3DOM N-Co_9S_{8-x}; (i) EPR signal of 3DOM Co_9S_8 and 3DOM N-Co_9S_{8-x}.

5.5 LiPS adsorptive and catalytic effect elucidation on N-Co_9S_{8-x}

To verify the enhanced LiPS adsorpbility of N-Co_9S_{8-x} on the defective sites, the adsorption energy (E_{ads}) of LiPS on Co_9S_8 and N-Co_9S_{8-x} (311) surface were calculated. The results show that N-Co_9S_{8-x} exhibits a higher E_{ads} than that on Co_9S_8 for all the Li_2S_2, Li_2S_6 and Li_2S_4 species (Figure 5.4d). The optimized adsorption configuration reveals that additional Co-S bonding was formed between LiPS species and N-Co_9S_{8-x}, which might contribute to its enhanced E_{ads}. In addition, the strengthened chemical interaction is revealed by XPS analysis (Figure 5.4a and b). Clearly, after Li_2S_6 adsorption, both Co $2p_{1/2}$ and Co $2p_{3/2}$ peaks of 3DOM N-Co_9S_{8-x}-Li_2S_6 shift to higher BE region. Meanwhile, the larger shift of S_{T-1} and S_{B0} peaks in the 3DOM N-Co_9S_{8-x}-Li_2S_6 indicates reduced electron density of S in LiPS.[148] The Li_2S_6 UV-vis spectra in Figure 5.4c shows a reduced peak intensity after adsorbed by 3DOM N-Co_9S_{8-x}, indicating its strong LiPS adsorption capabilities. These results strongly support that defective sites remarkably improve LiPS adsorption on 3DOM N-Co_9S_{8-x}, fulfilling the requirement to be used as sulfur immobilizer.

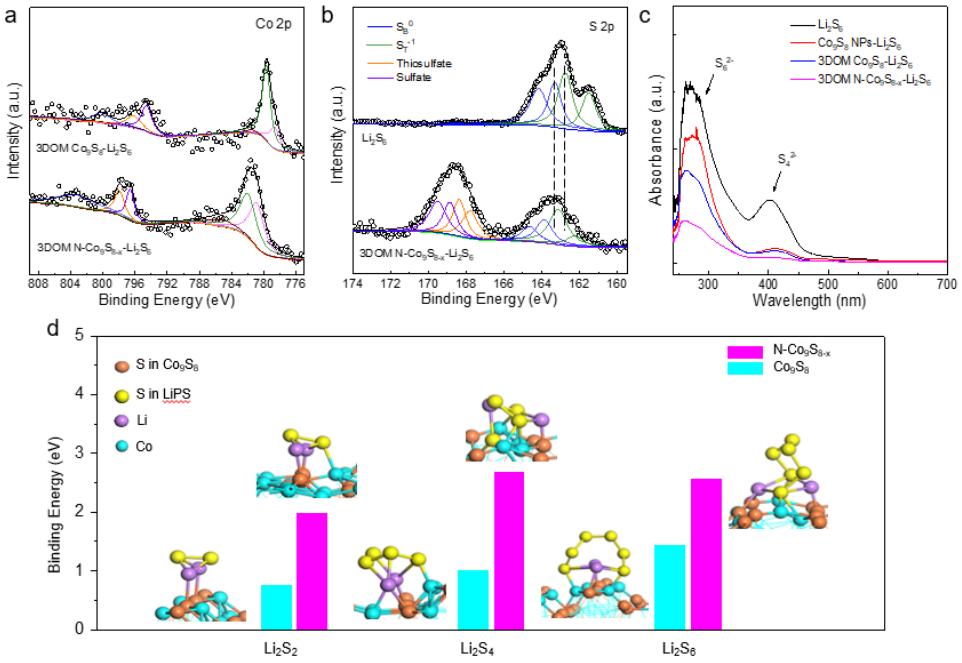

Figure 5.4 (a) Co 2p XPS spectra, (b) S 2p XPS spectra and (c) UV-vis spectra of 3DOM Co_9S_8 and 3DOM N-Co_9S_{8-x} after Li_2S_6 adsorption; (d) DFT optimized binding energies and geometries of Li_2S_2, Li_2S_4 and Li_2S_6.

The amplified S vacancies offers abundant active sites to accelerate the LiPS catalytic conversion, rendering favoured redox reaction. To verify this point, symmetrical cells were further assembled to evaluate the promoted LiPS conversion kinetics on the 3DOM N-Co_9S_{8-x} interface. Figure 5.5a-c demonstrates the CV curves with different scan rates of 3DOM N-Co_9S_{8-x}, 3DOM Co_9S_8 and Co_9S_8 NPs, respectively. The legible redox peaks represent the multi-step LiPS conversion reactions. 3DOM N-Co_9S_{8-x} exhibits the highest redox current response, suggesting its fast LiPS conversion. In Figure 5.5d, the 3DOM N-Co_9S_{8-x} exhibits the smallest resistance, corresponding to its favoured charge transfer process for fast LiPS conversion. To further demonstrate the enhanced catalytic behavior, potentiostatic discharge profiles of Li_2S_8/tetraglyme solution at 2.05 V were collected, as shown in Figure 5.5e and f. On the basis of calculating the integral of the current, the capacities of Li_2S precipitation on 3DOM N-Co_9S_{8-x} is evidently higher than that of 3DOM Co_9S_8, manifesting the superior activity and conversion behavior. The LiPS conversion kinetics on N-Co_9S_{8-x} was studied by calculating the energetics of Li_2S_2 decomposition pathway (Figure 5.5g). The results show that, on N-Co_9S_{8-x}, the Li_2S_2 need to overcome a barrier of 0.68 eV, which is much lower than that on ideal Co_9S_8 (1.02 eV). Overall, the defective N-Co_9S_{8-x} shows enhanced catalytic performance, achieving high kinetics for enhanced Li-S electrochemistry.[169]

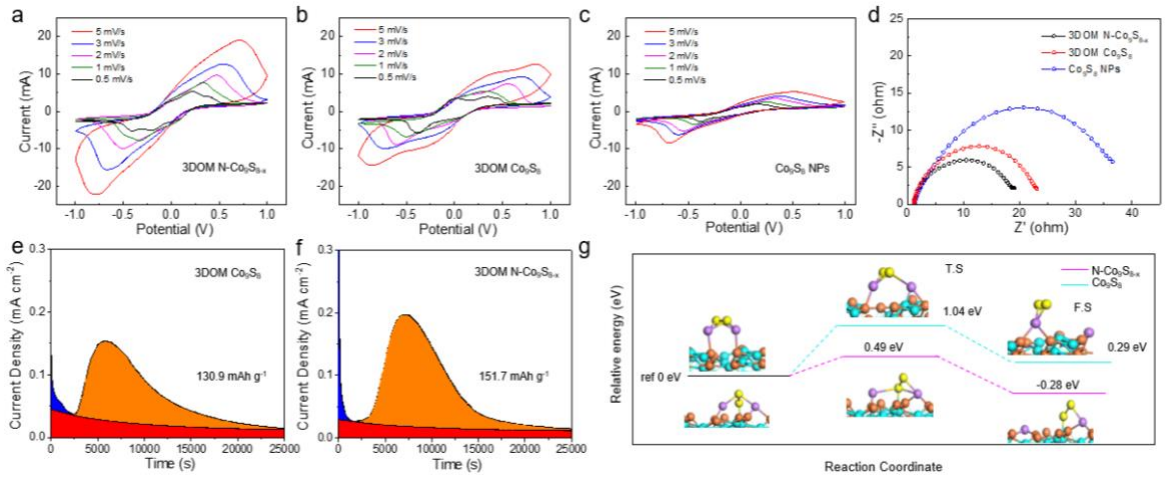

Figure 5.5 Kinetic and catalytic performance of different host materials: Symmetrical CV curves of (a) 3DOM N-Co_9S_{8-x}, (b) 3DOM Co_9S_8 and (c) Co_9S_8 NPs; (d) EIS spectra; (e, f) Potentiostatic discharge profiles of Li_2S_8/tetraglyme solution on various surfaces at 2.05 V; (g) energy profiles of Li_2S_2 decomposition on Co_9S_8 (311) and N-Co_9S_{8-x} (311) surface, T.S: transition state, F.S: final state.

5.6 Electrochemical performance evaluation of 3DOM N-Co_9S_{8-x}

In view of Li-S chemistry, 3DOM N-Co_9S_{8-x} sulfur composites were prepared by melt-impregnation method and its electrochemical performance was also evaluated. Figure 5.6a shows the GCD profiles of different cathodes. The discharge plateaus around 2.35 V and 2.1 V can be attributed to the reduction of sulfur to long-chain LiPS and further reduction to Li_2S_2 and Li_2S. Obviously, 3DOM N-Co_9S_{8-x} shows the smallest potential hysteresis and highest discharge capacity of 1252.9 mAh g^{-1}, indicating its high sulfur utilization and improved reaction kinetics. The CV curves in Figure 5.6b also exhibit two reduction peaks, which is consistent with the GCD profiles. Additionally, Figure 5.6c present the best rate performance of 3DOM N-Co_9S_{8-x} by showing the highest discharge capacity of 869.3 mAh g^{-1} at 5 C and 1193.9 mAh g^{-1} after the current switched back to 0.2 C. The EIS spectrum

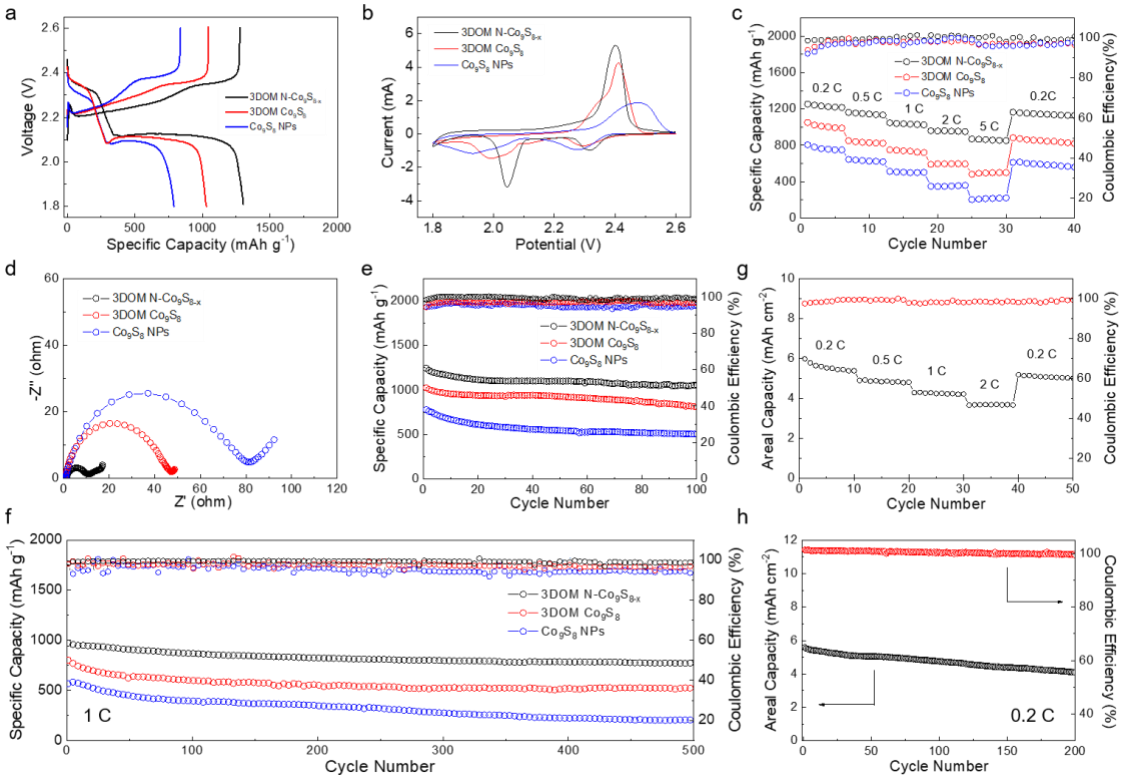

Figure 5.6 Electrochemical performance of Co_9S_8 NPs, 3DOM Co_9S_8 and 3DOM N-Co_9S_{8-x} sulfur composites: (a) GCD profiles under 0.2 C, (b) CV curves with a scan rate of 0.2 mV s^{-1}, (c) rate performance, (d) EIS spectra and (e) cycling performance under 0.2 C; (f) long-term cyclic stability under 1 C. Performance under raised sulfur loading of 6.5 mg cm^{-2} and low E/S ratio of 5: (g) rate performance and (h) cycling performance under 0.2 C.

of 3DOM N-Co_9S_{8-x} exhibits the smallest resistance for interfacial charge transfer process (Figure 5.6d). These results unveil the good kinetic behavior of 3DOM N-Co_9S_{8-x} attributed to its improved ion/electron transportation and superior LiPS catalytic effect. The cycling performance in Figure 5.6e demonstrates the highest discharge capacity of 1056.2 mAh g^{-1} with capacity retention of 84.8% over 100 cycles under the current density of 0.2 C, indicating its superior physical and chemical LiPS confinement. Attributed to these

synergistic features, 3DOM N-Co_9S_{8-x} achieves a high discharge capacity of 927.8 mAh g^{-1} after 500 cycles at 1 C (Figure 5.6f), corresponding to a remarkable cyclic stability with a low capacity fading rate of 0.04% per cycle. This sulfur electrode also demonstrates decent electrochemical performance under raised sulfur loading and low E/S ratio, which manifests a high initial capacity above 5.9 mAh cm^{-2} and decent rate capability (Figure 5.6g). Furthermore, the stable cycling operation also clarifies its good cyclic stability over 200 cycles (Figure 5.6h). The good Li-S performance is attributed to the synergistically combination of architectural and structural superiorities of 3DOM N-Co_9S_{8-x}.

5.7 Conclusion

In the present study, we have employed surface engineering strategy to design 3DOM N-Co_9S_{8-x} material as multifunctional sulfur immobilizer towards enhanced Li-S kinetics. The 3DOM structure homogenizes sulfur distribution, provides vast active interfaces and reduced ion diffusion pathway to expedite redox reaction. The hierarchical porosity of 3DOM N-Co_9S_{8-x} affords large void interior to store electrolyte and accommodate volume expansion. Meanwhile the defect engineering further introduces N substitution into Co_9S_8 to induce the transformation of some CoS_4 tetrahedron to CoS_6 octahedron, leaving abundant S vacancies on its octahedral sites. The abundant S vacancies further magnifies the adsorption capability and conversion kinetics of LiPS. Attributed to these superiorities, the 3DOM N-Co_9S_{8-x}/S cathode exhibits high sulfur utilization, enhanced LiPS chemisorption and electrocatalytic activity, leading to superior battery cyclability with a low capacity fading rate of 0.04% per cycle over 500 cycles at 1 C, good rate capability up to 5 C, and high areal capacity of 5.9 mAh cm^{-2}. This design strategy offers a synergistic

combination of architecture and defects design to enhance LiPS confinement and catalytic behavior, thereby enabling Li-S batteries with excellent sulfur kinetics and promoting its practical application.

Chapter 6 Synergistic Structure Design of Multifunctional Sulfur Immobilizer toward Superior Li-S Performance

6.1 Introduction

With the aim of facilitating the ion/electron conduction and promoting Li-S reaction kinetics, rational design of sulfur cathodes plays a critical role in upgrading the battery performance, which relies on: (1) nanostructuring and engineering high surface-to-volume ratio materials to shorten ion/electron transportation pathway, (2) integrating highly dispersive ultrafine NPs to enlarge active interfaces and enhance LiPS catalytic activity.[72] To this end, the development of well-tailored electrode structure encompassing the aforementioned principles is highly desired. In this regard, develop TMCs sulfur host with ultrafine NPs is able to meet these requirements. However, previously developed synthesis techniques cannot deliver a TMCs with small particle size (<5 nm). The ultrafine TMCs generally suffers from severe agglomeration when reducing its size, rendering limited active sites for LiPS adsorption and poor ionic/electronic transportations within electrode.

The spatial confinement of micro/mesopores in porous carbon can result in a size-limited growth of the rooted NPs even within angstrom scale, which is able to achieve highly dispersive ultrafine TMCs.[54, 57, 71] In previous chapter, we have demonstrated the superiorities by designing nanostructured cobalt based TMCs as sulfur stockpile. Herein, we aim to design ultrafine nanostructured cobalt based TMCs embedded in nanoporous carbon as sulfur host for boosted Li-S electrochemistry. However, preliminary results indicate the difficulty to obtain this composite with a desirable cobalt based TMCs content inlaid inside the pores, which may be pertained to the low formation energy of cobalt based TMCs on carbon substrate. The limited content of ultrafine particles offers insufficient

active interfaces to accelerate Li-S performance. Meanwhile, the immobilized cobalt based TMCs promote catalytic decomposition of carbon during material synthesis, which may cause the loss or aggregation of NPs and material degradation. In response to these challenges, we discovered that transitional metal compounds, such as Nb and Ta, demonstrates good implantation capability and compatibility inside the pores, offering considerable superiorities to be engineered with a desirable inlaid content.[25, 170] The abundant pores embedded with NPs is able to accommodate nanosized sulfur and regulate uniform Li_2S nucleation/growth inside the pore. By controlling the pore diameter and annealing atmosphere, the crystallinity and defective states of inlaid NPs could be manipulated for boosted LiPS affinity and catalytic activity.[171-173] Moreover, the synergistic combination of implantation strategy with defect engineering is expected to favor the electron/ion transfer and sulfur immobilization/catalyzation, rendering abundant active interfaces toward accelerated redox reaction.[174]

Herein, we developed a systematic method to synthesis ultrafine NPs porous carbon implantation architecture with controllable amorphous structure and oxygen vacancies for boosted Li-S performance. As for demonstration, Nb_2O_5 was selected as representative material to validate the capability of our strategy. Firstly, we reveal the superiority of amorphous and defective structure in strengthening LiPS adsorbability on Nb_2O_5. Inspired by this, ultrafine Nb_2O_5 NPs with amorphous structure and oxygen defects was rooted inside the porous carbon nanospheres, acting as the confined nanoreactor, with a high active surface-to-volume ratio and enhanced interactions with sulfur species. With the engineered 3-pronged spherical architecture, abundant interconnected pores implanted with Nb_2O_5, the composite architecture facilitates electrolyte infiltration, favors rapid

charge/mass transportation, as well as relieves the volume variation during lithiation. Hence, the Nb_2O_5-loaded nanoreactors not only possess both physical trapping and chemical binding for PS confinements, but also present an electrocatalytic effect, significantly accelerating the redox reaction kinetics. Owing to these superiorities, the as-developed amorphous oxygen-deficient Nb_2O_5 (A-Nb_2O_{5-x}) microporous carbon nanosphere nanocomposite (A-Nb_2O_{5-x}@MCS) sulfur electrode realizes an prevailing electrochemical performance, *i.e.*, high areal capacity of 6.62 mAh cm^{-2} under raised sulfur loading and decreased E/S ratio, high rate capability and stable cyclability with an extremely low capacity fading rate of 0.024% per cycle over a long-term operation of 1200 cycles. This strategy affords a synergistic combination of crystallinity modification, structural design and defects engineering towards rapid and durable sulfur electrochemistry, holding great potential in promoting the practical application of Li-S batteries.

6.2 Experimental section

6.2.1 Synthesis of and CoS_2@KJ

In a typical synthesis, 80 mg Ketjen Black EC600JD (KJ) carbon, which has enriched mesopores and concentrated PSD on ~4 nm, with adsorbed water vapor was placed inside a fused quartz tube under ammonium gas flow for several minutes at room temperature. Subsequently, the sample was immersed into saturated cobalt acetylacetonate ethyl acetate solution for 10 h. Then, the solid sample was filtrated and washed with ethyl acetate several times. After drying at 80 °C for 8 h, the collected sample was transferred to the center of a tube furnace. 2 g of sulfur powder was placed at the farthest upstream position in the tube furnace. The tube was purged with Ar and the sulfurization process was performed at 400 °C for 2 h, resulting in the formation of the CoS_2@KJ sample.

6.2.2 Synthesis of A-Nb_2O_5, T-Nb_2O_5 and Nb_2O_{5-x}

The Nb_2O_5 materials were synthesized *via* a thermal treatment process. In a typical reaction, $NbCl_5$ was dissolved in anhydrous ethanol under ultrasonication for 1 h to prepare 150 mM $NbCl_5$ ethanol solution and dried in vacuum oven at 80 °C overnight. The collected powder was transferred to furnace and annealed in Ar at 450 °C for 1 h with a ramping rate of 10°C/min to obtain amorphous Nb_2O_5 (A-Nb_2O_5). The orthorhombic Nb_2O_5 (T-Nb_2O_5) and oxygen-deficient Nb_2O_5 (Nb_2O_{5-x}) NPs were synthesized at 650 °C for 1 h under Ar atmosphere and Ar/H_2 atmosphere, respectively.

6.2.3 Synthesis composite materials

To synthesis MCS carbon, a 60 mL aqueous solution containing 0.6 M glucose was sealed in autoclave for hydrothermal reaction at 180 °C for 330 min. The brown precipitate was collected *via* filtration and washed by deionized water and dried overnight. The solid powder was then collected and impregnated into a 4 mL $ZnCl_2$ aqueous solution with a mass ratio of 1:4 and stir for 4 h. Next, the suspension was dried at 110 °C for 12 h followed by the vacuum drying overnight. The collected powder was ground inside the glovebox and transferred into tube furnace quickly and heated at 800 °C for 3 h under the CO_2 flow. Finally, the material was immersed in 3 M HCl under stirring for 1 h and washed with ethanol several times. The as-prepared $NbCl_5$ ethanol solution was added to MCS under ultrasonication for 2 h and dried at 80 °C under vacuum. The collected sample was heated in the Ar/H_2 atmosphere in tube furnace at 650 °C for 1 h to obtain A-Nb_2O_{5-x}@MCS. The A-Nb_2O_5@MCS without oxygen defects was prepared using the same collected sample but annealed in Ar atmosphere at 650 °C for 1 h. For T-Nb_2O_5@KJ and T-Nb_2O_{5-x}@KJ, the procedure is similar except replacing the MCS with KJ. The physically mixed samples T-

Nb_2O_5+KJ and A-Nb_2O_5+MCS were obtained by grinding the metal oxide and carbon together for 30 min, then annealed in Ar atmosphere at 650 °C for 1 h.

6.2.4 Physical characterization

The crystal structures were investigated by XRD (Bruker AXS D8). The morphology and microstructure were characterized by SEM (LEO FESEM 1530) and TEM (FEI Titan 80-300 LB). EELS characterization was performed under HAADF-STEM mode. The surface chemical composition of the samples was analyzed by XPS. XAS analyzation were performed at Canadian Light Source Inc, using the SXRMB beamlines. The *ex-situ* spectra of Nb L_3-edge were collected by TEY mode while the S *K*-edge spectra were collected by FLY mode. All XANES data were processed using Athena program. TGA was conducted on a TA instrument Q 500. EPR spectra was conducted on a Bruker EMX spectrometer at 77 K with a microwave frequency of 9.4 GHz and microwave power of 2 mW.

6.2.5 Electrochemical measurements

All sulfur composite samples were prepared by melting-diffusion method. The sulfur composite, Super P and PVDF was well mixed with a mass ratio of 8:1:1 in NMP to form the slurry. The composite electrodes were fabricated by coating the slurry on Al foil with a mass loading around 1 mg cm^{-2}. The Li foil was used as counter and reference electrode while the Celgard 2500 was used as separator. The electrolyte was prepared by well dissolved 1.0 M LiTFSI and 2 wt.% $LiNO_3$ in the mixed DOL/DME solvent. GCD process was performed on a Land CT2001A multi-channel battery tester within a cut-off voltage window of 1.8 V to 2.6 V at room temperature.

6.2.6 Li_2S nucleation test

The cell was assembled by using the identical electrode as working electrode and Li foil as counter electrode. 20 uL Li_2S_8 electrolyte (Li_2S_8 solution containing 2.0 mol L^{-1} [S] and 1 mol L^{-1} LiTFSI in tetraglyme was used as catholyte and 20 uL control electrolyte without Li_2S_8 was used as anolyte. The assembled cells were first discharged galvanostatically at 0.112 mA to 2.06 V and then discharged potentiostatically at 2.05 V. The potentiostatic discharge was terminated when the current was below 0.01 mA.

6.2.7 DFT calculations

The PBE function was used for the exchange and correlation energy terms. Li_2S_6 was selected as typical LiPS model and studied their absorption on A-Nb_2O_5, T-Nb_2O_5 (001) and Nb_2O_{5-x} (001) surfaces. A vacuum slab of about 15 Å was performed. The cell parameter of (1×2) supercell was constructed. The bottom two atomic layers were fixed whereas the remaining layers and the adsorbates were allowed to relax. For amorphous structure calculation, all layers and the adsorbates were allowed to relax. The k-space was sampled using a 2×2×1 Monkhorst-Pack grid. The BE was calculated as $BE = E_{total} - E_{ads} - E_{surf}$, where E_{total} is the total energy of the absorbed system, E_{ads} is the energy of the optimized Li_2S_6 in vacuum and E_{surf} is the energy of the optimized bare surface.

6.3 Morphology, structure and performance examination of CoS_2@KJ

CoS_2 and KJ was selected as representative active and host materials to investigate the implantation capability of cobalt based TMCs in the pores of porous carbon. After impregnating cobalt precursor into KJ and transferred for annealing process, the CoS_2@KJ nanoparticles can be obtained. SEM image (Figure 6.1A) reveals a uniform distribution and clean external surface of CoS_2@KJ without agglomeration, implying the successful

loading of CoS_2 inside the pores. The bright nanodomains in STEM image are the CoS_2 phase, whereas the dark domains are mainly the C phase from KJ carbon, indicating the non-uniform distribution of CoS_2 (Figure 6.1B). The high-resolution STEM image of CoS_2@KJ in Figure 6.1C indicates the sophisticated CoS_2 implantation structure with a size of ~7 nm. EDX elemental mappings of selected single particle also reveal the homogeneous elemental distribution of Co and S, confirming the formation of CoS_2@KJ (Figure 6.1D).

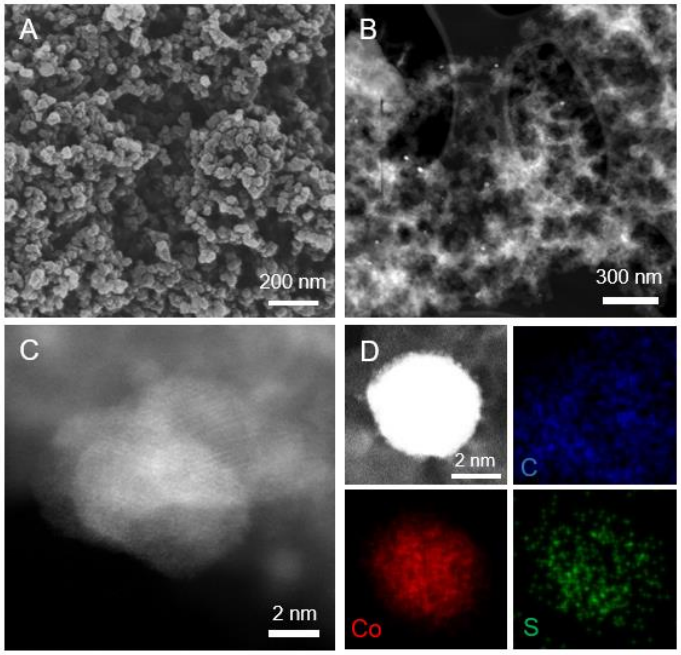

Figure 6.1 (A) SEM, (B) STEM and high-resolution STEM images of CoS_2@KJ; (D) EDX elemental mapping of CoS_2@KJ.

The structure information of CoS_2@KJ was further evaluated. The CoS_2 loading amount in the composite can be determined by TGA (Figure. 6.2A). TGA curve manifests a significant mass loss of 91.5 wt.% above 500°C, corresponding to the CoS_2 content of 12.4 wt.% inside composite. The crystalline nature of the as-prepared materials is confirmed by

XRD (Figure. 6.2B). All these peaks can be unequivocally attributed to cubic CoS_2 (JCPDS 41-1471),[19] which indicates that the cobalt precursor was thermally sulfurized. The BET surface analysis of KJ suggests its mesoporous feature with a large specific surface area of 1433 $m^2\ g^{-1}$ while the PSD reveals a high pore volume of 2.6 $cm^3\ g^{-1}$ and concentrated mesopores distribution between 2-8 nm (Figure 6.2 C and D). After implanted CoS_2 nanoparticles inside the mesopores of KJ, the obtained CoS_2@KJ well succeeds to the mesoporous texture without significantly sacrificing its specific surface area (880 $m^2\ g^{-1}$) and total pore volume (1.76 $cm^3\ g^{-1}$). The C 1s XPS spectra of KJ and CoS_2@KJ were also performed in Figure 6.2E and F. Three peaks can be observed at 284.8 eV, 285.7 eV and 288.8 eV, which can be deconvluted to C-C, C=C and C=O bonds, respectively.[138] A distinctive peak can be observed at ~283.5 eV in CoS_2@KJ, which may be related to the C-S bond between carbon matrix and CoS_2.[175] The chemical valence of CoS_2@KJ is determined by analyzing the de-convoluted Co 2p XPS spectrum (Figure 6.2G), indicating the only existence of Co^{2+}.[32,33] Moreover, the S 2p XPS spectrum also witnesses a broad peak at ~164 eV, which can be assigned to the Co-S bond of CoS_2.[165] These results confirm the formation of CoS_2@KJ implantation structure.

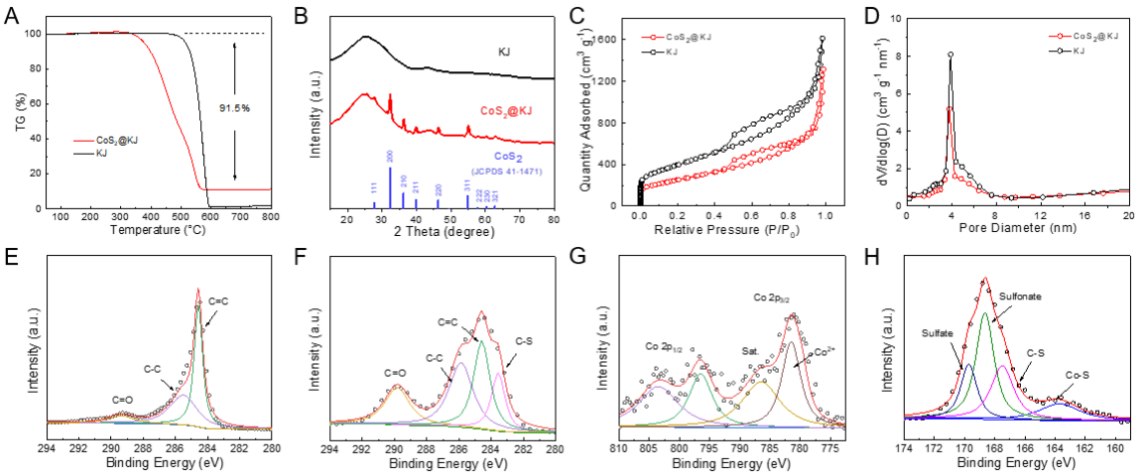

Figure 6.2 (A) TGA analysis and (B) XRD pattern of CoS_2@KJ and KJ; (C) N_2 adsorption-desorption isotherms and corresponding PSD of CoS_2@KJ and KJ; (E, F) C 1s XPS spectra of CoS_2@KJ and KJ; (G) Co 2p and (H) S 2p XPS spectra of CoS_2@KJ.

The CoS_2 NPs serves as active sites, which enhances the LiPS adsorption and redox reaction. To examine its performance improvement, CoS_2@KJ and KJ sulfur composites were prepared by melt-impregnation method and employed in Li-S batteries. The GCD profiles of CoS_2@KJ sulfur composites shows a higher discharge capacity of 1020 mAh g^{-1} and reduced potential hysteresis, indicating its enhanced redox reaction kinetics attributed to the strong LiPS interaction of CoS_2 (Figure 6.3A). The EIS spectra of CoS_2@KJ witnesses a reduced charge transfer resistance, indicating its favored charge transfer process (Figure 6.3B). The rate performance of CoS_2@KJ is further unveiled in Figure 6.3C. Comparing with KJ, CoS_2@KJ demonstrates a better rate capability with a higher discharge capacity of 475 mAh g^{-1} under the current density of 5 C, indicating its improved Li-S kinetics. After current switched back to 0.2 C, an admirable discharge capacity of 965 mAh g^{-1} can still be retained, indicating its high electrochemical reversibility. The cycling performance in Figure 6.3D also demonstrates the better cyclic stability with a lower capacity retention of CoS_2@KJ, corresponding to its enhanced sulfur confinement and strengthened chemical interaction with LiPS. Therefore, the sulfur host developed by this strategy is able to improve the Li-S performance.

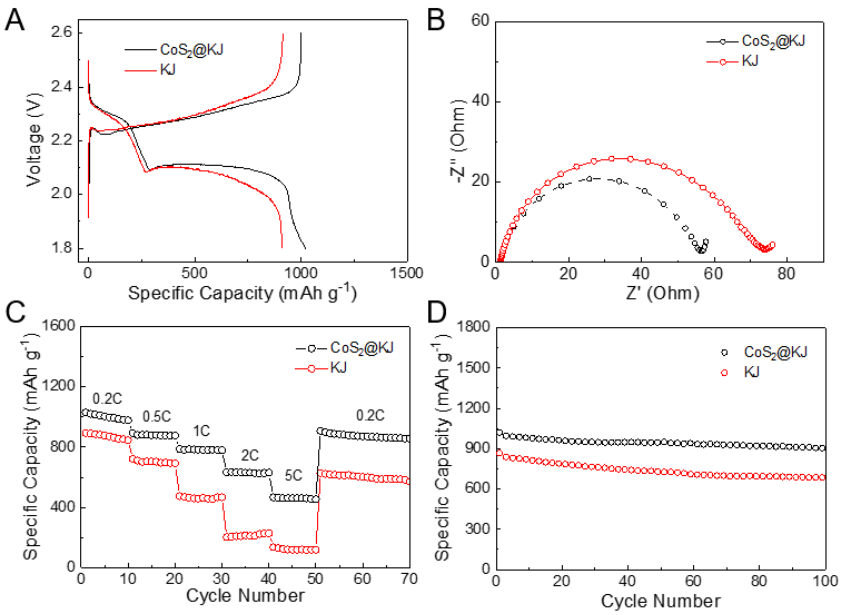

Figure 6.3 (A) GCD profiles, (B) EIS spectra, (C) rate performance and (D) cycling performance of CoS_2@KJ and KJ sulfur composites.

6.4 Tuning crystallinity, defective state of ultrafine NPs for fast redox reactions

Albeit this composite material facilitates ion/electron transportation within the electrode, the electrochemical performance is still not satisfied, especially under high C-rate. This could be ascribed to its large particle size and low CoS_2 content, which provides insufficient active interfaces for redox reaction. To further increase active sites and realize expedite performance under fast charge-discharge conditions, it is critical to reduce particle size for large surface-to-volume ratio and improve the content of TMCs. However, the cobalt based TMCs is unable to achieve both higher implantation content inside pores and ultra-small particle size, which may be related to the low formation energy and its catalytic decomposition effect with carbon substrates. Therefore, replacing cobalt based TMCs by other TMCs with strong affinity inside the carbon pores can well solve this problem. From

our investigation, the group 5 and 6 elements (Ta, Nb, W, Mo, etc) exhibits high implantation contents inside porous carbon and good compatibility with carbon substrate.[176] Given this, an elaborate architectural design is developed to acquire the size-limited growth of ultrafine and highly dispersive NPs. As for demonstration, ultrafine Nb_2O_5 NPs embedded porous carbon composites were successfully synthesized, as shown in Figure 6.4. Porous carbon, including microporous MCS and mesoporous KJ, are selected as substrates to confine NPs growth inside the pores. The MCS has a concentrated pore diameter of ~ 1.5 nm while the KJ has a concentrated pore diameter of ~4 nm. A facile wet-impregnation technique was employed to impregnate niobium ethoxide into the micropores of MCS (denoted as $Nb(OEt)_5$@MCS) and mesopores of KJ (denoted as $Nb(OEt)_5$@KJ) after alcoholysis. Following this, a high-temperature pyrolysis reaction was performed in inert atmosphere to yield the elaborate composite architecture with ultrafine NPs accommodated within the pores. The micropores of MCS is able to confine particle growth and inhibit its crystallization, rendering the formation of amorphous ultrafine Nb_2O_5. Meanwhile, the Ar/H_2 treatment will result in the formation of oxygen-defects on the surface. Therefore, by controlling annealing atmosphere during synthesis and pore diameter of porous carbon precursor, the ultrafine Nb_2O_5 NPs with desirable crystallinity and defective states can be obtained.

To investigate the effect of crystal structure manipulation on LiPS adsorbability, A-Nb_2O_5 and T-Nb_2O_5 were synthesized. The low crystallinity feature of A-Nb_2O_5 is revealed by XRD measurement, as shown in Figure 6.5A. The LiPS adsorption capability of A-Nb_2O_5 was evaluated by UV-vis spectra (Figure 6.5B). Comparatively, A-Nb_2O_5 shows lower intensity than T-Nb_2O_5, indicating the enhanced interaction with LiPS. According to DFT

calculation, T-Nb_2O_5 manifests a moderate E_{ads} of -1.75 eV with a Nb-S bond distance of 2.07 Å and Li-O bond distance of 2.38 Å (Figure 6.5D). Attributed to surface rearrangement, the A-Nb_2O_5 demonstrates a decent E_{ads} of -3.16 eV with a significantly reduced Li-O and Nb-S bond (Figure 6.5F), indicating its stronger LiPS adsorption.[177]

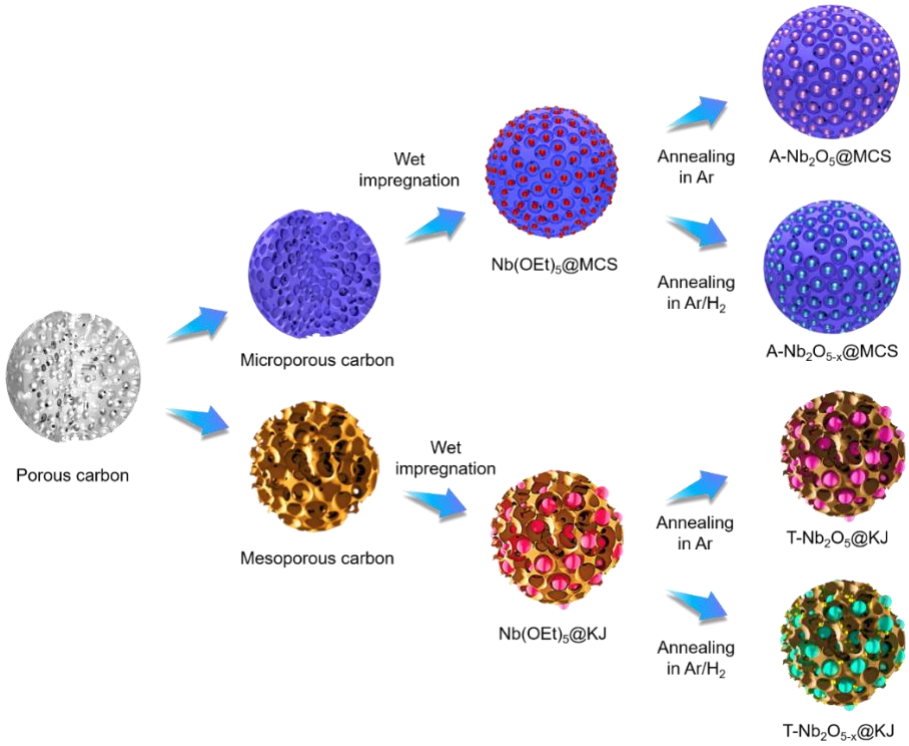

Figure 6.4 Scheme illustration of synthetic process of Nb_2O_5 composites materials with controllable oxygen vacancies and crystallinity by adjusting the pore diameter of carbon substrate and annealing atmosphere.

Nb_2O_5 sulfur composites were further employed as sulfur cathode material to examine their LiPS shuttling inhibition. Comparing with T-Nb_2O_5, A-Nb_2O_5 exhibits higher capacity with smaller potential hysteresis, indicating its favored LiPS interaction and facilitated redox reaction during charge-discharge process. Moreover, A-Nb_2O_5 shows

enhanced cyclic stability than T-Nb_2O_5, suggesting its effective suppression of LiPS shuttle effect (Figure 6.5G-I**)**. These results strongly support the advantages of amorphous structure design in sulfur host for high efficiency Li-S electrochemistry.

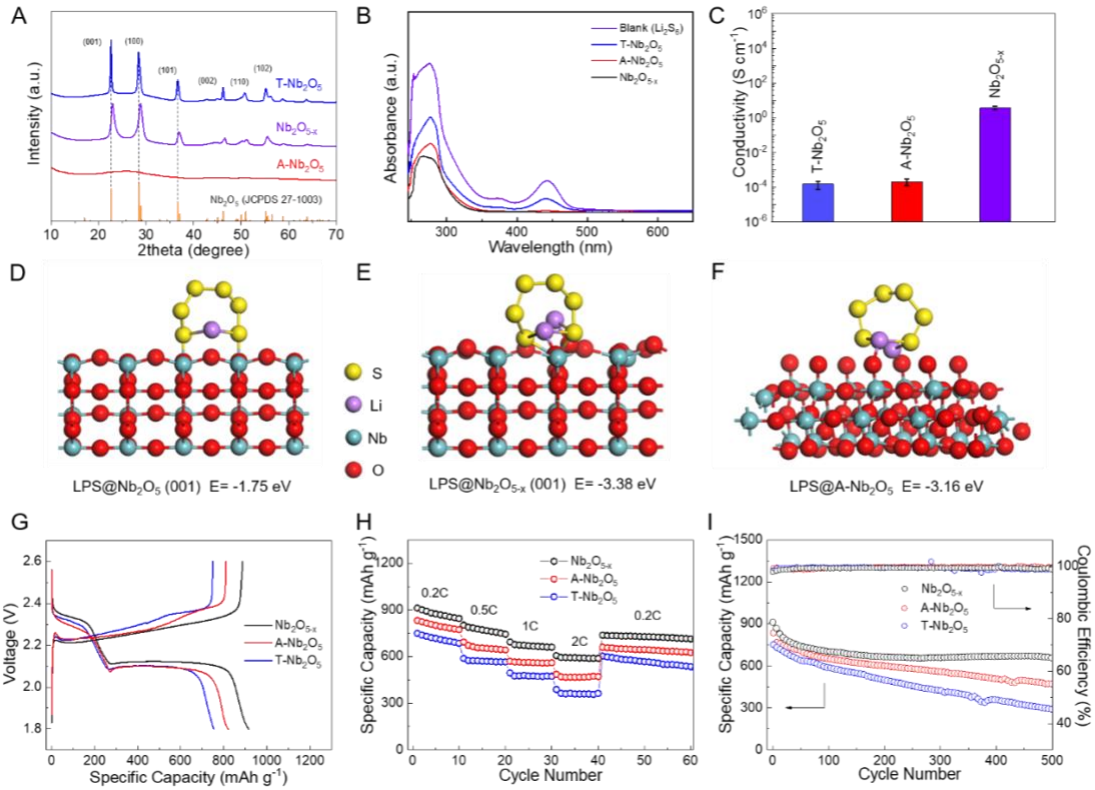

Figure 6.5 (A) XRD pattern, (B) UV-vis spectra of Li_2S_6 solution after adsorption and (C) electrical conductivities of T-Nb_2O_5, A-Nb_2O_5 and Nb_2O_{5-x}; Optimized geometric configuration and corresponding Li_2S_6 E_{ads} of (D) T-Nb_2O_5 (001), (E) Nb_2O_{5-x} (001) and (F) A-Nb_2O_5 (001); (G) GCD profiles at 0.2 C, (H) rate performance and (I) cycling performance at 0.2 C of Nb_2O_{5-x}, A-Nb_2O_5 and T-Nb_2O_5 sulfur cathode materials.

In addition, the importance of defect engineering for LiPS trapping is identified. Nb_2O_{5-x} is synthesized in Ar/H_2 atmosphere under 650 °C. The slight positive shift of XRD peaks in Nb_2O_{5-x} implies the structure distortion attributed to introduction of oxygen defects. The

UV-vis spectrum of Nb_2O_{5-x} exhibits a lower peak intensity than T-Nb_2O_5 and A-Nb_2O_5, indicating its stronger LiPS interaction. DFT calculation of Nb_2O_{5-x} (001) demonstrates a higher E_{ads} of -3.38 eV with reduced Li-O bond length (1.87 Å) and Nb-S bond length (2.34 Å), implying the enhanced LiPS affinity on oxygen vacancies (Figure 6.5E). Meanwhile, Nb_2O_{5-x} possesses the highest conductivity of 3.62 S cm^{-1}, indicating its best electron transfer within the bulk material (Figure 6.5C). The electrochemical performance of Nb_2O_{5-x} further confirms its enhanced LiPS adsorption. Notably, Nb_2O_{5-x} sulfur composite delivers the highest discharge capacity, best rate capability and cyclic stability, suggesting its improved redox reaction according to its enhanced electron conductivity and strong LiPS confinement (Figure 6.5G-I). The above results clearly manifest the superiorities of defect engineering in Nb_2O_{5-x} for the improvement of Li-S performance.

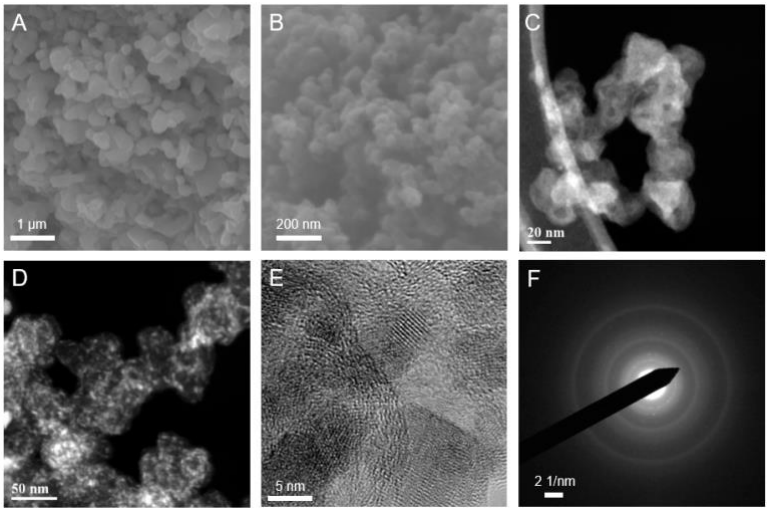

Figure 6.6 SEM image of (A) T-Nb_2O_5+KJ and (B) T-Nb_2O_5@KJ; STEM image of (C) KJ and (D) T-Nb_2O_5@KJ; (E) HRTEM and (F) SAD image of T-Nb_2O_5@KJ.

In view of the spatial confinement of porous carbon, $NbCl_5$ ethanol solution was dried under vacuum, mixed with KJ and annealed (denoted as T-Nb_2O_5+KJ). The obtained

material exhibits vast large size particle with a non-uniform size distribution (Figure 6.6A). However, the T-Nb_2O_5@KJ exhibits similar morphology with KJ by showing a smooth outside surface and uniform particles size within 100 nm. No agglomerate big particle can be observed, which indicates that T-Nb_2O_5 is fully embedded inside the pores of KJ (Figure 6.6B). The STEM images of KJ and T-Nb_2O_5@KJ also reveal a uniform distribution of ultrafine T-Nb_2O_5 inside the pores of KJ (Figure 6.6C and D). The HRTEM image in Figure 6.6E demonstrates the lattice fringe of embedded ultrafine particle, which can be assigned to the T-Nb_2O_5 (001) crystalline plane. The selected area diffraction pattern of T-Nb_2O_5@KJ shows the ring like pattern, indicating its nanocrystalline feature (Figure 6.6F).

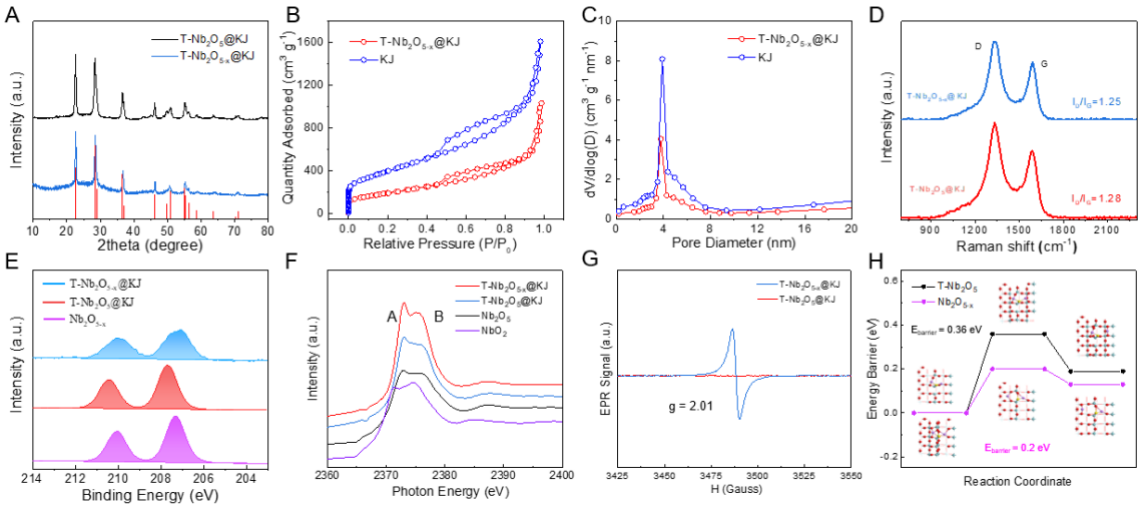

Figure 6.7 (A) XRD pattern of T-Nb_2O_5@KJ and T-Nb_2O_{5-x}@KJ; and (B, C) N_2 adsorption-desorption isotherms curves and the corresponding PSD of T-Nb_2O_{5-x}@KJ and KJ. (D) Raman spectra, (E) Nb 3d XPS spectra, (F) Nb L_3-edge XANES spectra and (G) EPR spectra of T-Nb_2O_5@KJ and T-Nb_2O_{5-x}@KJ; (H) Energy profiles and geometric configuration of Li_2S decomposition on Nb_2O_{5-x} (001) and T-Nb_2O_5 (001) surface.

The structural information was further revealed by XRD results (Figure 6.7A). The distinctive XRD peaks of T-Nb_2O_5@KJ and T-Nb_2O_{5-x}@KJ indicates that the impregnated Nb precursor will crystallize and form orthorhombic structure after annealing at 650 °C.[152] Moreover, a positive shift of XRD peak can be observed in T-Nb_2O_{5-x}@KJ, implying its reduced lattice fringe attributed to oxygen defects introduction. After decoration by T-Nb_2O_{5-x} nanoclusters, the obtained T-Nb_2O_{5-x}@KJ well succeeds to the mesoporous texture with a decent specific surface area (704 m_2 g_{-1}) and total pore volume (1.41 cm_3 g_{-1}), as shown in Figure 6.7B and C. The pore volume of T-Nb_2O_{5-x}@KJ is much lower than that of CoS_2@KJ, indicating a higher content of metal compounds inside the composites.

6.5 Defect engineering on ultrafine orthorhombic Nb_2O_5

In view of its defective structure formation, Raman spectra of T-Nb_2O_5@KJ and T-Nb_2O_{5-x}@KJ were performed to examine the defective states of KJ after annealing, which exhibit a very close D/G intensity ratio (I_D/I_G), suggesting their similar carbon structures with consistent degree of carbon defects (Figure 6.7D).[178] The high-resolution Nb 3d XPS spectra in Figure 6.7E exhibits Nb $3d_{3/2}$ and Nb $3d_{5/2}$ peaks located at 210.2 and 207.5 eV, indicating its valence feature of Nb^{5+}.[165] However, these two peaks in T-Nb_2O_{5-x}@KJ shift to lower BE region, corresponding the valence reduction of Nb.[172] Figure 6.7F displays the X-ray absorption near edge structure (XANES) spectroscopy of T-Nb_2O_5@KJ and T-Nb_2O_{5-x}@KJ, indicating their dominant valence of Nb^{5+}, which is consistent with XPS analyses. A double-peaked edge structure feature of Nb_2O_5 and NbO_2 are pertained to the interaction of Nb with surrounding O in the compound.[179] The intensity of peak A of all these samples is much higher than that of peak B, confirming their dominantly octahedral NbO_6 coordination.[180] The peak separation of A and B stems from the ligand field splitting

of Nb d-orbitals and the energy gap between A and B reflects the local symmetry of coordinated NbO_6.[181, 182] Therefore, the oxygen-deficient environment induce the oxygen vacancies formation in octahedral NbO_6, leading to severe structural distortion and reduced oxygen coordination number of Nb. T-Nb_2O_{5-x}@KJ delivers the smallest energy gap of 2.3 eV, which is lower than that of T-Nb_2O_5@KJ (2.8 eV) corresponding to the high distortion degree of octahedral symmetry (Table 6.1).[181] Moreover, T-Nb_2O_{5-x}@KJ delivers an EPR signal near a g-factor of 2.01, confirming the formation of oxygen vacancies in T-Nb_2O_{5-x}@KJ (Figure 6.7G).[183] The oxygen defects further enhances the electron conduction and bestows multiple active sites for efficient sulfur redox reaction.

Table 6.1. Peak position and energy gap (in eV) of Nb L_3-edge XANES spectra.

Sample	Peak A position	Peak B position	Energy gap between Peak A and B
Nb_2O_5	2373 eV	2375.9 eV	2.9 eV
NbO_2	2371.4 eV	2374.7 eV	3.3 eV
T-Nb_2O_5@KJ	2373 eV	2375.8 eV	2.8 eV
T-Nb_2O_{5-x}@KJ	2373 eV	2375.3 eV	2.3 eV
A-Nb_2O_5@MCS	2373 eV	2375.8 eV	2.8 eV
A-Nb_2O_{5-x}@MCS	2372.9 eV	2375 eV	2.1 eV

To further understand the importance of defect engineering and its substantial impact on Li-S kinetics, LiPS catalytic ability on oxygen vacancies was examined and the activation energies of Li_2S decomposition on Nb_2O_{5-x} and Nb_2O_5 were calculated (Figure 6.7H). Obviously, the Li_2S decomposition shows a much lower energy barrier on Nb_2O_{5-x} (0.2 eV) than that on T-Nb_2O_5 (0.36 eV), indicating the facilitated Li_2S conversion kinetics. This result confirms the enhanced catalytic effect on the defects in T-Nb_2O_{5-x}@KJ.

The electrochemical behaviors of sulfur cathodes based on these host materials were examined. Comparing with other electrodes, the GCD profiles of T-Nb_2O_5@KJ shows a high discharge capacity of 1048.9 mAh g^{-1} while T-Nb_2O_{5-x}@KJ shows the highest discharge capacity of 1211 mAh g^{-1} with smallest polarizations, suggesting the expedite sulfur kinetics when employing T-Nb_2O_{5-x}@KJ as sulfur host owing to its structural advancements (Figure 6.8A). The Nyquist plots of T-Nb_2O_{5-x}@KJ in Figure 6.8B shows the smallest R_{ct}, indicating its rapid charge transfer process attributed to the enhancement of ion/electron transportation. The multi-rate performance unveils the best rate capability of T-Nb_2O_{5-x}@KJ with a decent discharge capacity of 861.5 mAh g^{-1} at 5 C and high capacity of 1102.6 mAh g^{-1} after current switched back to 0.2 C, indicating its superb electrochemical reversibility (Figure 6.8C). Nevertheless, the T-Nb_2O_5@KJ and T-Nb_2O_5+KJ witness fast capacity fading to 623.2 and 408.5 mAh g^{-1} at 5 C, respectively. The cycling performance under current density of 0.2 C was further presented in Figure 6.8D. T-Nb_2O_{5-x}@KJ shows a high capacity retention of 81.5% over 300 cycles with a low capacity fading rate of 0.061% per cycle, indicating its enhanced LiPS confinement. T-Nb_2O_{5-x}@KJ demonstrates the highest capacity retention of 86.5%, corresponding to a low

fading rate of 0.045% per cycle, confirming its expedite physical and chemical LiPS confinement owing to the synergy of ultrafine structure design and defect engineering.

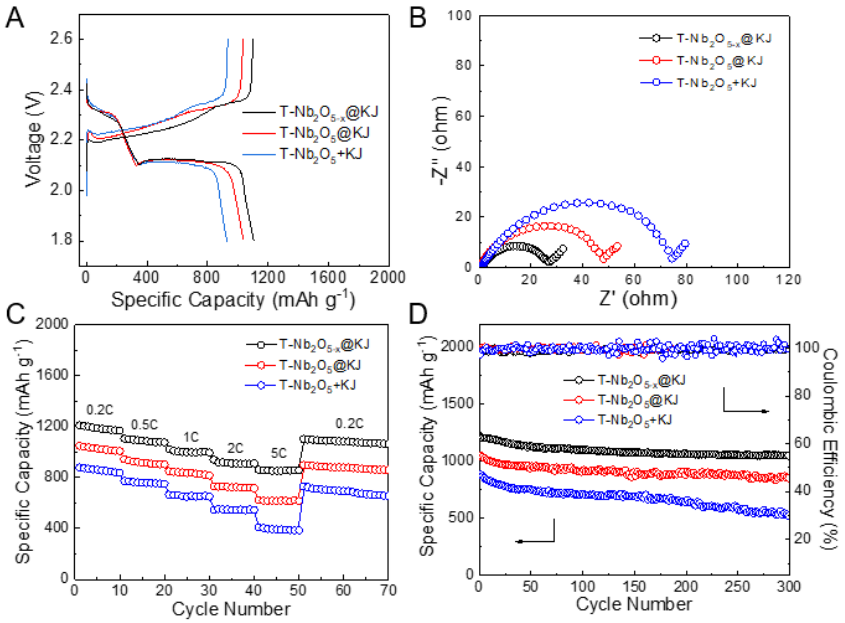

Figure 6.8 (A) GCD profiles, (B) EIS spectra, (C) rate performance and (D) cycling performance under 0.2 C of T-Nb_2O_5+KJ, T-Nb_2O_5@KJ and T-Nb_2O_{5-x}@KJ.

6.6 Synergistic engineering of defects and crystallinity on ultrafine Nb_2O_5

To further reduce the particle size and manipulate the crystallinity of Nb_2O_5, MCS was synthesized to confine the crystallization and growth of Nb_2O_5. After annealing in Ar atmosphere, A-Nb_2O_5@MCS can be obtained. For comparison, $NbCl_5$ ethanol solution was dried under vacuum, mechanically mixing with MCS, and annealed at 450 °C and 650 °C, separately (denoted as A-Nb_2O_5+MCS and T-Nb_2O_5+MCS). The spatial confinement of micropores constrains the structure change of A-Nb_2O_5, as revealed by XRD results (Figure 6.9A). No typical XRD peak can be seen in A-Nb_2O_5+MCS while the T-Nb_2O_5+MCS exhibits XRD peaks of orthorhombic Nb_2O_5, indicating the crystallization

inhibition owing to the spatial confinement effect of micropores. However, A-Nb_2O_5@MCS only shows a broad peak at 26°, implying its amorphous feature. In Figure 6.9B, the typical I type isotherm of MCS suggests its microporous feature, which possesses a large surface area of 2492 m^2 g^{-1}, pore volume of 1.50 cm^3 g^{-1} and average pore diameter of ca. 1.3 nm (Figure 6.9C). The well-matched particle size and the diameter of pores indicates the implantation of nanocluster inside micropores. After decoration by A-Nb_2O_5 nanoclusters, the obtained A-Nb_2O_5@MCS well succeeds to the initial microporous texture of MCS without significantly sacrificing its specific surface area (1834 m^2 g^{-1}) and total pore volume (1.21 cm^3 g^{-1}). By contrast, reduced surface area (1258 m^2 g^{-1}) and total pore volume (0.70 cm^3 g^{-1}) can be observed in A-Nb_2O_5+MCS, according to the pore clogging and porosity spoilage by physical mixing. Therefore, the spatial confinement of micropores not only restrains the size growth of rooted Nb_2O_5 nanocluster, but also inhibits the crystallization and structural change to deliver an amorphous structure.

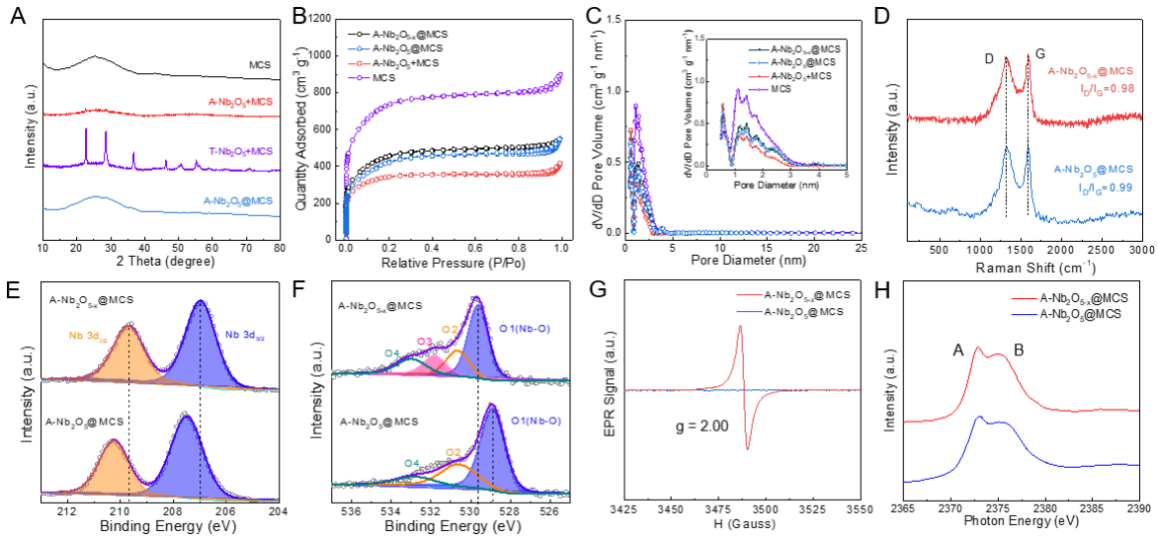

Figure 6.9 (A) XRD pattern, (B) N_2 adsorption-desorption isotherms and (C) corresponding PSD of A-Nb_2O_{5-x}@MCS, A-Nb_2O_5@MCS, A-Nb_2O_5+MCS and MCS; (D)

Raman spectra, (E) Nb 3d XPS spectra, (F) O 1s XPS spectra, (G) EPR pattern and (H) Nb *L*$_3$-edge XANES spectra of A-Nb_2O_{5-x}@MCS and A-Nb_2O_5@MCS.

To further understand the structure change induced by defect engineering, the A-Nb_2O_{5-x}@MCS was synthesized. TEM image demonstrates the morphology of A-Nb_2O_{5-x}@MCS, which shows clean external surface without particle aggregation (Figure 6.10A). The homogenous distribution of Nb and O in EDX mapping (Figure 6.10B) corroborates a highly uniform dispersion of A-Nb_2O_{5-x} throughout the skeleton of MCSs. The rooted A-Nb_2O_{5-x} nanocluster can be seen in the micropores of MCS framework. (Figure 6.10C-E). The EELS mapping (Figure 6.10F-H) reveals the recessed growth of intact A-Nb_2O_{5-x} nanocluster within carbon pores. Comparing with the XRD pattern of T-Nb_2O_5 (Figure 6.9A), the diffraction peaks of A-Nb_2O_5@MCS shifts to higher region, indicating its reduced lattice fringe attributed to amorphous structure design. The further shifts of A-Nb_2O_{5-x}@MCS is related to the structure distortion induced by oxygen vacancies implantation. Raman spectra in Figure 6.9D reveals a very close D/G intensity ratio (I_D/I_G) between A-Nb_2O_{5-x}@MCS (0.98) and A-Nb_2O_5@MCS (0.99), suggesting their similar carbon structures with similar carbon defects content.[184] The Nb 3d XPS spectra in Figure 6.9E also indicates its valence feature of Nb^{5+}. Meanwhile, a negative peak shift can be observed in A-Nb_2O_{5-x}@MCS, confirming the valence reduction of Nb in the A-Nb_2O_{5-x}. Besides, A-Nb_2O_5@MCS exhibits three sub peaks (O1, O2, and O4) in high-resolution O 1s spectra, corresponding to the Nb-O bond, hydroxylated surface and adsorbed moisture, respectively (Figure 6.9F).[165] However, the O1 peak of A-Nb_2O_{5-x}@MCS shifts up to a higher BE region while a particular O3 peak appears at 532.0 eV, which indicates oxygen

defects formation.[140] The EPR pattern witnesses a strong signal at g = 2.0, confirming a large proportion of oxygen vacancies in A-Nb_2O_{5-x} (Figure 6.9G).[141] Figure 6.9H shows the XANES spectra of A-Nb_2O_5@MCS and A-Nb_2O_{5-x}@MCS. Comparing with A-Nb_2O_5@MCS, A-Nb_2O_{5-x}@MCS shows a negative peaks shift and lower energy gap between A and B of 2.1 eV, implying partial valence reduction and defects formation on the surface, consistent with XPS analyzations (Table 6.1).[184] These results confirm the existence of defects on the surface of A-Nb_2O_{5-x}@MCS, which enhances the electron conduction and bestows multiple active sites for efficient sulfur redox reaction.

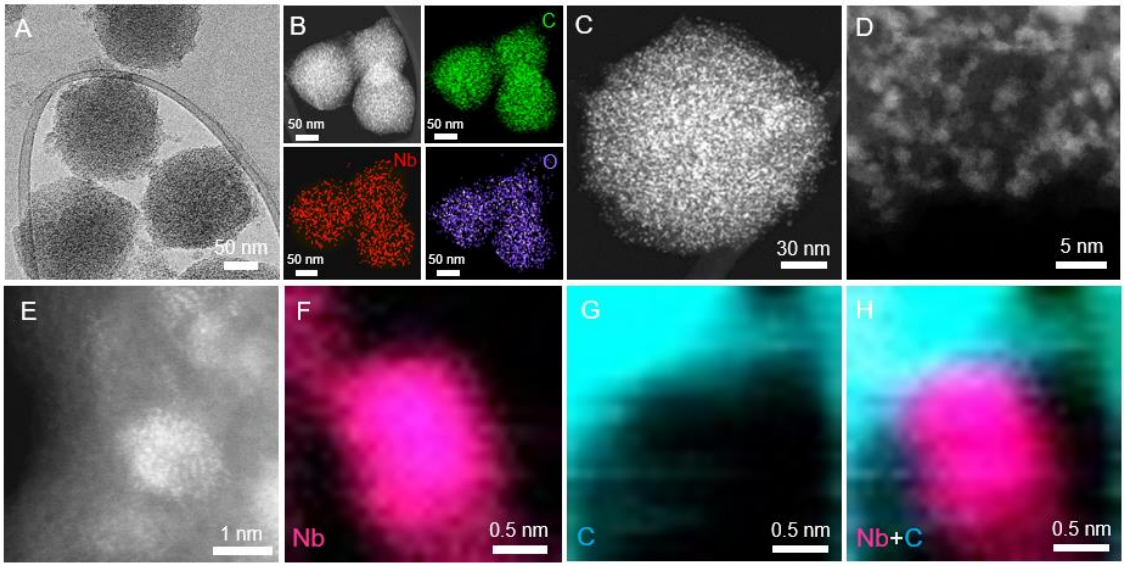

Figure 6.10 (A) TEM image, (B) EDX element mapping, (C) STEM image of A-Nb_2O_{5-x}@MCS; (D, E) STEM image of A-Nb_2O_{5-x} nanocluster and the corresponding EELS elemental mappings of (F) Nb, (G) C and (H) mixture.

The strong LiPS interaction of A-Nb_2O_{5-x}@MCS can be understood by XPS analyses. A large positive shift can be observed in A-Nb_2O_{5-x}@MCS-Li_2S_6 XPS spectra, indicating its strong LiPS chemisorption **(**Figure 6.11A**)**.[181, 185] A pair of sulfate/sulfite peaks were

emerged in the high BE region, manifesting chemical bondage between the defective sties and LiPS.[138] Besides, a positive shift of O1 peak can be observed in Figure 6.11B, indicating the reduction of electron cloud density of O in A-Nb_2O_{5-x}, induced by "lithium bond"-like interactions between A-Nb_2O_{5-x} and LiPS.[186] The LiPS catalyzation is verified by *ex-situ* XANES measurements. Figure 6.11C and E show the Nb L_3-edge spectra of A-Nb_2O_{5-x}@MCS, A-Nb_2O_5@MCS sulfur composite cathode cycling at 0.2 C (1C=1675 mAh g^{-1}). The corresponding status is shown in Figure 6.11G. During the 1st discharge-charge process, the peaks A and B of A-Nb_2O_5@MCS remain at the same position with an energy gap around 3.1 eV, implying the octahedral symmetry of A-Nb_2O_5 without structural change. However, the A-Nb_2O_{5-x}@MCS shows a reduced half-peak width with a lower energy gap of 2.3 eV. The energy gap enlarges to 2.75 eV in spectrum III and reduces to 2.45 eV in spectrum V (Figure 6.11C), confirming the reversible change of distorted structure. Figure 6.11D and F show the S *K*-edge XANES spectra of A-Nb_2O_{5-x}@MCS and A-Nb_2O_5@MCS. The peaks A and B in Li_2S_4 and Li_2S_6 reference spectra (Figure 6.11H) correspond to the transition of S 1s to π* state and S 1s core level to S-S π* state [152] while the peak C can be assigned to Li_2S.[187] The S_x^{2-} peak emerges during discharge process and reduced after fully discharged, indicating the conversion of sulfur to LiPS and further reduction to Li_2S. The gradually decreased S-S peak and increased Li_2S peak intensity during discharge process indicates the reduction of sulfur. The spectrum II shows the early formation of Li_2S at the initial stage of discharge, revealing its lowered discharge overpotential and the improved kinetics.[188]

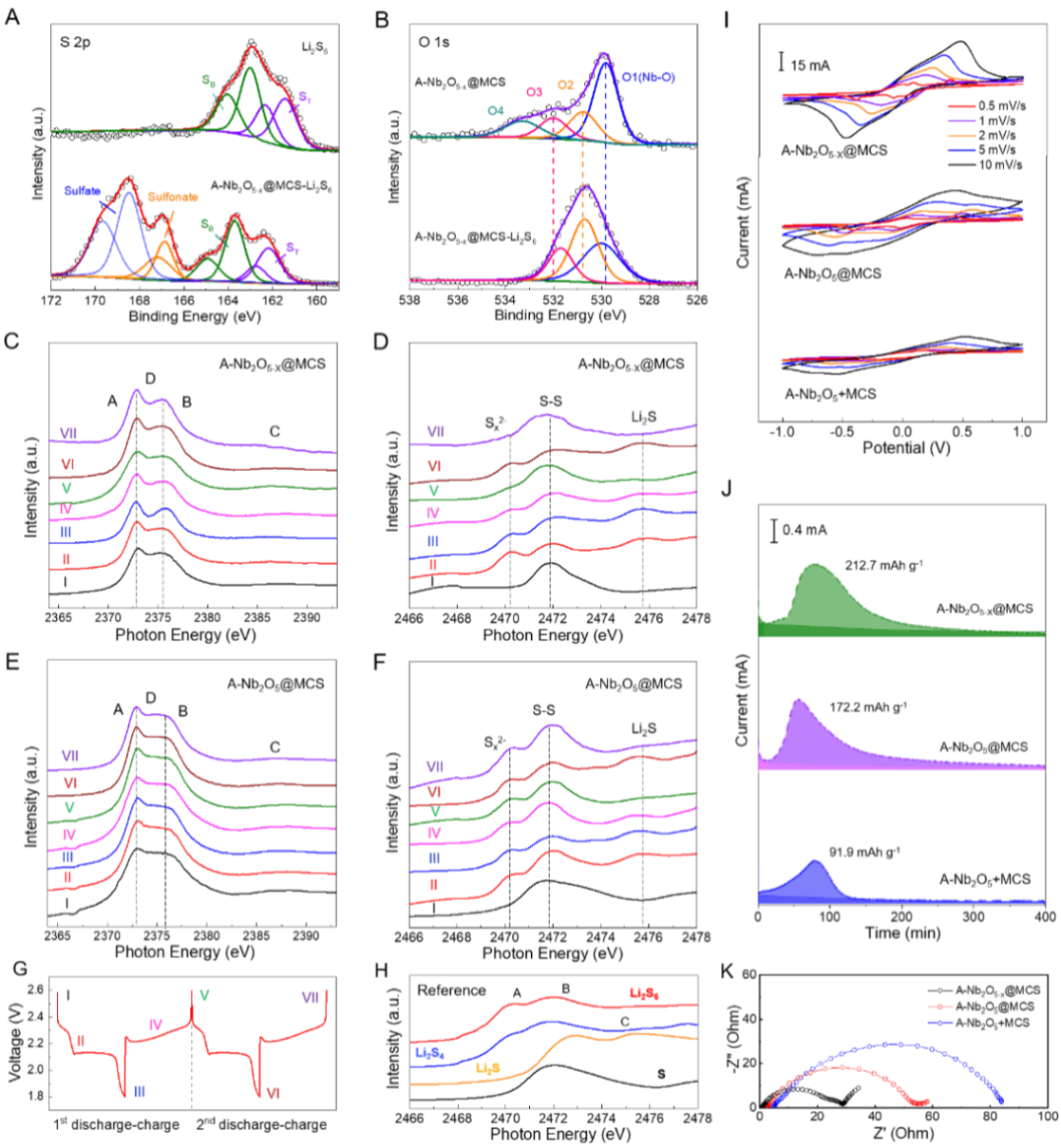

Figure 6.11 LiPS interaction and catalyzation characterizations: (A) S 2p and (B) O 1s XPS spectra for A-Nb_2O_{5-x}@MCS and A-Nb_2O_{5-x}@MCS-Li_2S_6; Evolution of Nb *L*$_3$-edge and S *K*-edge XANES spectra of (C, D) A-Nb_2O_{5-x}@MCS and (E, F) A-Nb_2O_5@MCS sulfur cathode during electrochemical cycling at 0.2 C; (G) the discharge/charge status of the sulfur electrode collected for *ex-situ* XANES analyzations: (I) initial status, (II) discharge to 2.15 V, (III) discharge to 1.8 V, (IV) charge to 2.3 V, (V) charge to 2.6 V, (VI) discharge to 1.8 V and (VII) charge to 2.6 V; (H) reference S *K*-edge XANES spectra of

LiPS and S; (I) symmetric CV curves and (K) EIS spectra of A-Nb_2O_{5-x}@MCS, A-Nb_2O_5@MCS and A-Nb_2O_5+MCS; (J) Potentiostatic discharge profile at 2.05 V.

A-Nb_2O_{5-x}@MCS shows a more dampened S-S/S_{x2-} peak intensity ratio in spectrum II and legible Li_2S peak in spectrum III, which indicates its favored sulfur reduction (Figure 6.11D). Much smaller S_{x2-} and Li_2S peaks can be seen in the spectrum V of A-Nb_2O_{5-x}@MCS, suggesting its more completed LiPS conversion after fully charged.[72] During the 2nd discharge-charge process, A-Nb_2O_5@MCS still exhibits a 3 eV energy gap between peak A and B under the fully discharged and charged state (VI and VII), indicating its unobvious structure change. However, A-Nb_2O_{5-x}@MCS demonstrate an increased energy gap of 2.7 eV at fully discharged state (VI) and reduced to 2.4 eV at fully charged state (VII), confirming the reversible structure distortion evolution. These results confirm an efficient and stable LiPS adsorption-conversion-desorption process on A-Nb_2O_{5-x}@MCS, which could serve as a promising electrocatalyst for the promotion of sulfur conversions.

To further gain insight into the synergistic effect of ultrafine amorphous structure design and oxygen defects implantation of Nb_2O_5 for expedite sulfur chemistry, the symmetric cells using A-Nb_2O_5+MCS, A-Nb_2O_5@MCS and A-Nb_2O_{5-x}@MCS as identical electrodes were investigated. Figure 6.11I demonstrates the different scan rates CV curves of symmetric cells, where the distinctive redox peaks represent the multi-step LiPS conversion reactions. The results reveal the continuous increase of current response and decrease of polarizations from A-Nb_2O_5+MCS to A-Nb_2O_5@MCS to A-Nb_2O_{5-x}@MCS, indicating the kinetic improvements. Figure 6.11K shows their EIS spectra. The A-Nb_2O_{5-x}@MCS shows the lowest R_{ct}, suggesting its fast LiPS adsorption and conversion. Apart

from that, the electrocatalytic activity is analyzed by Li_2S nucleation test (Figure 6.11J). The A-Nb_2O_5@MCS exhibits a higher capacity and earlier responsivity of Li_2S nucleation than A-Nb_2O_5+MCS, confirming the reduced overpotential for initial Li_2S nucleation and rapid kinetics to promote Li_2S precipitation.[188, 189] A-Nb_2O_{5-x}@MCS delivers the highest capacity, indicating its fast Li_2S nucleation and precipitation process. All these results strongly demonstrate the superior catalytic activity and durability of A-Nb_2O_{5-x}@MCS.

Table 6.2 Peak position and energy gap (in eV) of A-Nb_2O_{5-x}@MCS-S, A-Nb_2O_5@MCS-S and A-Nb_2O_5+MCS-S in Nb *L*$_3$-edge XANES spectra during discharge-charge process.

Sample		Pristine electrode (I)	Discharge to 2.15 V (II)	Discharge to 1.8 V (III)	Charge to 2.3 V (IV)	Charge to 2.6 V (V)
A-Nb_2O_{5-x}@MCS-S	Peak A position	2373	2373	2373	2373	2373
	Peak B position	2375.3	2375.5	2375.7	2375.6	2375.4
	Energy gap between A and B	2.3	2.5	2.7	2.6	2.4
A-Nb_2O_5@MCS-S	Peak A position	2373	2373	2373	2373	2373
	Peak B position	2376.2	2376.1	2376.1	2376.1	2376.1
	Energy gap between A and B	3.2	3.1	3.1	3.1	3.1

The GCD profiles in Figure 6.12A reveals the best Li-S performance of A-Nb_2O_{5-x}@MCS, which demonstrates the highest discharge capacity of 1342 mAh g^{-1} and the smallest potential gap between charge and discharge plateaus. Figure 6.12B shows the Nyquist plots

of different sulfur electrode. A-Nb_2O_{5-x}@MCS shows the smallest R_{ct}, indicating its favored charge/mass transportation. The multi-rate performance in Figure 6.12C unveils the best rate capability of A-Nb_2O_{5-x}@MCS with a decent discharge capacity of 941.9 mAh g^{-1} at 5 C and high capacity of 1210.3 mAh g^{-1} after current switched back to 0.2 C. Nevertheless, the MCS, A-Nb_2O_5+MCS and A-Nb_2O_5@MCS witness fast capacity fading to 127.2, 348.1 and 694.7 mAh g^{-1} respectively at 5 C. The cycling performance of A-Nb_2O_{5-x}@MCS in Figure 6.12D demonstrates the highest discharge capacity of 1056.6 mAh g^{-1}, high capacity retention of 81.8% and high coulombic efficiency close to 100% over 100 cycles, indicating its superior physical and chemical LiPS confinement. To further understand the structural stability for long-term operation, the ultra-long cyclic stabilities were further examined (Figure 6.12E). A-Nb_2O_5@MCS exhibits a low capacity fading rate of 0.034% per cycle over 1200 cycles, attributed to the superiority of nanocluster implanted microporous structure, which efficiently traps sulfur species and accelerates their redox reactions. Beyond that, A-Nb_2O_{5-x}@MCS shows an extremely low capacity fading rate of 0.024% per cycle at 1 C. These enhancements in capacity, rate capability and cyclability of A-Nb_2O_{5-x}@MCS are attributed to the synergistic regulations of crystallinity nature, defect chemistry and nanoreactor architecture, which immobilize LiPS species and effectively catalyze their electrochemical conversions toward excellent LiPS shuttle suppression and Li-S kinetic enhancement.

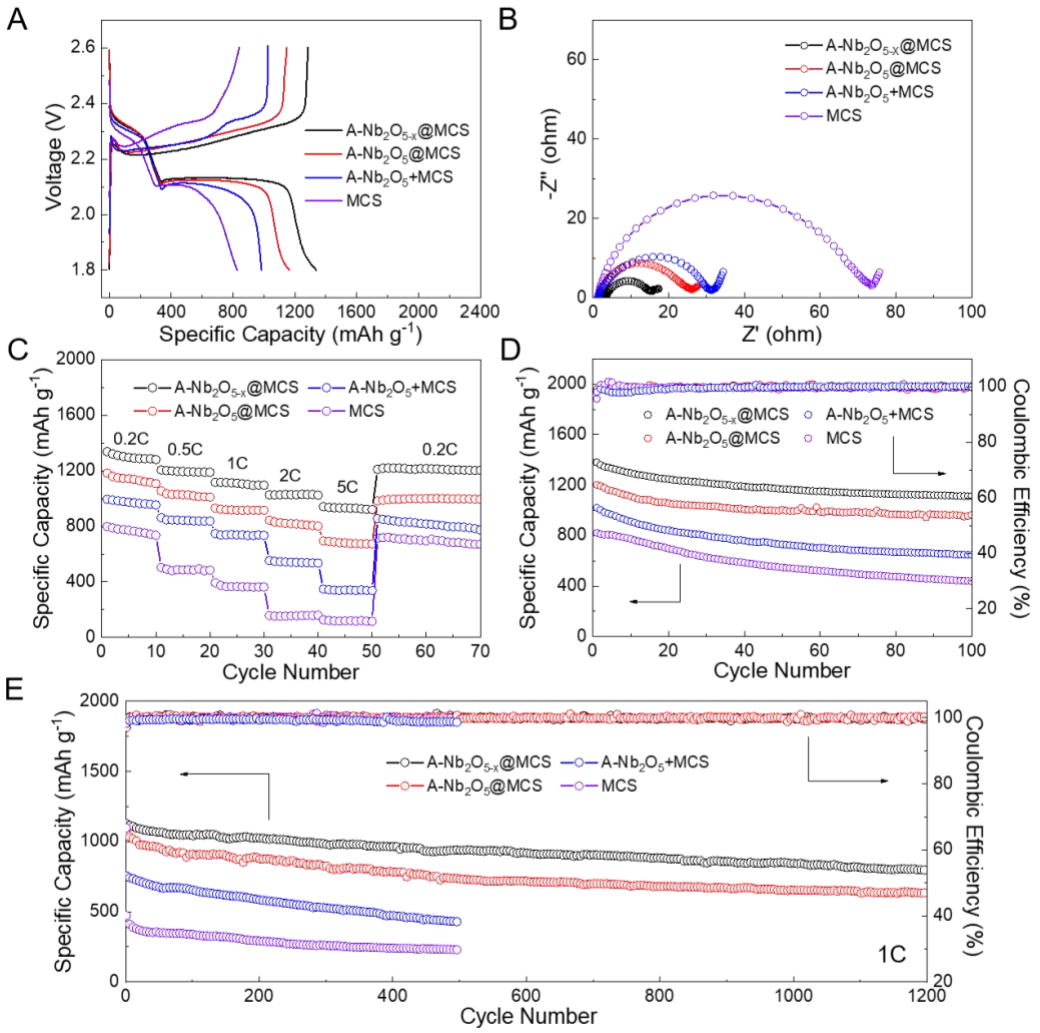

Figure 6.12 Electrochemical performance of A-Nb_2O_{5-x}@MCS, A-Nb_2O_5@MCS, A-Nb_2O_5+MCS and MCS: (A) GCD profiles of 0.2 C, (B) EIS spectra, (C) rate performance, (D) cycling performance under 0.2 C and (E) long-term cycling operation under 1 C.

In view of the demand of high energy density in practical applications, the Li-S performance under raised sulfur loading and low electrolyte/sulfur (E/S) ratio was probed. Clearly, A-Nb_2O_{5-x}@MCS sulfur composites exhibits the best Li-S performance among these materials. Therefore, A-Nb_2O_{5-x}@MCS was selected as sulfur immobilizer to examine its performance under practical relevant operation conditions. Figure 6.13A shows

the GCD profiles of A-Nb_2O_{5-x}@MCS, which still exhibits two distinctive discharge plateaus and a high areal capacity of 6.62 mAh cm^{-2} with a high sulfur loading of ~5.8 mg cm^{-2} and decreased E/S ratio of 4.5 ml g^{-1}. The rate performance evaluation under high sulfur loading shows a decent areal capacity of 4.63 mAh cm^{-2} at 1 C, and 6.18 mAh cm^{-2} when the current density switched back to 0.1 C, indicating the high sulfur utilizations and limited electrochemical polarizations (Figure 6.13B). A stable cycling behavior can be achieved with a high capacity retention of 5.48 mAh cm^{-2} after 200 cycles, as depicted in Figure 6.13C. The extraordinary cyclability is attributed to the favorable LiPS adsorptive and catalytic superiorities of A-Nb_2O_{5-x}@MCS, which serves as multifunctional sulfur immobilizer to stockpile sulfur, suppress LiPS shuttling and promote Li-S electrochemistry for prolonged battery lifespan.

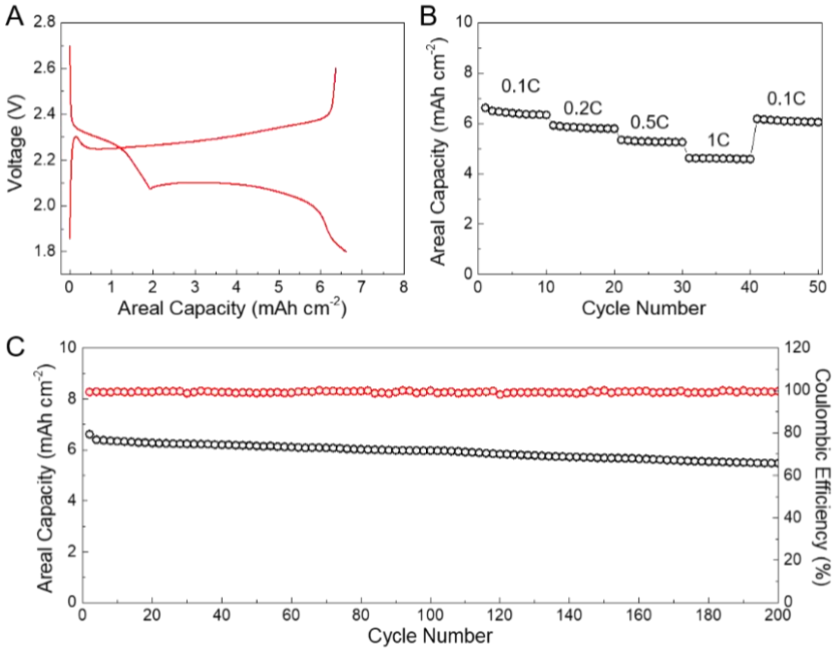

Figure 6.13 (A) GCD profiles at 0.1 C, (B) rate performance and (C) cycling performance of A-Nb_2O_{5-x}@MCS at 0.1 C under raised sulfur loading of 5.8 mg cm^{-2} and decreased E/S ratio of 4.5 ml g^{-1}.

6.7 Conclusions

In summary, we have developed a new method to synthesis ultrafine cobalt based TMCs by porous carbon implantation strategy and identified the universality to synthesis TMOs, like Nb_2O_5, with ultrafine particle size as well as controllable crystallinity and/or defective states. The as-developed ultrafine amorphous oxygen-deficient A-Nb_2O_{5-x}@MCS serves as high-efficiency multifunctional sulfur immobilizer and promoter toward superior LiPS shutting inhibition and catalytic conversion. The amorphous and defective structure strengthens LiPS affinity of Nb_2O_5, while the oxygen defects further enhances the catalytic activity for LiPS conversions. Moreover, the ultra-small NPs embedded composite architecture serves as confining nanoreactor toward homogenized sulfur distribution for enhanced sulfur utilization, conductive framework for expedite electron/ion transfer, and abundant active interfaces for LiPS confinements and conversions, leading to improved electrocatalytic behavior. Attributed to these structural superiorities, the A-Nb_2O_{5-x}@MCS bestows an excellent long-term cycling stability with a low capacity fading of 0.024 % per cycle over 1200 cycles, good rate capability and high areal capacity of 6.62 mAh cm^{-2} under practical relevant conditions. This work provides a new method to develop tertiary interconnected nanoarchitecture embedded with highly dispersive ultrafine NPs for much improved stability and catalytic activity, which enlighten the material engineering in other related areas. Besides, the systematic investigation of this work unveils the structure-performance relationship with a combination of material crystallinity selection, embedded structure creation and defect engineering introduction towards the concurrent fulfillment of highly adsorptive and catalytic sulfur cathode, showing great potential in the development of high-performance Li-S batteries.

Chapter 7 Conclusions and future prospects

7.1 Conclusions

Rechargeable Li-S batteries have attracted tremendous interests due to its ultra-high theoretical energy density and low cost, which are considered as the most promising energy storage systems applied for long-range electric vehicles and military/aviation use. However, the practical application of Li-S batteries still remains many challenges. On the cathode side, the insulating nature of sulfur and its discharge product Li_2S significantly impedes the electron transportation of sulfur cathodes in Li-S batteries. The dissolution and shuttle effect of LiPS lead to poor coulombic efficiency and reduced cycle life of Li-S batteries. Besides, the limited active sites of sulfur host and sluggish conversion kinetics of LiPS results in unsatisfied redox reaction. For the electrolyte, the stability of electrolyte affects the LiPS solubility and the safety of Li-S batteries. Furthermore, lithium metal as anode material raises many challenges to this system, which needs deep understanding in the lithium metal protection and SEI design in future work. This thesis work is mainly focused on the advanced structure design for sulfur cathodes. A series of experimental designs were carried out in this study to fabricate various sulfur immobilizer toward fast and durable Li-S performance. Different physical and electrochemical characterizations were conducted to determine the relationships between structural properties and their electrochemical performance. Furthermore, underlying mechanisms of materials and electrochemical reactions were explored, such as the sulfur confinement enhancement by multi-shelled hollow structure host materials, the enhanced LiPS catalytic conversion on anion defects and amorphous structure; the amplified Li-S performance by employing ultrafine nanoparticle implantation structured material as sulfur immobilizer; the synergistic

engineering of high active sulfur host by manipulating the crystallinity and defective states, etc. In summary, this study focused on sulfur cathodes in Li-S batteries and mainly works on four parts: morphology control, micro-nano structure design, defective engineering and ultrafine nanoparticle implantation. The detailed study gained better understanding in Li-S batteries, and it is believed that these synthesis and analysis bring new sights of Li-S batteries in their applications.

Developing highly adsorptive and catalytic material to endow sulfur cathode with strengthened adsorption and fast conversion reaction of LiPS is inevitable to realize superb rate capability and cyclic stability of Li-S battery. Cobalt based TMOs are widely investigated in electrocatalysis area owing to its high electrochemical stability and simple synthesis process. However, this material is scarcely investigated in Li-S battery area. Developing cobalt based TMOs as sulfur host and understanding its structure-performance relationship is significant to reveal the origin of strong sulfur confinement of TMOs. In Chapter 3, Co_3O_4 was introduced as sulfur host and its sulfur confinement was investigated. The synthetic technique endows the formation of TMOs multishelled hollow microsphere with tunable shell number and composition. The structure evolution of QS-HS microsphere has been revealed via *ex-situ* morphological/structural characterizations and the underlying mechanism is elucidated. This unique structure offers large hollow interior and surface area, which facilities electrolyte infiltration, alleviates volume expansion and homogenizes sulfur distribution within the shell. The porous shell with massive exposed active interfaces shortens ion diffusion pathway and strengthen the adsorption of LiPS, which endows Co_3O_4 QS-HS with fast and durable redox reaction. Besides, this multishelled structure serves as reservoir, which reserves abundant electrolyte inside and offers strong sulfur

confinement to suppress LiPS dissolution and diffusion out of hollow sphere. Attributed to these features, the Co_3O_4 QS-HS sulfur composites deliver the highest discharge capacity of 983.8 mAh g^{-1} and good cycling performance with a capacity retention of 82% after 100 cycles at 1 C comparing other Co_3O_4 hollow spheres with different shell number, indicating its improved sulfur utilization and potent sulfur confinement attributed to multi-shelled structure design. This morphology control engineering is also capable of designing other TMOs with tunable shell number and composition towards desirable electrochemical performance, which also enlighten the material engineering in related field.

To further accelerate the electron conduction and LiPS adsorption, defect engineering strategy was introduced to design oxygen-deficient TMOs porous hollow microsphere for enhanced Li-S performance. In Chapter 4, a facile synthesis method was developed, which is able to produce double shelled Co_3O_4 porous hollow microsphere with enriched cation substitution and anion defects as multifunctional sulfur immobilizer. The porous hollow structure facilitates electrolyte infiltration and exposes more surface area and porosity to homogenize sulfur distribution and stockpile sulfur, rendering improved Li-S electrochemistry. The defect engineering, raised by Ni substitution, induces abundant anion defects on the octahedral sites of spinel Co_3O_4, which serves as adsorption sites for strong LiPS interaction. Besides, the synergistic incorporation of cation and anion defects significantly strengthen the electron conduction, leading to expedite electron transportation within the electrode. Attributed to these features, the as-developed NCO-HS, which act as absorber and promoter, offers strong sulfur immobilization and accelerates sulfur conversion. This sulfur composite delivers higher discharge capacity of 1201 mAh g^{-1}, superb rate capability up to 5 C and outstanding cyclability with a low capacity fading rate

of 0.045% per cycle. This synergistic engineering combing morphology control and defect introduction is able to manipulate the adsorptive and conductive properties of sulfur immobilizer towards strong sulfur trapping and superior redox reaction kinetics for fast and durable Li-S performance.

In addition to oxygen defect, the Li-S kinetics enhancement by other type of anion defects such as sulfur vacancies are also investigated. Co_9S_8 was selected as representative material to reveal the role of sulfur vacancies in strengthening LiPS adsorption and catalytic conversion. In Chapter 5, a new strategy was developed to synthesis 3DOM Co_9S_8 material, which exhibits similar BET surface area and porosity with NCO-HS. The unique 3DOM design provides abundant voids for sulfur storage and enlarged active interfaces that reduce electron/ion diffusion pathways. The ammonia treatment introduces N substitution on the surface of Co_9S_8, which tunes part of CoS_4 tetrahedron into CoS_6 octahedron, leading to the formation of S vacancies on the octahedral sites. The as-developed 3DOM N-Co_9S_{8-x} demonstrates high conductivity, enhanced LiPS adsorbability and conversion kinetics. Benefiting from these features, the as-developed 3DOM N-Co_9S_{8-x}/S cathode delivers high areal capacity, superb rate capability and excellent cyclic stability with ultra-low capacity fading rate under raised sulfur loading and low E/S ratio. These works lays the footstone for the work in Chapter 6.

To further promote the redox reaction, it is critical to expose more active interfaces. In Chapter 6, a unique porous carbon NPs implantation structure was developed, which endows the inlaid Nb_2O_5 NPs with ultrafine particle size with high surface-to-volume ratio. The synergistic engineering encompassing particle size refinement, defect implantation and crystallinity control can further endow the composite material with strong sulfur

confinement, more complete Li_2S transformation and superior LiPS catalytic activity. Thus, a systematic synthesis method was established, in which the particle size and crystallinity can be manipulated by controlling the pore diameter of carbon matrix while the defective states can be regulated by selecting different atmosphere for annealing. A-Nb_2O_{5-x}@MCS was developed to offer superior LiPS shuttle inhibition and conversion catalyzation. The A-Nb_2O_{5-x} nanocluster implanted framework uniformizes sulfur distribution, exposes vast active interfaces and offers reduced ion/electron transportation pathway for expedited redox reaction. Moreover, the low crystallinity feature of A-Nb_2O_{5-x} manipulates the LiPS chemical affinity while the defect chemistry enhances the intrinsic conductivity and catalytic activity for rapid electrochemical conversions. Attributed to these unique superiorities, A-Nb_2O_{5-x}@MCS enables remarkable Li-S battery performances under practical relevant sulfur loading and E/S ratio, holding a great promise in developing practically viable Li-S batteries and enlightening material engineering in related energy storage and conversion areas.

7.2 Future prospects

This thesis has shown great improvement in the cycling life and reaction kinetics of a Li-S battery. These cathodes expand over a wide spectrum of transition metal oxides/sulfides and their composites. The verification and understanding of the chemical interaction of various defective materials with PS by spectroscopic and theoretical studies, the deposition behavior of discharged products, catalytic redox reactions of the sulfur immobilizers comprise the most important contribution of this thesis to the Li-S research community. Excellent cycling behavior over 1500 cycles and superb rate capability have been achieved

in this thesis. We are now on the precipice of the next phase of Li-S research, where new developments must palpably contribute to making the Li-S technology commercially relevant. To take this leap, the Li-S community should recognize the shortcomings in the parameters being used in current cell designs and deliberately move toward those that can fully realize the high-energy density promise of Li-S batteries. Thus, the idea development and performance verification in this thesis are carefully designed to meet the practical application requirement (sulfur loading ≥ 5 mg cm_2, E/S ratio ≤ 5, discharge capacity $\geq$1000 mAh g_{-1}). Although many accomplishments have been achieved in this thesis, there's still some challenges remain in this field. The following are recommendations for future research:

1. Quantitatively analyzing the defects content in sulfur immobilizer and reveal the relationship between defect contents and its performance. Determine the optimal defects content with the admirable catalytic activity and stability to realize fast and durable Li-S performance.
2. Understanding the underlying mechanism of the LiPS adsorption and catalytic effect by synergistic combining defective and amorphous structures. Develop the optimized model for DFT calculation to reveal the LiPS adsorption energy and conversion energy barrier on the amorphous defective surfaces of TMCs.
3. Employing A-Nb_2O_{5-x}@MCS sulfur cathode in pouch cell to examine its cycle life and fast charge-discharge capabilities in cell level. Evaluating the capability and feasibility of A-Nb_2O_{5-x}@MCS for scaling up to realize large scale production.
4. Investigating the anode failure mechanism and develop new electrolyte for Li-S batteries. The past decade has witnessed the rapid development of sulfur cathode

towards superior Li-S performance. However, the SEI accumulation, dead Li formation and dendrite growth on the anode side results in the battery failure in a short period of time. Developing efficient Li metal protection strategy to improve the anode stability can further enhance the Li-S performance. Besides, searching new type of electrolyte which can simultaneously eliminate the LiPS formation and dissolution into electrolyte on the cathode and induce stable SEI formation on the anode is the new direction for Li-S research community in the next decade.

Copyright permissions

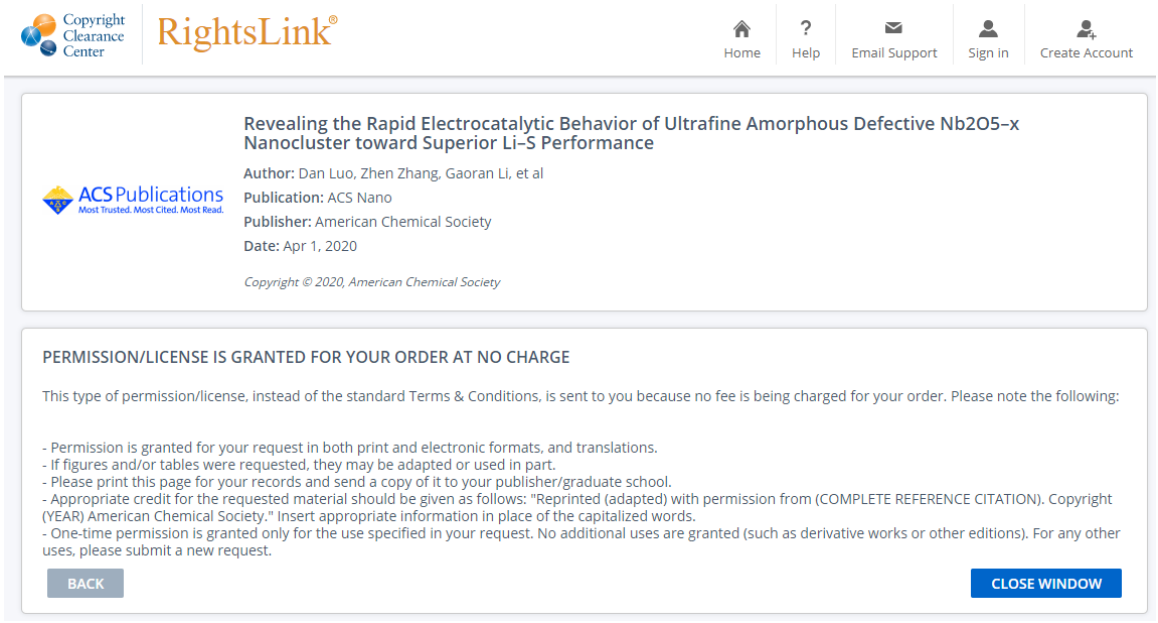

Copyright Clearance Center | RightsLink®

Home | Help | Email Support | Sign in | Create Account

ACS Publications
Most Trusted. Most Cited. Most Read.

Revealing the Rapid Electrocatalytic Behavior of Ultrafine Amorphous Defective Nb2O5–x Nanocluster toward Superior Li–S Performance

Author: Dan Luo, Zhen Zhang, Gaoran Li, et al
Publication: ACS Nano
Publisher: American Chemical Society
Date: Apr 1, 2020

Copyright © 2020, American Chemical Society

PERMISSION/LICENSE IS GRANTED FOR YOUR ORDER AT NO CHARGE

This type of permission/license, instead of the standard Terms & Conditions, is sent to you because no fee is being charged for your order. Please note the following:

- Permission is granted for your request in both print and electronic formats, and translations.
- If figures and/or tables were requested, they may be adapted or used in part.
- Please print this page for your records and send a copy of it to your publisher/graduate school.
- Appropriate credit for the requested material should be given as follows: "Reprinted (adapted) with permission from (COMPLETE REFERENCE CITATION). Copyright (YEAR) American Chemical Society." Insert appropriate information in place of the capitalized words.
- One-time permission is granted only for the use specified in your request. No additional uses are granted (such as derivative works or other editions). For any other uses, please submit a new request.

BACK | CLOSE WINDOW

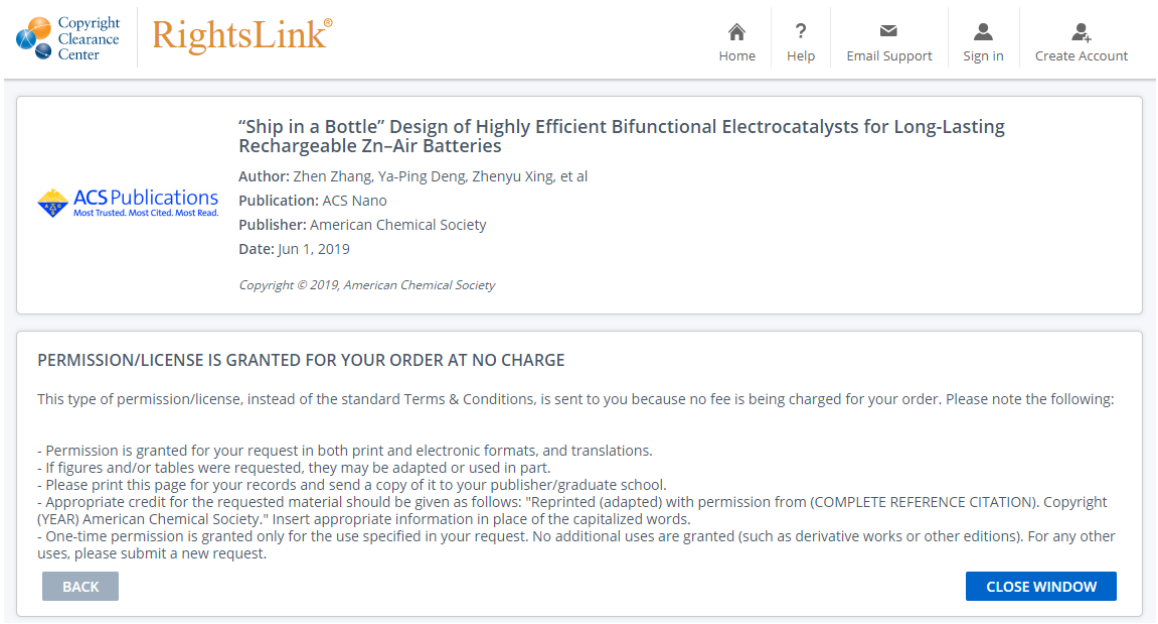

Copyright Clearance Center | RightsLink®

Home | Help | Email Support | Sign in | Create Account

ACS Publications
Most Trusted. Most Cited. Most Read.

"Ship in a Bottle" Design of Highly Efficient Bifunctional Electrocatalysts for Long-Lasting Rechargeable Zn–Air Batteries

Author: Zhen Zhang, Ya-Ping Deng, Zhenyu Xing, et al
Publication: ACS Nano
Publisher: American Chemical Society
Date: Jun 1, 2019

Copyright © 2019, American Chemical Society

PERMISSION/LICENSE IS GRANTED FOR YOUR ORDER AT NO CHARGE

This type of permission/license, instead of the standard Terms & Conditions, is sent to you because no fee is being charged for your order. Please note the following:

- Permission is granted for your request in both print and electronic formats, and translations.
- If figures and/or tables were requested, they may be adapted or used in part.
- Please print this page for your records and send a copy of it to your publisher/graduate school.
- Appropriate credit for the requested material should be given as follows: "Reprinted (adapted) with permission from (COMPLETE REFERENCE CITATION). Copyright (YEAR) American Chemical Society." Insert appropriate information in place of the capitalized words.
- One-time permission is granted only for the use specified in your request. No additional uses are granted (such as derivative works or other editions). For any other uses, please submit a new request.

BACK | CLOSE WINDOW

Copyright Clearance Center | RightsLink®

Home | Help | Email Support | Dan Luo

ACS Publications
Most Trusted. Most Cited. Most Read.

Tuning Shell Numbers of Transition Metal Oxide Hollow Microspheres toward Durable and Superior Lithium Storage

Author: Dan Luo, Ya-Ping Deng, Xiaolei Wang, et al
Publication: ACS Nano
Publisher: American Chemical Society
Date: Nov 1, 2017

PERMISSION/LICENSE IS GRANTED FOR YOUR ORDER AT NO CHARGE

This type of permission/license, instead of the standard Terms & Conditions, is sent to you because no fee is being charged for your order. Please note the following:

- Permission is granted for your request in both print and electronic formats, and translations.
- If figures and/or tables were requested, they may be adapted or used in part.
- Please print this page for your records and send a copy of it to your publisher/graduate school.
- Appropriate credit for the requested material should be given as follows: "Reprinted (adapted) with permission from (COMPLETE REFERENCE CITATION). Copyright (YEAR) American Chemical Society." Insert appropriate information in place of the capitalized words.
- One-time permission is granted only for the use specified in your request. No additional uses are granted (such as derivative works or other editions). For any other uses, please submit a new request.

BACK | CLOSE WINDOW

Copyright Clearance Center | RightsLink®

Home | Help | Email Support | Dan Luo

Synergistic Engineering of Defects and Architecture in Binary Metal Chalcogenide toward Fast and Reliable Lithium–Sulfur Batteries
Author: Zhongwei Chen, Aiping Yu, Wen Lei, et al
Publication: Advanced Energy Materials
Publisher: John Wiley and Sons
Date: Mar 13, 2019

Order Completed

Thank you for your order.

This Agreement between 200 university ave west ("You") and John Wiley and Sons ("John Wiley and Sons") consists of your license details and the terms and conditions provided by John Wiley and Sons and Copyright Clearance Center.

Your confirmation email will contain your order number for future reference.

Printable Details

License Number	4825061202756
License date	May 09, 2020

Licensed Content

Licensed Content Publisher	John Wiley and Sons
Licensed Content Publication	Advanced Energy Materials
Licensed Content Title	Synergistic Engineering of Defects and Architecture in Binary Metal Chalcogenide toward Fast and Reliable Lithium–Sulfur Batteries
Licensed Content Author	Zhongwei Chen, Aiping Yu, Wen Lei, et al
Licensed Content Date	Mar 13, 2019
Licensed Content Volume	9
Licensed Content Issue	18
Licensed Content Pages	10

Order Details

Type of use	Dissertation/Thesis
Requestor type	Author of this Wiley article
Format	Electronic
Portion	Figure/table
Number of figures/tables	1
Will you be translating?	No

About Your Work

Title	Li-S BATTERIES
Institution name	University of waterloo
Expected presentation date	Aug 2020

Additional Data

Portions	Figure 1, 2, 3, 4

Requestor Location

	200 university ave west 904-137 university ave west
Requestor Location	WATERLOO, ON N2L 3E6 Canada Attn: 200 university ave west

Tax Details

Publisher Tax ID	EU826007151

List of publications

- **Luo D**.; Zheng L.; *et al*. Constructing Multifunctional Solid Electrolyte Interface *via in-situ* Polymerization for Dendrite-Free and Low N/P Ratio Lithium Metal Batteries. *Nature Communications*, **2020**, revised.
- **Luo D.**#; Zhang Z.#; *et al.* Revealing the rapid electrocatalytic behavior of ultrafine amorphous defective Nb_2O_{5-x} nanocluster towards superior Li-S performance. *ACS nano*, **2020**, 14, 4849-4860.
- Zhang Z.#; **Luo D.**#; *et al.* Ultrafine amorphous Ta_2O_{5-x} nanoclusters in a pitaya-inspired design kinetically enhancing polysulfide redox reactions for high-performance lithium-sulfur batteries. *Matter*, **2020**, in press. DOI:10.1016/j.matt.2020.06.002.
- Liu G.#; **Luo D**.#; *et al*. A Combined Ordered Macro-Mesoporous Architecture Design and Surface Engineering Strategy for High-Performance Sulfur Immobilizer in Lithium-Sulfur Batteries. *Small*, **2020**, 2001089.
- **Luo D.**#; Li G. R.#; *et al.* Synergistic Engineering of Defects and Architecture in Binary Metal Chalcogenide towards Fast and Reliable Lithium-Sulfur Batteries. *Adv. Energy Mater.*, **2019**, 9, 1900228.
- Zhang Z.#; **Luo D.** #; *et al.* In-situ ion-activated carbon nanospheres with tunable ultramicroporosity for superior CO_2 capture. *Carbon*, **2019**, 143, 531-541.
- **Luo D.**#; Deng Y. P.#; *et al.* Tuning Shell Numbers of Transition Metal Oxide Hollow Microspheres towards Durable and Superior Lithium Storage. *ACS nano*, **2017**, 11, 11521-11530.

- Li G.#; **Luo D.**#; *et al.* Enhanced reversible sodium-ion intercalation by synergistic coupling of few layered MoS_2 and S-doped graphene. *Adv. Funct. Mater.*, **2017**, 27, 1702562.
- Cai W.; Li G.; **Luo D.**; *et al*. The dual-play of 3D conductive scaffold embedded with Co, N co-doped hollow polyhedra toward high-performance Li-S full cell. *Adv. Energy Mater.*, **2018**, 1802561.
- Li G. R.; Lei W.; **Luo D.**; *et al*. Stringed "tube on cube" nanohybrids as compact cathode matrix for high-loading and lean-electrolyte lithium-sulfur batteries. *Energy Environ. Sci.*, **2018**, 11, 2372-2381.
- Li G. R.; Lei W.; **Luo D.**; *et al.* Three-dimensionally porous carbon sheets with multidirectional ion pathways for fast and durable lithium-sulfur batteries. *Adv. Energy Mater.*, **2017**, 1702381.
- Deng Y. P.; Jiang Y.; **Luo D.**; *et al*. Hierarchical Porous Double-Shelled Electrocatalyst with Tailored Lattice Alkalinity toward Bifunctional Oxygen Reactions for Metal-Air Batteries. *ACS Energy Lett.*, **2017**, 2, 2706-2712.

  (#: These authors contributed equally to this work.)

References

1. Halford, B. Lithium-Ion Battery Pioneers Nab 2019 Nobel Prize in Chemistry. https://cen.acs.org/people/nobel-prize/Li-ion-batteries-win-2019-Nobel-Prize-in-Chemistry/97/web/2019/10.

2. Ritchie, A. G.; Giwa, C. O.; Lee, J. C.; Bowles, P.; Gilmour, A.; Allan, J.; Rice, D. A.; Brady, F.; Tsang, S. C. E., Future Cathode Materials for Lithium Rechargeable Batteries. *J Power Sources* 1999, 80, 98-102.

3. Bruce Dunn, H. K., Jean-Marie Tarascon, Electrical Energy Storage for the Grid: A Battery of Choices. *Science* 2011, 334, 928-935.

4. Hwang, J.; Rao, R. R.; Giordano, L.; Katayama, Y.; Yu, Y.; Shao-Horn, Y., Perovskites in Catalysis and Electrocatalysis. *Science* 2017, 358, 751-756.

5. Hassan, F. M.; Batmaz, R.; Li, J.; Wang, X.; Xiao, X.; Yu, A.; Chen, Z., Evidence of Covalent Synergy in Silicon-Sulfur-Graphene Yielding Highly Efficient and Long-Life Lithium-Ion Batteries. *Nat. Commun.* 2015, 6, 8597.

6. Li, M.; Chen, Z.; Wu, T.; Lu, J., Li2 S- or S-Based Lithium-Ion Batteries. *Adv. Mater.* 2018, e1801190.

7. Tang, C.; Li, B.-Q.; Zhang, Q.; Zhu, L.; Wang, H.-F.; Shi, J.-L.; Wei, F., Cao-Templated Growth of Hierarchical Porous Graphene for High-Power Lithium-Sulfur Battery Applications. *Adv. Funct. Mater.* 2016, 26, 577-585.

8. Liang, X.; Hart, C.; Pang, Q.; Garsuch, A.; Weiss, T.; Nazar, L. F., A Highly Efficient Polysulfide Mediator for Lithium-Sulfur Batteries. *Nat. Commun.* 2015, 6, 5682.

9. Luo, D.; Zhang, Z.; Li, G.; Cheng, S.; Li, S.; Li, J.; Gao, R.; Li, M.; Sy, S.; Deng, Y. P.; Jiang, Y.; Zhu, Y.; Dou, H.; Hu, Y.; Yu, A.; Chen, Z., Revealing the Rapid Electrocatalytic Behavior of Ultrafine Amorphous Defective Nb2O5-x Nanocluster toward Superior Li-S Performance. *ACS nano* 2020.

10. Zhang, S. S., Liquid Electrolyte Lithium/Sulfur Battery: Fundamental Chemistry, Problems, and Solutions. *J. Power Sources* 2013, 231, 153-162.

11. Barchasz, C.; Molton, F.; Duboc, C.; Lepretre, J. C.; Patoux, S.; Alloin, F., Lithium/Sulfur Cell Discharge Mechanism: An Original Approach for Intermediate Species Identification. *Anal. Chem.* 2012, 84, 3973-80.

12. Li, G.; Wang, S.; Zhang, Y.; Li, M.; Chen, Z.; Lu, J., Revisiting the Role of Polysulfides in Lithium-Sulfur Batteries. *Adv. Mater.* 2018, 30, 1705590.

13. Cheng, X.-B.; Huang, J.-Q.; Zhang, Q.; Peng, H.-J.; Zhao, M.-Q.; Wei, F., Aligned Carbon Nanotube/Sulfur Composite Cathodes with High Sulfur Content for Lithium–Sulfur Batteries. *Nano Energy* 2014, 4, 65-72.

14. Seh, Z. W.; Yu, J. H.; Li, W.; Hsu, P. C.; Wang, H.; Sun, Y.; Yao, H.; Zhang, Q.; Cui, Y., Two-Dimensional Layered Transition Metal Disulphides for Effective Encapsulation of High-Capacity Lithium Sulphide Cathodes. *Nat. Commun.* 2014, 5, 5017.

15. Xu, R.; Belharouak, I.; Li, J. C. M.; Zhang, X.; Bloom, I.; Bareño, J., Role of Polysulfides in Self-Healing Lithium-Sulfur Batteries. *Adv. Energy Mater.* 2013, 3, 833-838.

16. Gao, X.; Yang, X.; Adair, K.; Li, X.; Liang, J.; Sun, Q.; Zhao, Y.; Li, R.; Sham, T. K.; Sun, X., 3d Vertically Aligned Li Metal Anodes with Ultrahigh Cycling Currents and Capacities of 10 mA cm^{-2}/20 mAh cm^{-2} Realized by Selective Nucleation within Microchannel Walls. *Adv. Energy Mater.* 2020, 1903753.

17. Zhang, S.; Ueno, K.; Dokko, K.; Watanabe, M., Recent Advances in Electrolytes for Lithium-Sulfur Batteries. *Adv. Energy Mater.* 2015, 5, 1500117.

18. Zhang, S. S., Role of Lino3 in Rechargeable Lithium/Sulfur Battery. *Electrochim. Acta* 2012, 70, 344-348.

19. Safari, M.; Kwok, C. Y.; Nazar, L. F., Transport Properties of Polysulfide Species in Lithium-Sulfur Battery Electrolytes: Coupling of Experiment and Theory. *ACS Cent. Sci.* 2016, 2, 560-8.

20. Yuan, H.; Peng, H.-J.; Huang, J.-Q.; Zhang, Q., Sulfur Redox Reactions at Working Interfaces in Lithium-Sulfur Batteries: A Perspective. *Adv. Mater. Interfaces* 2019, 6, 1802046.

21. Zhao, M.; Peng, H. J.; Li, B. Q.; Chen, X.; Xie, J.; Liu, X.; Zhang, Q.; Huang, J. Q., Electrochemical Phase Evolution of Metal-Based Pre-Catalysts for High-Rate Polysulfide Conversion. *Angew. Chem. Int. Ed. Engl.* 2020.

22. Fan, L.; Zhuang, H. L.; Zhang, K.; Cooper, V. R.; Li, Q.; Lu, Y., Chloride-Reinforced Carbon Nanofiber Host as Effective Polysulfide Traps in Lithium-Sulfur Batteries. *Adv. Sci.* 2016, 3, 1600175.

23. Ji, X.; Lee, K. T.; Nazar, L. F., A Highly Ordered Nanostructured Carbon-Sulphur Cathode for Lithium-Sulphur Batteries. *Nat. Mater.* 2009, 8, 500-506.

24. Yang, Y.; Yu, G. H.; Cha, J. J.; Wu, H.; Vosgueritchian, M.; Yao, Y.; Bao, Z. A.; Cui, Y., Improving the Performance of Lithium-Sulfur Batteries by Conductive Polymer Coating. *Acs Nano* 2011, 5, 9187-9193.

25. Kong, L.; Chen, X.; Li, B. Q.; Peng, H. J.; Huang, J. Q.; Xie, J.; Zhang, Q., A Bifunctional Perovskite Promoter for Polysulfide Regulation toward Stable Lithium-Sulfur Batteries. *Adv. Mater.* 2017, 1705219.

26. Yang, Y.; Xu, H.; Wang, S.; Deng, Y.; Qin, X.; Qin, X.; Chen, G., N-Doped Carbon-Coated Hollow Carbon Nanofibers with Interspersed Tio2 for Integrated Separator of Li-S Batteries. *Electrochim. Acta* 2019, 297, 641-649.

27. Dai, C.; Lim, J.-M.; Wang, M.; Hu, L.; Chen, Y.; Chen, Z.; Chen, H.; Bao, S.-J.; Shen, B.; Li, Y.; Henkelman, G.; Xu, M., Honeycomb-Like Spherical Cathode Host Constructed from Hollow Metallic and Polar Co9s8 Tubules for Advanced Lithium-Sulfur Batteries. *Adv. Funct. Mater.* 2018, 1704443.

28. Lin, H.; Yang, L.; Jiang, X.; Li, G.; Zhang, T.; Yao, Q.; Zheng, G. W.; Lee, J. Y., Electrocatalysis of Polysulfide Conversion by Sulfur-Deficient Mos2 Nanoflakes for Lithium–Sulfur Batteries. *Energy Environ. Sci.* 2017, 10, 1476-1486.

29. Lu, Y.; Li, X.; Liang, J.; Hu, L.; Zhu, Y.; Qian, Y., A Simple Melting-Diffusing-Reacting Strategy to Fabricate S/Nis2-C for Lithium-Sulfur Batteries. *Nanoscale* 2016, 8, 17616-17622.

30. Li, G.; Wang, X.; Seo, M. H.; Li, M.; Ma, L.; Yuan, Y.; Wu, T.; Yu, A.; Wang, S.; Lu, J.; Chen, Z., Chemisorption of Polysulfides through Redox Reactions with Organic Molecules for Lithium-Sulfur Batteries. *Nat. Commun.* 2018, 9, 705.

31. Kim, H.; Lee, J.; Ahn, H.; Kim, O.; Park, M. J., Synthesis of Three-Dimensionally Interconnected Sulfur-Rich Polymers for Cathode Materials of High-Rate Lithium-Sulfur Batteries. *Nat. Commun.* 2015, 6, 7278.

32. Wu, Y.; Zhu, X.; Li, P.; Zhang, T.; Li, M.; Deng, J.; Huang, Y.; Ding, P.; Wang, S.; Zhang, R.; Lu, J.; Lu, G.; Li, Y.; Li, Y., Ultradispersed Wxc Nanoparticles Enable Fast Polysulfide Interconversion for High-Performance Li-S Batteries. *Nano Energy* 2019, 59, 636-643.

33. Tao, X.; Wang, J.; Liu, C.; Wang, H.; Yao, H.; Zheng, G.; Seh, Z. W.; Cai, Q.; Li, W.; Zhou, G.; Zu, C.; Cui, Y., Balancing Surface Adsorption and Diffusion of Lithium-Polysulfides on Nonconductive Oxides for Lithium-Sulfur Battery Design. *Nat. Commun.* 2016, 7, 11203.

34. Wang, X.; Li, G.; Li, J.; Zhang, Y.; Wook, A.; Yu, A.; Chen, Z., Structural and Chemical Synergistic Encapsulation of Polysulfides Enables Ultralong-Life Lithium–Sulfur Batteries. *Energy Environ. Sci.* 2016, 9, 2533-2538.

35. Liang, X.; Kwok, C. Y.; Lodi-Marzano, F.; Pang, Q.; Cuisinier, M.; Huang, H.; Hart, C. J.; Houtarde, D.; Kaup, K.; Sommer, H.; Brezesinski, T.; Janek, J.; Nazar, L. F., Tuning Transition Metal Oxide-Sulfur Interactions for Long Life Lithium Sulfur Batteries: The "Goldilocks" Principle. *Adv. Energy Mater.* 2016, 6, 1501636.

36. Niu, X. Q.; Wang, X. L.; Xie, D.; Wang, D. H.; Zhang, Y. D.; Li, Y.; Yu, T.; Tu, J. P., Nickel Hydroxide-Modified Sulfur/Carbon Composite as a High-Performance Cathode Material for Lithium Sulfur Battery. *ACS Appl. Mater. Interfaces* 2015, 7, 16715-22.

37. Wang, Z.; Shen, J.; Liu, J.; Xu, X.; Liu, Z.; Hu, R.; Yang, L.; Feng, Y.; Liu, J.; Shi, Z.; Ouyang, L.; Yu, Y.; Zhu, M., Self-Supported and Flexible Sulfur Cathode Enabled Via Synergistic Confinement for High-Energy-Density Lithium-Sulfur Batteries. *Adv. Mater.* 2019, 31, e1902228.

38. Shen, S.; Xia, X.; Zhong, Y.; Deng, S.; Xie, D.; Liu, B.; Zhang, Y.; Pan, G.; Wang, X.; Tu, J., Implanting Niobium Carbide into Trichoderma Spore Carbon: A New Advanced Host for Sulfur Cathodes. *Adv.Mater.* 2019, 31, e1900009.

39. Yang, C. P.; Yin, Y. X.; Ye, H.; Jiang, K. C.; Zhang, J.; Guo, Y. G., Insight into the Effect of Boron Doping on Sulfur/Carbon Cathode in Lithium-Sulfur Batteries. *ACS Appl. Mater. Interfaces* 2014, 6, 8789-95.

40. Yu, Z.; Liu, M.; Guo, D.; Wang, J.; Chen, X.; Li, J.; Jin, H.; Yang, Z.; Chen, X.; Wang, S., Radially Inwardly Aligned Hierarchical Porous Carbon for Ultra-Long-Life Lithium-Sulfur Batteries. *Angew. Chem. Int. Ed. Engl.* 2020, 59, 6406-6411.

41. Wang, Z.; Dong, Y.; Li, H.; Zhao, Z.; Wu, H. B.; Hao, C.; Liu, S.; Qiu, J.; Lou, X. W., Enhancing Lithium-Sulphur Battery Performance by Strongly Binding the Discharge Products on Amino-Functionalized Reduced Graphene Oxide. *Nat. Commun.* 2014, 5, 5002.

42. Ma, L.; Zhuang, H. L.; Wei, S.; Hendrickson, K. E.; Kim, M. S.; Cohn, G.; Hennig, R. G.; Archer, L. A., Enhanced Li-S Batteries Using Amine-Functionalized Carbon Nanotubes in the Cathode. *ACS nano* 2016, 10, 1050-9.

43. Li, Z.; Li, C.; Ge, X.; Ma, J.; Zhang, Z.; Li, Q.; Wang, C.; Yin, L., Reduced Graphene Oxide Wrapped Mofs-Derived Cobalt-Doped Porous Carbon Polyhedrons as Sulfur Immobilizers as Cathodes for High Performance Lithium Sulfur Batteries. *Nano Energy* 2016, 23, 15-26.

44. Liang, X.; Rangom, Y.; Kwok, C. Y.; Pang, Q.; Nazar, L. F., Interwoven Mxene Nanosheet/Carbon-Nanotube Composites as Li-S Cathode Hosts. *Adv. Mater.* 2017, 29.

45. Li, M.; Du, H.; Kuai, L.; Huang, K.; Xia, Y.; Geng, B., Scalable Dry Production Process of a Superior 3d Net-Like Carbon-Based Iron Oxide Anode Material for Lithium-Ion Batteries. *Angew. Chem. Int. Ed. Engl.* 2017, 56, 12649-12653.

46. Lee, B. J.; Kang, T. H.; Lee, H. Y.; Samdani, J. S.; Jung, Y.; Zhang, C.; Yu, Z.; Xu, G. L.; Cheng, L.; Byun, S.; Lee, Y. M.; Amine, K.; Yu, J. S., Revisiting the Role of Conductivity and Polarity of Host Materials for Long‐Life Lithium–Sulfur Battery. *Adv. Energy Mater.* 2020, 1903934.

47. Ma, D.; Li, Y.; Yang, J.; Mi, H.; Luo, S.; Deng, L.; Yan, C.; Rauf, M.; Zhang, P.; Sun, X.; Ren, X.; Li, J.; Zhang, H., New Strategy for Polysulfide Protection Based on Atomic Layer Deposition of Tio2 onto Ferroelectric-Encapsulated Cathode: Toward Ultrastable Free-Standing Room Temperature Sodium-Sulfur Batteries. *Adv. Funct. Mater.* 2018, 28, 1705537.

48. Iqbal, A.; Ali Ghazi, Z.; Muqsit Khattak, A.; Ahmad, A., Efficient Sulfur Host Based on Nico 2 O 4 Hollow Microtubes for Advanced Li-S Batteries. *J. Solid State Chem.* 2017, 256, 189-195.

49. Li, B. Q.; Zhang, S. Y.; Kong, L.; Peng, H. J.; Zhang, Q., Porphyrin Organic Framework Hollow Spheres and Their Applications in Lithium-Sulfur Batteries. *Adv. Mater.* 2018, 30, e1707483.

50. Liang, X.; Wen, Z.; Liu, Y.; Wang, X.; Zhang, H.; Huang, M. W. L., Preparation and Characterization of Sulfur–Polypyrrole Composites with Controlled Morphology as High Capacity Cathode for Lithium Batteries. *Solid State Ionics* 2011, 192, 347-350.

51. Qiang, S.; Bin, H.; Xiang-qian, Z.; An-hui, L., Engineering of Hollow Core - Shell Interlinked Carbon Spheres for Highly Stable Lithium Sulfur Batteries. *ACS nano* 2015, 9, 8504-8513.

52. Su, Z.; Liu, J.; Li, M.; Zhu, Y.; Qian, S.; Weng, M.; Zheng, J.; Zhong, Y.; Pan, F.; Zhang, S., Defect Engineering in Titanium-Based Oxides for Electrochemical Energy Storage Devices. *Electrochem. Energy Rev.* 2020.

53. Wang, N.; Bai, Z.; Qian, Y.; Yang, J., Double-Walled Sb@Tio2-X Nanotubes as a Superior High-Rate and Ultralong-Lifespan Anode Material for Na-Ion and Li-Ion Batteries. *Adv. Mater.* 2016, 28, 4126-33.

54. Zhao, Z.; Li, G.; Wang, Z.; Feng, M.; Sun, M.; Xue, X.; Liu, R.; Jia, H.; Wang, Z.; Zhang, W.; Li, H.; Chen, Z., Black Batio3 as Multifunctional Sulfur Immobilizer for Superior Lithium Sulfur Batteries. *J. Power Sources* 2019, 434, 226729.

55. Wei, C.; Feng, Z.; Scherer, G. G.; Barber, J.; Shao-Horn, Y.; Xu, Z. J., Cations in Octahedral Sites: A Descriptor for Oxygen Electrocatalysis on Transition-Metal Spinels. *Adv. Mater.* 2017, 29.

56. Smith, R. D. L.; Pasquini, C.; Loos, S.; Chernev, P.; Klingan, K.; Kubella, P.; Mohammadi, M. R.; González-Flores, D.; Dau, H., Geometric Distortions in Nickel (Oxy)Hydroxide Electrocatalysts by Redox Inactive Iron Ions. *Energy Environ. Sci.* 2018, 11, 2476-2485.

57. Xu, L.; Zhao, H.; Sun, M.; Huang, B.; Wang, J.; Xia, J.; Li, N.; Yin, D.; Luo, M.; Luo, F.; Du, Y.; Yan, C., Oxygen Vacancies on Layered Niobic Acid That Weaken the Catalytic Conversion of Polysulfides in Lithium-Sulfur Batteries. *Angew. Chem. Int. Ed. Engl.* 2019, 58, 11491-11496.

58. Liu, G.; Li, J.; Fu, J.; Jiang, G.; Lui, G.; Luo, D.; Deng, Y. P.; Zhang, J.; Cano, Z. P.; Yu, A.; Su, D.; Bai, Z.; Yang, L.; Chen, Z., An Oxygen-Vacancy-Rich Semiconductor-Supported Bifunctional Catalyst for Efficient and Stable Zinc-Air Batteries. *Adv. Mater.* 2019, 31, e1806761.

59. Huang, L.; Chen, R.; Xie, C.; Chen, C.; Wang, Y.; Zeng, Y.; Chen, D.; Wang, S., Rapid Cationic Defect and Anion Dual-Regulated Layered Double Hydroxides for Efficient Water Oxidation. *Nanoscale* 2018, 10, 13638-13644.

60. Zhang, Y.; Guo, L.; Tao, L.; Lu, Y.; Wang, S., Defect‐Based Single‐Atom Electrocatalysts. *Small Methods* 2018, 3, 1800406.

61. Yan, D.; Li, Y.; Huo, J.; Chen, R.; Dai, L.; Wang, S., Defect Chemistry of Nonprecious-Metal Electrocatalysts for Oxygen Reactions. *Adv. Mater.* 2017.

62. Wang, Q.; Lei, Y.; Wang, D.; Li, Y., Defect Engineering in Earth-Abundant Electrocatalysts for Co2 and N2 Reduction. *Energy Environ. Sci.* 2019, 12, 1730-1750.

63. Wang, Y.; Zhang, R.; Chen, J.; Wu, H.; Lu, S.; Wang, K.; Li, H.; Harris, C. J.; Xi, K.; Kumar, R. V.; Ding, S., Enhancing Catalytic Activity of Titanium Oxide in Lithium–Sulfur Batteries by Band Engineering. *Adv. Energy Mater.* 2019, 9, 1900953.

64. Liu, D.; Wang, C.; Yu, Y.; Zhao, B.-H.; Wang, W.; Du, Y.; Zhang, B., Understanding the Nature of Ammonia Treatment to Synthesize Oxygen Vacancy-Enriched Transition Metal Oxides. *Chem* 2019, 5, 376-389.

65. Li, H.; Tsai, C.; Koh, A. L.; Cai, L.; Contryman, A. W.; Fragapane, A. H.; Zhao, J.; Han, H. S.; Manoharan, H. C.; Abild-Pedersen, F.; Norskov, J. K.; Zheng, X., Corrigendum: Activating and Optimizing Mos2 Basal Planes for Hydrogen Evolution through the Formation of Strained Sulphur Vacancies. *Nat. Mater.* 2016, 15, 364.

66. Zhou, D.; Xiong, X.; Cai, Z.; Han, N.; Jia, Y.; Xie, Q.; Duan, X.; Xie, T.; Zheng, X.; Sun, X.; Duan, X., Flame-Engraved Nickel-Iron Layered Double Hydroxide Nanosheets for Boosting Oxygen Evolution Reactivity. *Small Methods* 2018, 2, 1800083.

67. Kim, H. S.; Cook, J. B.; Lin, H.; Ko, J. S.; Tolbert, S. H.; Ozolins, V.; Dunn, B., Oxygen Vacancies Enhance Pseudocapacitive Charge Storage Properties of Moo3-X. *Nat. Mater.* 2017, 16, 454-460.

68. Dou, S.; Tao, L.; Wang, R.; El Hankari, S.; Chen, R.; Wang, S., Plasma-Assisted Synthesis and Surface Modification of Electrode Materials for Renewable Energy. *Adv. Mater.* 2018, 30, e1705850.

69. Chen, D.; Qiao, M.; Lu, Y. R.; Hao, L.; Liu, D.; Dong, C. L.; Li, Y.; Wang, S., Preferential Cation Vacancies in Perovskite Hydroxide for the Oxygen Evolution Reaction. *Angew. Chem. Int. Ed. Engl.* 2018, 57, 8691-8696.

70. Zhang, C.; Shi, Y.; Yu, Y.; Du, Y.; Zhang, B., Engineering Sulfur Defects, Atomic Thickness, and Porous Structures into Cobalt Sulfide Nanosheets for Efficient Electrocatalytic Alkaline Hydrogen Evolution. *ACS Catal.* 2018, 8, 8077-8083.

71. Zhao, M.; Peng, H. J.; Zhang, Z. W.; Li, B. Q.; Chen, X.; Xie, J.; Chen, X.; Wei, J. Y.; Zhang, Q.; Huang, J. Q., Activating Inert Metallic Compounds for High-Rate Lithium-Sulfur Batteries through in-Situ Etching of Extrinsic Metal. *Angew. Chem. Int. Ed. Engl.* 2018.

72. Du, Z.; Chen, X.; Hu, W.; Chuang, C.; Xie, S.; Hu, A.; Yan, W.; Kong, X.; Wu, X.; Ji, H.; Wan, L. J., Cobalt in Nitrogen-Doped Graphene as Single-Atom Catalyst for High-Sulfur Content Lithium-Sulfur Batteries. *J. Am. Chem. Soc.* 2019, 141, 3977-3985.

73. Shi, P.; Cheng, X. B.; Li, T.; Zhang, R.; Liu, H.; Yan, C.; Zhang, X. Q.; Huang, J. Q.; Zhang, Q., Electrochemical Diagram of an Ultrathin Lithium Metal Anode in Pouch Cells. *Adv. Mater.* 2019, 31, e1902785.

74. Smith, A. J.; Burns, J. C.; Zhao, X.; Xiong, D.; Dahn, J. R., A High Precision Coulometry Study of the Sei Growth in Li/Graphite Cells. *J. Electrochem. Soc.* 2011, 158, A447.

75. Zhang, X.-Q.; Cheng, X.-B.; Zhang, Q., Advances in Interfaces between Li Metal Anode and Electrolyte. *Adv. Mater.Interfaces* 2018, 5, 1701097.

76. Lin, D.; Liu, Y.; Cui, Y., Reviving the Lithium Metal Anode for High-Energy Batteries. *Nat. Nanotechnol.* 2017, 12, 194-206.

77. Wang, S. H.; Yue, J.; Dong, W.; Zuo, T. T.; Li, J. Y.; Liu, X.; Zhang, X. D.; Liu, L.; Shi, J. L.; Yin, Y. X.; Guo, Y. G., Tuning Wettability of Molten Lithium Via a Chemical Strategy for Lithium Metal Anodes. *Nat. Commun.* 2019, 10, 4930.

78. Yu, L.; Chen, S.; Lee, H.; Zhang, L.; Engelhard, M. H.; Li, Q.; Jiao, S.; Liu, J.; Xu, W.; Zhang, J.-G., A Localized High-Concentration Electrolyte with Optimized Solvents and Lithium Difluoro(Oxalate)Borate Additive for Stable Lithium Metal Batteries. *ACS Energy Lett.* 2018, 3, 2059-2067.

79. Pan, H.; Han, K. S.; Engelhard, M. H.; Cao, R.; Chen, J.; Zhang, J.-G.; Mueller, K. T.; Shao, Y.; Liu, J., Addressing Passivation in Lithium-Sulfur Battery under Lean Electrolyte Condition. *Adv. Funct. Mater.* 2018, 28, 1707234.

80. Jaumaux, P.; Liu, Q.; Zhou, D.; Xu, X.; Wang, T.; Wang, Y.; Kang, F.; Li, B.; Wang, G., Deep-Eutectic-Solvent-Based Self-Healing Polymer Electrolyte for Safe and Long-Life Lithium-Metal Batteries. *Angew. Chem. Int. Ed. Engl.* 2020.

81. Bai, S.; Liu, X.; Zhu, K.; Wu, S.; Zhou, H., Metal–Organic Framework-Based Separator for Lithium–Sulfur Batteries. *Nat. Energy* 2016, 1, 16094.

82. Ghazi, Z. A.; He, X.; Khattak, A. M.; Khan, N. A.; Liang, B.; Iqbal, A.; Wang, J.; Sin, H.; Li, L.; Tang, Z., Mos2 /Celgard Separator as Efficient Polysulfide Barrier for Long-Life Lithium-Sulfur Batteries. *Adv. Mater.* 2017, 29.

83. Xiang, Y.; Li, J.; Lei, J.; Liu, D.; Xie, Z.; Qu, D.; Li, K.; Deng, T.; Tang, H., Advanced Separators for Lithium-Ion and Lithium-Sulfur Batteries: A Review of Recent Progress. *ChemSusChem* 2016, 9, 3023-3039.

84. Zhao, T.; Ye, Y.; Peng, X.; Divitini, G.; Kim, H.-K.; Lao, C.-Y.; Coxon, P. R.; Xi, K.; Liu, Y.; Ducati, C.; Chen, R.; Kumar, R. V., Advanced Lithium-Sulfur Batteries Enabled by a Bio-Inspired Polysulfide Adsorptive Brush. *Adv. Funct. Mater.* 2016, 26, 8418-8426.

85. Kim, J. H.; Jung, G. Y.; Lee, Y. H.; Kim, J. H.; Lee, S. Y.; Kwak, S. K.; Lee, S. Y., Polysulfide-Breathing/Dual-Conductive, Heterolayered Battery Separator Membranes Based on 0d/1d Mingled Nanomaterial Composite Mats. *Nano letters* 2017, 17, 2220-2228.

86. Pei, F.; Lin, L.; Fu, A.; Mo, S.; Ou, D.; Fang, X.; Zheng, N., A Two-Dimensional Porous Carbon-Modified Separator for High-Energy-Density Li-S Batteries. *Joule* 2018, 2, 323-336.

87. Bonnick, P.; Nagai, E.; Muldoon, J., Perspective—Lithium-Sulfur Batteries. *J. Electrochem. Soc.* 2017, 165, A6005-A6007.

88. Dörfler, S.; Althues, H.; Härtel, P.; Abendroth, T.; Schumm, B.; Kaskel, S., Challenges and Key Parameters of Lithium-Sulfur Batteries on Pouch Cell Level. *Joule* 2020, 4, 539-554.

89. Kaiser, M. R.; Chou, S.; Liu, H. K.; Dou, S. X.; Wang, C.; Wang, J., Structure-Property Relationships of Organic Electrolytes and Their Effects on Li/S Battery Performance. *Adv. Mater.* 2017, 29.

90. Zhou, W.; Wang, C.; Zhang, Q.; Abruña, H. D.; He, Y.; Wang, J.; Mao, S. X.; Xiao, X., Tailoring Pore Size of Nitrogen-Doped Hollow Carbon Nanospheres for Confining Sulfur in Lithium-Sulfur Batteries. *Adv. Energy Mater.* 2015, 5, 1401752.

91. Guan, B. Y.; Kushima, A.; Yu, L.; Li, S.; Li, J.; Lou, X. W. D., Coordination Polymers Derived General Synthesis of Multishelled Mixed Metal-Oxide Particles for Hybrid Supercapacitors. *Adv. Mater.* 2017, 29, 1605902.

92. Yoshio Idota, T. K., Akihiro Matsufuji, Yukio Maekawa, Tsutomu Miyasaka, Tin Based Amorphous Oxide: A High-Capacity Lithium-Ion-Storage Material. *Science* 1997, 276, 1395-1397.

93. Zhao, Y.; Li, X.; Yan, B.; Xiong, D.; Li, D.; Lawes, S.; Sun, X., Recent Developments and Understanding of Novel Mixed Transition-Metal Oxides as Anodes in Lithium Ion Batteries. *Adv. Energy Mater.* 2016, 6, 1502175.

94. Yang, X.; Shi, K.; Zhitomirsky, I.; Cranston, E. D., Cellulose Nanocrystal Aerogels as Universal 3d Lightweight Substrates for Supercapacitor Materials. *Adv. Mater.* 2015, 27, 6104-9.

95. Wang, J.; Yang, N.; Tang, H.; Dong, Z.; Jin, Q.; Yang, M.; Kisailus, D.; Zhao, H.; Tang, Z.; Wang, D., Accurate Control of Multishelled Co3o4 Hollow Microspheres as High-Performance Anode Materials in Lithium-Ion Batteries. *Angew. Chem. Int. Ed. Engl.* 2013, 52, 6417-20.

96. Hu;, L.; Peng;, Q.; Li, a. Y., Selective Synthesis of Co3o4 Nanocrystal with Different Shape and Crystal Plane Effect on Catalytic Property for Methane Combustion. *J. Am. Chem. Soc.* 2008, 16136-16137.

97. Naichao Li, C. J. P., Guangli Che, and Charles R. Martin, Rate Capabilities of Nanostructured Limn2o4 Electrodes in Aqueous Electrolyte. *Journal of the Electrochemical Chemistry* 2000, 147, 2044-2049.

98. Deng, D. R.; Xue, F.; Jia, Y. J.; Ye, J. C.; Bai, C. D.; Zheng, M. S.; Dong, Q. F., Co4n Nanosheet Assembled Mesoporous Sphere as a Matrix for Ultrahigh Sulfur Content Lithium-Sulfur Batteries. *ACS nano* 2017, 11, 6031-6039.

99. Cheng, H.; Wang, S.; Tao, D.; Wang, M., Sulfur/Co3o4 Nanotube Composite with High Performances as Cathode Materials for Lithium Sulfur Batteries. *Funct. Mater. Lett.* 2014, 07, 1450020.

100. Zhang, G.; Lou, X. W., General Synthesis of Multi-Shelled Mixed Metal Oxide Hollow Spheres with Superior Lithium Storage Properties. *Angewandte Chemie* 2014, 53, 9041-4.

101. Jiang, J.; Li, Y.; Liu, J.; Huang, X.; Yuan, C.; Lou, X. W., Recent Advances in Metal Oxide-Based Electrode Architecture Design for Electrochemical Energy Storage. *Adv. Mater.* 2012, 24, 5166-80.

102. Liang, J.; Yu, X. Y.; Zhou, H.; Wu, H. B.; Ding, S.; Lou, X. W., Bowl-Like Sno2 @Carbon Hollow Particles as an Advanced Anode Material for Lithium-Ion Batteries. *Angewandte Chemie* 2014, 53, 12803-7.

103. Zhou, W.; Yu, Y.; Chen, H.; DiSalvo, F. J.; Abruna, H. D., Yolk-Shell Structure of Polyaniline-Coated Sulfur for Lithium-Sulfur Batteries. *J. Am. Chem. Soc.* 2013, 135, 16736-43.

104. Dong, Z.; Lai, X.; Halpert, J. E.; Yang, N.; Yi, L.; Zhai, J.; Wang, D.; Tang, Z.; Jiang, L., Accurate Control of Multishelled Zno Hollow Microspheres for Dye-Sensitized Solar Cells with High Efficiency. *Adv. Mater.* 2012, 24, 1046-9.

105. Dong, Z.; Ren, H.; Hessel, C. M.; Wang, J.; Yu, R.; Jin, Q.; Yang, M.; Hu, Z.; Chen, Y.; Tang, Z.; Zhao, H.; Wang, D., Quintuple-Shelled Sno2 Hollow Microspheres with Superior Light Scattering for High-Performance Dye-Sensitized Solar Cells. *Adv. Mater.* 2014, 26, 905-9.

106. Li, X.; Jiang, L.; Zhou, C.; Liu, J.; Zeng, H., Integrating Large Specific Surface Area and High Conductivity in Hydrogenated Nico2o4 Double-Shell Hollow Spheres to Improve Supercapacitors. *NPG Asia Mater.* 2015, 7, e165.

107. Wang, J.; Tang, H.; Ren, H.; Yu, R.; Qi, J.; Mao, D.; Zhao, H.; Wang, D., Ph-Regulated Synthesis of Multi-Shelled Manganese Oxide Hollow Microspheres as Supercapacitor Electrodes Using Carbonaceous Microspheres as Templates. *Adv. Sci. (Weinh)* 2014, 1, 1400011.

108. Xu, S.; Hessel, C. M.; Ren, H.; Yu, R.; Jin, Q.; Yang, M.; Zhao, H.; Wang, D., A-Fe2o3multi-Shelled Hollow Microspheres for Lithium Ion Battery Anodes with Superior Capacity and Charge Retention. *Energy Environ. Sci.* 2014, 7, 632-637.

109. Xu, H.; Wang, W., Template Synthesis of Multishelled Cu2o Hollow Spheres with a Single-Crystalline Shell Wall. *Angewandte Chemie* 2007, 46, 1489-92.

110. Zhang, G.; Yu, L.; Wu, H. B.; Hoster, H. E.; Lou, X. W., Formation of Znmn2o4 Ball-in-Ball Hollow Microspheres as a High-Performance Anode for Lithium-Ion Batteries. *Adv. Mater.* 2012, 24, 4609-13.

111. Qi, X.; Zheng, W.; He, G.; Tian, T.; Du, N.; Wang, L., Nico2o4 Hollow Microspheres with Tunable Numbers and Thickness of Shell for Supercapacitors. *Chem. Eng. J.* 2017, 309, 426-434.

112. Guo, J.; Yin, Z.; Zang, X.; Dai, Z.; Zhang, Y.; Huang, W.; Dong, X., Facile One-Pot Synthesis of Nico2o4 Hollow Spheres with Controllable Number of Shells for High-Performance Supercapacitors. *Nano Res.* 2017, 10, 405-414.

113. Pang, Q.; Kundu, D.; Nazar, L. F., A Graphene-Like Metallic Cathode Host for Long-Life and High-Loading Lithium–Sulfur Batteries. *Mater. Horiz.* 2016, 3, 130-136.

114. Nie, Z.; Wang, Y.; Zhang, Y.; Pan, A., Multi-Shelled A-Fe2o3 Microspheres for High-Rate Supercapacitors. *Science China Materials* 2016, 59, 247-253.

115. Sun, X.; Liu, J.; Li, Y., Use of Carbonaceous Polysaccharide Microspheres as Templates for Fabricating Metal Oxide Hollow Spheres. *Chem. Eur. J* 2006, 12, 2039-47.

116. Luo, D.; Zhitomirsky, I., Electrophoretic Deposition of Polyetheretherketone Composites, Containing Huntite and Alumina Platelets. *J. Electrochem. Soc.* 2015, 162, D3057-D3062.

117. Luo, D.; Zhang, T.; Zhitomirsky, I., Electrophoretic Deposition of Tannic Acid-Polypyrrolidone Films and Composites. *J. Colloid Inter. Sci.* 2016, 469, 177-83.

118. Ren, Y.; Ma, Z.; Bruce, P. G., Ordered Mesoporous Nicomno4: Synthesis and Application in Energy Storage and Catalytic Decomposition of N2o. *J. Mater. Chem.* 2012, 22, 15121.

119. Massignan, D. B. a. C., Composition and Microstructure of Cobalt Oxide Thin Films Obtained from a Novel Cobalt(Ii) Precursor by Chemical Vapor Deposition. *Chem. Mater.* 2001, 13, 588-593.

120. Chagas, C. A.; de Souza, E. F.; de Carvalho, M. C. N. A.; Martins, R. L.; Schmal, M., Cobalt Ferrite Nanoparticles for the Preferential Oxidation of Co. *Applied Catalysis A: General* 2016, 519, 139-145.

121. zhong-shuai Wu, W. R., Lei Wen, Libo Gao, Jinping Zhao, Zongping Chen, Guangmin Zhou, Feng Li, and Hui-ming Cheng, Graphene Anchored with Co3o4 Nanoparticles as Anode of Lithium Ion Batteries with Enhanced Reversible Capacity and Cyclic Performance. *ACS nano* 2010, 4, 3187-3194.

122. Ma, Z.; Yuan, X.; Li, L.; Ma, Z.-F.; Zhang, L.; Mai, L.; Zhang, J., Porous Ni0.14mn0.86o1.43 Hollow Microspheres as High-Performing Anodes for Lithium-Ion Batteries. *J. Power Sources* 2015, 291, 156-162.

123. Shen, L.; Yu, L.; Yu, X. Y.; Zhang, X.; Lou, X. W., Self-Templated Formation of Uniform Nico2o4 Hollow Spheres with Complex Interior Structures for Lithium-Ion Batteries and Supercapacitors. *Angew. Chem. Int. Ed. Engl.* 2015, 54, 1868-72.

124. Wang, J.; Tang, H.; Zhang, L.; Ren, H.; Yu, R.; Jin, Q.; Qi, J.; Mao, D.; Yang, M.; Wang, Y.; Liu, P.; Zhang, Y.; Wen, Y.; Gu, L.; Ma, G.; Su, Z.; Tang, Z.; Zhao, H.; Wang, D., Multi-Shelled Metal Oxides Prepared Via an Anion-Adsorption Mechanism for Lithium-Ion Batteries. *Nat. Energy* 2016, 1, 16050.

125. P.Nkeng, J.-F. K., J.L.Gautier, P.Chartier, G.Poillerat, Enhancement of Surface Areas of Co3o4 and Nico204 Electrocatalysts Prepared by Spray Pyrolysis *J. Electroalytical Chem.* 1996, 402, 81-89.

126. Wang, K.; Wu, X.; Wu, W.; Hu, Y.; Liao, S., Synthesis of Spinel Mnco2o4 by Thermal Decomposition of Carbonates and Kinetics of Thermal Decomposition of Precursor. *J. Superconduct. Nov. Magn.* 2013, 27, 1249-1256.

127. Wang, X.; Li, G.; Hassan, F. M.; Li, J.; Fan, X.; Batmaz, R.; Xiao, X.; Chen, Z., Sulfur Covalently Bonded Graphene with Large Capacity and High Rate for High-Performance Sodium-Ion Batteries Anodes. *Nano Energy* 2015, 15, 746-754.

128. Sun, J.; Lv, C.; Lv, F.; Chen, S.; Li, D.; Guo, Z.; Han, W.; Yang, D.; Guo, S., Tuning the Shell Number of Multishelled Metal Oxide Hollow Fibers for Optimized Lithium-Ion Storage. *ACS Nano* 2017, 11, 6186-6193.

129. Li, M.; Zhang, Y.; Bai, Z.; Liu, W. W.; Liu, T.; Gim, J.; Jiang, G.; Yuan, Y.; Luo, D.; Feng, K.; Yassar, R. S.; Wang, X.; Chen, Z.; Lu, J., A Lithium-Sulfur Battery Using a 2d Current Collector Architecture with a Large-Sized Sulfur Host Operated under High Areal Loading and Low E/S Ratio. *Adv. Mater.* 2018, 30, e1804271.

130. Titirici, M. M.; Antonietti, M.; Thomas, A., A Generalized Synthesis of Metal Oxide Hollow Spheres Using a Hydrothermal Approach. *Chem. Mater.* 2006, 18, 3808-3812.

131. Luo, D.; Deng, Y. P.; Wang, X.; Li, G.; Wu, J.; Fu, J.; Lei, W.; Liang, R.; Liu, Y.; Ding, Y.; Yu, A.; Chen, Z., Tuning Shell Numbers of Transition Metal Oxide Hollow

Microspheres toward Durable and Superior Lithium Storage. *ACS nano* 2017, 11, 11521-11530.

132. Iberi, V.; Vlassiouk, I.; Zhang, X. G.; Matola, B.; Linn, A.; Joy, D. C.; Rondinone, A. J., Maskless Lithography and in Situ Visualization of Conductivity of Graphene Using Helium Ion Microscopy. *Sci. Rep.* 2015, 5, 11952.

133. Emmrich, D.; Beyer, A.; Nadzeyka, A.; Bauerdick, S.; Meyer, J. C.; Kotakoski, J.; Gölzhäuser, A., Nanopore Fabrication and Characterization by Helium Ion Microscopy. *Appl. Phys. Lett.* 2016, 108, 163103.

134. Ren, Y.; Ma, Z.; Bruce, P. G., Ordered Mesoporous Metal Oxides: Synthesis and Applications. *Chem. Soc. Rev.* 2012, 41, 4909-27.

135. Yao, X.; Ke, Y.; Ren, W.; Wang, X.; Xiong, F.; Yang, W.; Qin, M.; Li, Q.; Mai, L., Defect‐Rich Soft Carbon Porous Nanosheets for Fast and High‐Capacity Sodium‐Ion Storage. *Adv. Energy Mater.* 2018, 1803260.

136. Tong, X.; Xia, X.; Guo, C.; Zhang, Y.; Tu, J.; Fan, H. J.; Guo, X.-Y., Efficient Oxygen Reduction Reaction Using Mesoporous Ni-Doped Co3o4 Nanowire Array Electrocatalysts. *J. Mater. Chem. A* 2015, 3, 18372-18379.

137. McNulty, D.; Geaney, H.; O'Dwyer, C., Carbon-Coated Honeycomb Ni-Mn-Co-O Inverse Opal: A High Capacity Ternary Transition Metal Oxide Anode for Li-Ion Batteries. *Sci. Rep.* 2017, 7, 42263.

138. Li, G.; Lei, W.; Luo, D.; Deng, Y.; Deng, Z.; Wang, D.; Yu, A.; Chen, Z., Stringed "Tube on Cube" Nanohybrids as Compact Cathode Matrix for High-Loading and Lean-Electrolyte Lithium–Sulfur Batteries. *Energy Environ. Sci.* 2018, 11, 2372-2381.

139. Xu, L.; Jiang, Q.; Xiao, Z.; Li, X.; Huo, J.; Wang, S.; Dai, L., Plasma-Engraved Co3 O4 Nanosheets with Oxygen Vacancies and High Surface Area for the Oxygen Evolution Reaction. *Angew. Chem. Int. Ed. Engl.* 2016, 55, 5277-81.

140. Yuan, C.; Li, J.; Hou, L.; Zhang, X.; Shen, L.; Lou, X. W. D., Ultrathin Mesoporous Nico2o4nanosheets Supported on Ni Foam as Advanced Electrodes for Supercapacitors. *Adv. Funct. Mater.* 2012, 22, 4592-4597.

141. Gao, R.; Li, Z.; Zhang, X.; Zhang, J.; Hu, Z.; Liu, X., Carbon-Dotted Defective Coo with Oxygen Vacancies: A Synergetic Design of Bifunctional Cathode Catalyst for Li–O2 Batteries. *ACS Catal.* 2015, 6, 400-406.

142. Choudhury, T.; Saied, S. O.; Sullivan, J. L.; Abbot, A. M., Reduction of Oxides of Iron, Cobalt, Titanium and Niobium by Low-Energy Ion-Bombardment. *J. Phys. D: Appl. Phys.* 1989, 22, 1185-1195.

143. Ju, Z.; Ma, G.; Zhao, Y.; Xing, Z.; Qiang, Y.; Qian, Y., A Facile Method for Synthesis of Porous Nico2o4nanorods as a High-Performance Anode Material for Li-Ion Batteries. *Part. Part. Syst. Charact.* 2015, 32, 1012-1019.

144. Luo, K.; Roberts, M. R.; Guerrini, N.; Tapia-Ruiz, N.; Hao, R.; Massel, F.; Pickup, D. M.; Ramos, S.; Liu, Y. S.; Guo, J.; Chadwick, A. V.; Duda, L. C.; Bruce, P. G., Anion Redox Chemistry in the Cobalt Free 3d Transition Metal Oxide Intercalation Electrode Li[Li0.2ni0.2mn0.6]O2. *J. Am. Chem. Soc.* 2016, 138, 11211-8.

145. Suntivich, J.; Hong, W. T.; Lee, Y.-L.; Rondinelli, J. M.; Yang, W.; Goodenough, J. B.; Dabrowski, B.; Freeland, J. W.; Shao-Horn, Y., Estimating Hybridization of Transition Metal and Oxygen States in Perovskites from O K-Edge X-Ray Absorption Spectroscopy. *J. Phys. Chem. C* 2014, 118, 1856-1863.

146. Fu, J.; Hassan, F. M.; Zhong, C.; Lu, J.; Liu, H.; Yu, A.; Chen, Z., Defect Engineering of Chalcogen-Tailored Oxygen Electrocatalysts for Rechargeable Quasi-Solid-State Zinc-Air Batteries. *Adv. Mater.* 2017, 29.

147. Wang, Z. L.; Yin, J. S.; Jiang, Y. D., Eels Analysis of Cation Valence States and Oxygen Vacancies in Magnetic Oxides. *Micron* 2000, 31, 571-580.

148. Zhang, Y.; Mu, Z.; Yang, C.; Xu, Z.; Zhang, S.; Zhang, X.; Li, Y.; Lai, J.; Sun, Z.; Yang, Y.; Chao, Y.; Li, C.; Ge, X.; Yang, W.; Guo, S., Rational Design of Mxene/1t-2h Mos2-C Nanohybrids for High-Performance Lithium-Sulfur Batteries. *Adv. Funct. Mater.* 2018, 1707578.

149. Wang, Y.; Zhou, T.; Jiang, K.; Da, P.; Peng, Z.; Tang, J.; Kong, B.; Cai, W.-B.; Yang, Z.; Zheng, G., Reduced Mesoporous Co3o4nanowires as Efficient Water Oxidation Electrocatalysts and Supercapacitor Electrodes. *Adv. Energy Mater.* 2014, 4, 1400696.

150. Zhou, T.; Zheng, Y.; Gao, H.; Min, S.; Li, S.; Liu, H. K.; Guo, Z., Surface Engineering and Design Strategy for Surface-Amorphized Tio2@Graphene Hybrids for High Power Li-Ion Battery Electrodes. *Adv. Sci.* 2015, 2, 1500027.

151. Zhong, Y.; Yang, K. R.; Liu, W.; He, P.; Batista, V.; Wang, H., Mechanistic Insights into Surface Chemical Interactions between Lithium Polysulfides and Transition Metal Oxides. *J. Phys. Chem. C* 2017, 121, 14222-14227.

152. Hou, T. Z.; Xu, W. T.; Chen, X.; Peng, H. J.; Huang, J. Q.; Zhang, Q., Lithium Bond Chemistry in Lithium-Sulfur Batteries. *Angew. Chem. Int. Ed. Engl.* 2017, 56, 8178-8182.

153. Liu, Y.; Lin, D.; Yuen, P. Y.; Liu, K.; Xie, J.; Dauskardt, R. H.; Cui, Y., An Artificial Solid Electrolyte Interphase with High Li-Ion Conductivity, Mechanical Strength, and Flexibility for Stable Lithium Metal Anodes. *Adv. Mater.* 2017, 29.

154. Liu, X.; Huang, J. Q.; Zhang, Q.; Mai, L., Nanostructured Metal Oxides and Sulfides for Lithium-Sulfur Batteries. *Adv. Mater.* 2017, 29, 1601759.

155. Liang, Z.; Zheng, G. Y.; Li, W. Y.; Seh, Z. W.; Yao, H. B.; Yan, K.; Kong, D. S.; Cui, Y., Sulfur Cathodes with Hydrogen Reduced Titanium Dioxide Inverse Opal Structure. *ACS nano* 2014, 8, 5249-5256.

156. Pang, Q.; Liang, X.; Kwok, C. Y.; Nazar, L. F., Advances in Lithium–Sulfur Batteries Based on Multifunctional Cathodes and Electrolytes. *Nat. Energy* 2016, 1, 16132.

157. Mi, Y. Y.; Liu, W.; Li, X. L.; Zhuang, J. L.; Zhou, H. H.; Wang, H. L., High-Performance Li-S Battery Cathode with Catalyst-Like Carbon Nanotube-Mop Promoting Polysulfide Redox. *Nano Res.* 2017, 10, 3698-3705.

158. Yuan, Z.; Peng, H. J.; Hou, T. Z.; Huang, J. Q.; Chen, C. M.; Wang, D. W.; Cheng, X. B.; Wei, F.; Zhang, Q., Powering Lithium-Sulfur Battery Performance by Propelling Polysulfide Redox at Sulfiphilic Hosts. *Nano Lett.* 2016, 16, 519-527.

159. Yang, Z. Z.; Wang, H. Y.; Lu, L.; Wang, C.; Zhong, X. B.; Wang, J. G.; Jiang, Q. C., Hierarchical Tio2 Spheres as Highly Efficient Polysulfide Host for Lithium-Sulfur Batteries. *Sci. Rep.* 2016, 6, 22990.

160. Miao, L.; Wang, W.; Yuan, K.; Yang, Y.; Wang, A., A Lithium-Sulfur Cathode with High Sulfur Loading and High Capacity Per Area: A Binder-Free Carbon Fiber Cloth-Sulfur Material. *Chem. Commun. (Camb)* 2014, 50, 13231-4.

161. Peng, H.-J.; Huang, J.-Q.; Cheng, X.-B.; Zhang, Q., Review on High-Loading and High-Energy Lithium-Sulfur Batteries. *Adv. Energy Mater.* 2017, 7, 1700260.

162. Lu, F.; Zhou, M.; Li, W.; Weng, Q.; Li, C.; Xue, Y.; Jiang, X.; Zeng, X.; Bando, Y.; Golberg, D., Engineering Sulfur Vacancies and Impurities in Nico2s4 Nanostructures toward Optimal Supercapacitive Performance. *Nano Energy* 2016, 26, 313-323.

163. Lui, G.; Li, G.; Wang, X.; Jiang, G.; Lin, E.; Fowler, M.; Yu, A.; Chen, Z., Flexible, Three-Dimensional Ordered Macroporous Tio2 Electrode with Enhanced Electrode–Electrolyte Interaction in High-Power Li-Ion Batteries. *Nano Energy* 2016, 24, 72-77.

164. Luo, D.; Deng, Y. P.; Wang, X.; Li, G.; Wu, J.; Fu, J.; Lei, W.; Liang, R.; Liu, Y.; Ding, Y.; Yu, A.; Chen, Z., Tuning Shell Numbers of Transition Metal Oxide Hollow Microspheres toward Durable and Superior Lithium Storage. *ACS nano* 2017, 11, 11521-11530.

165. Zhang, Z.; Deng, Y. P.; Xing, Z.; Luo, D.; Sy, S.; Cano, Z. P.; Liu, G.; Jiang, Y.; Chen, Z., "Ship in a Bottle" Design of Highly Efficient Bifunctional Electrocatalysts for Long-Lasting Rechargeable Zn-Air Batteries. *ACS nano* 2019, 13, 7062-7072.

166. Feng, L.-L.; Fan, M.; Wu, Y.; Liu, Y.; Li, G.-D.; Chen, H.; Chen, W.; Wang, D.; Zou, X., Metallic Co9s8 Nanosheets Grown on Carbon Cloth as Efficient Binder-Free Electrocatalysts for the Hydrogen Evolution Reaction in Neutral Media. *J. Mater. Chem. A* 2016, 4, 6860-6867.

167. Li, B. Q.; Zhao, C. X.; Chen, S.; Liu, J. N.; Chen, X.; Song, L.; Zhang, Q., Framework-Porphyrin-Derived Single-Atom Bifunctional Oxygen Electrocatalysts and Their Applications in Zn-Air Batteries. *Adv. Mater.* 2019, 31, e1900592.

168. Kleibeuker, J. E.; Choi, E.-M.; Jones, E. D.; Yu, T.-M.; Sala, B.; MacLaren, B. A.; Kepaptsoglou, D.; Hernandez-Maldonado, D.; Ramasse, Q. M.; Jones, L.; Barthel, J.; MacLaren, I.; MacManus-Driscoll, J. L., Route to Achieving Perfect B-Site Ordering in Double Perovskite Thin Films. *NPG Asia Mater.* 2017, 9, e406-e406.

169. Cai, W.; Li, G.; Luo, D.; Xiao, G.; Zhu, S.; Zhao, Y.; Chen, Z.; Zhu, Y.; Qian, Y., The Dual-Play of 3d Conductive Scaffold Embedded with Co, N Codoped Hollow Polyhedra toward High-Performance Li-S Full Cell. *Adv. Energy Mater.* 2018, 8, 1802561.

170. Wu, J.; Ma, Q.; Lian, C.; Yuan, Y.; Long, D., Promoting Polythionate Intermediates Formation by Oxygen-Deficient Manganese Oxide Hollow Nanospheres for High Performance Lithium-Sulfur Batteries. *Chem. Eng. J.* 2019, 370, 556-564.

171. Cai, W.; Li, G.; Zhang, K.; Xiao, G.; Wang, C.; Ye, K.; Chen, Z.; Zhu, Y.; Qian, Y., Conductive Nanocrystalline Niobium Carbide as High-Efficiency Polysulfides Tamer for Lithium-Sulfur Batteries. *Adv. Funct. Mater.* 2017, 1704865.

172. Meng, J.; He, Q.; Xu, L.; Zhang, X.; Liu, F.; Wang, X.; Li, Q.; Xu, X.; Zhang, G.; Niu, C.; Xiao, Z.; Liu, Z.; Zhu, Z.; Zhao, Y.; Mai, L., Identification of Phase Control of Carbon‐Confined Nb2o5 Nanoparticles toward High‐Performance Lithium Storage. *Adv. Energy Mater.* 2019, 9, 1802695.

173. Li, X.; Gao, B.; Huang, X.; Guo, Z.; Li, Q.; Zhang, X.; Chu, P. K.; Huo, K., Conductive Mesoporous Niobium Nitride Microspheres/Nitrogen-Doped Graphene Hybrid with Efficient Polysulfide Anchoring and Catalytic Conversion for High-Performance Lithium-Sulfur Batteries. *ACS Appl. Mater. Interfaces* 2019, 11, 2961-2969.

174. Li, S.; Xu, Q.; Uchaker, E.; Cao, X.; Cao, G., Comparison of Amorphous, Pseudohexagonal and Orthorhombic Nb2o5 for High-Rate Lithium Ion Insertion. *CrystEngComm* 2016, 18, 2532-2540.

175. Greczynski, G.; Hultman, L., X-Ray Photoelectron Spectroscopy: Towards Reliable Binding Energy Referencing. *Progress in Materials Science* 2020, 107.

176. Ma, Z.; Li, S.; Wu, L.; Song, L.; Jiang, G.; Liang, Z.; Su, D.; Zhu, Y.; Adzic, R. R.; Wang, J. X.; Chen, Z., Nbox Nano-Nail with a Pt Head Embedded in Carbon as a Highly Active and Durable Oxygen Reduction Catalyst. *Nano Energy* 2020, 69.

177. Zhang, X.; Guo, J.; Guan, P.; Liu, C.; Huang, H.; Xue, F.; Dong, X.; Pennycook, S. J.; Chisholm, M. F., Catalytically Active Single-Atom Niobium in Graphitic Layers. *Nat. Commun.* 2013, 4, 1924.

178. Nowak, I.; Ziolek, M., Niobium Compounds: Preparation, Characterization, and Application in Heterogeneous Catalysis. *Chem. Rev.* 1999, 99, 3603-3624.

179. Hemmati, S.; Li, G.; Wang, X.; Ding, Y.; Pei, Y.; Yu, A.; Chen, Z., 3d N-Doped Hybrid Architectures Assembled from 0d T-Nb2o5 Embedded in Carbon Microtubes toward High-Rate Li-Ion Capacitors. *Nano Energy* 2019, 56, 118-126.

180. Wang, B.; Zhao, Y.; Banis, M. N.; Sun, Q.; Adair, K. R.; Li, R.; Sham, T. K.; Sun, X., Atomic Layer Deposition of Lithium Niobium Oxides as Potential Solid-State Electrolytes for Lithium-Ion Batteries. *ACS Appl. Mater. Interfaces* 2018, 10, 1654-1661.

181. Sugiura, C.; Kitamura, M.; Muramatsu, S., Niobium Liii and Lii X-Ray Absorption-Edge Spectra of Nb2o5 and Nh4nbf6. *J. Phys. Chem. Solids* 1988, 49, 1095-1099.

182. Cao, J.; Poumellec, B.; Mazerolles, L.; Brisset, F.; Helbert, A.-L.; Surble, S.; He, X.; Lancry, M.; Pinckney, L., Nanoscale Phase Separation in Lithium Niobium Silicate Glass by Femtosecond Laser Irradiation. *J. Am. Ceram. Soc.* 2017, 100, 115-124.

183. Kubouchi, Y.; Hayakawa, S.; Namatame, H.; Hirokawa, T., Direct Observation of Fractional Change of Niobium Ionic Species in a Solution by Means of X-Ray Absorption Fine Structure Spectroscopy. *X-Ray Spectrom.* 2012, 41, 259-263.

184. Luo, D.; Li, G.; Deng, Y.-P.; Zhang, Z.; Li, J.; Liang, R.; Li, M.; Jiang, Y.; Zhang, W.; Liu, Y.; Lei, W.; Yu, A.; Chen, Z., Synergistic Engineering of Defects and Architecture in Binary Metal Chalcogenide toward Fast and Reliable Lithium-Sulfur Batteries. *Adv. Energy Mater.* 2019, 1900228.

185. Nuraini, U.; Agustianawati, D.; Yahya, E.; Cahyono, Y.; Kidkhunthod, P.; Suasmoro, S., The Influence of Local Distortion on the Electrical Properties of the (1-X)(K 0.5 Na 0.5)Nbo 3 -X(Ba 0.8 C 0.2)Tio 3 System. *Ceram. Int.* 2017, 43, 3664-3669.

186. Zhang, J.; Li, G.; Zhang, Y.; Zhang, W.; Wang, X.; Zhao, Y.; Li, J.; Chen, Z., Vertically Rooting Multifunctional Tentacles on Carbon Scaffold as Efficient Polysulfide Barrier toward Superior Lithium-Sulfur Batteries. *Nano Energy* 2019, 64, 103905.

187. Lin, Z.; Nan, C.; Ye, Y.; Guo, J.; Zhu, J.; Cairns, E. J., High-Performance Lithium/Sulfur Cells with a Bi-Functionally Immobilized Sulfur Cathode. *Nano Energy* 2014, 9, 408-416.

188. Gorlin, Y.; Patel, M. U. M.; Freiberg, A.; He, Q.; Piana, M.; Tromp, M.; Gasteiger, H. A., Understanding the Charging Mechanism of Lithium-Sulfur Batteries Using Spatially Resolved Operando X-Ray Absorption Spectroscopy. *J. Electrochem. Soc.* 2016, 163, A930-A939.

189. Li, X.; Banis, M.; Lushington, A.; Yang, X.; Sun, Q.; Zhao, Y.; Liu, C.; Li, Q.; Wang, B.; Xiao, W.; Wang, C.; Li, M.; Liang, J.; Li, R.; Hu, Y.; Goncharova, L.; Zhang, H.; Sham, T. K.; Sun, X., A High-Energy Sulfur Cathode in Carbonate Electrolyte by Eliminating Polysulfides Via Solid-Phase Lithium-Sulfur Transformation. *Nat. Commun.* 2018, 9, 4509.